

# **A Multiscale Analysis on the Effect of Atomistic Processes on Mechanical Properties**

By Liam Morrissey (Thesis) submitted to the School of Graduate Studies in partial  
fulfillment of the requirement for the degree of

**PhD Mechanical Engineering/ Faculty of Engineering and Applied Science**

Memorial University of Newfoundland

**November 2020**

St. John's Newfoundland and Labrador

## Acknowledgements

Over the last 4 years of my PhD I have received significant support, both financially and personally from a number of invaluable sources. First, I would like to acknowledge Suncor Energy and the National Sciences and Engineering Research council for their significant financial support. Without these programs in place this research would not have been possible. Next, I would like to acknowledge Ahmed El-Ruby, Stephen Handrigan, Sabir Subedi, and Doug Pratt for their friendship and research assistance throughout my PhD. You have all made this experience an extremely positive one and helped keep research 'fun' even when faced with never-ending challenges. Personally, I also need to recognize my family (Alex States, Lynn Morrissey, Bill Morrissey, and Shaun Morrissey). Your unwavering support of my dreams and goals has been the foundation of my passion for research. Thanks for always listening to my research ramblings and cleaning up my notes throughout the house. Next, I would like to recognize Dr. Hawboldt, Dr. Shirokoff (committee members) and Dr. Morrill (master's supervisor) for their constant support in both my master's and PhD. Finally, I can only attempt to convey my gratitude to Dr. Nakhla. Your supervision and support was more than I could have ever expected. You have pushed me and challenged me to meet my potential all while being there every step of the way. You have encouraged creativity and passion all while constantly reminding us of the importance of friendship and family. Beyond this you have become like a part of my family and I look forward to many years of collaboration. Long live the team.

## Table of Contents

<b>Acknowledgements</b> .....	<b>2</b>
<b>List of Tables</b> .....	<b>7</b>
<b>List of Figures</b> .....	<b>9</b>
<b>List of Abbreviations</b> .....	<b>13</b>
<b>Abstract</b> .....	<b>14</b>
<b>Chapter 1: Literature Review</b> .....	<b>15</b>
<b>Introduction and Overview</b> .....	<b>15</b>
<b>Hydrogen Embrittlement in the Offshore Environment</b> .....	<b>17</b>
Hydrogen Embrittlement Models .....	17
The Effect of Hydrogen on Mechanical Properties .....	19
Molecular Dynamics Simulations: An alternative traditional testing .....	19
Previous Simulations on the Effect of Hydrogen .....	23
<b>Atomic Scale Collisions in Space</b> .....	<b>25</b>
The Low Earth Orbit and Deep Space .....	25
Molecular Dynamics Simulations: An Alternative to Testing in the Field .....	26
<b>Molecular Dynamics Fundamentals</b> .....	<b>28</b>
EAM/MEAM .....	29
Tersoff .....	31
ReaxFF .....	31
Importance of Potential .....	32
<b>Knowledge Gap</b> .....	<b>33</b>
MD simulations and Mechanical Properties .....	33
Effect of Hydrogen on Microstructure.....	33
Effect of Atomic Oxygen on Microstructure .....	34
<b>References</b> .....	<b>35</b>
<b>Co-authorship Statement</b> .....	<b>40</b>
<b>Chapter 2: Quantifying Void Formation and Changes to Microstructure during Hydrogen Charging: A precursor to Embrittlement and Blistering</b> .....	<b>41</b>
<b>Abstract:</b> .....	<b>42</b>
<b>Introduction</b> .....	<b>43</b>
Hydrogen Damage .....	43
Effect of Hydrogen in Producing Vacancies .....	44
<b>Purpose of Study</b> .....	<b>45</b>
<b>Materials and Methods</b> .....	<b>45</b>
Sample Microstructure .....	45
CT Imaging .....	46
Thresholding .....	47
Noise Reduction .....	48
Hydrogen Charging .....	49

Limitations .....	50
<b>Results and Discussion .....</b>	<b>51</b>
Initial Void Volume Fraction .....	51
Post-Charging Void Volume Fraction .....	53
Effect of Hydrogen on Void Distribution.....	55
SEM Analysis .....	58
Effect on Mechanical Behavior .....	60
<b>Conclusion .....</b>	<b>61</b>
<b>References .....</b>	<b>62</b>
<b>Chapter 3: A Finite Element Model to Predict the Effect of Porosity on Elastic Modulus in Low Porosity Materials .....</b>	<b>63</b>
<b>Abstract: .....</b>	<b>64</b>
<b>Introduction .....</b>	<b>65</b>
Background .....	65
Porosity and its Effect on Modulus .....	66
Low Porosity Materials .....	67
Intermediate Porosity .....	68
Finite Element Models .....	70
<b>Purpose of Study .....</b>	<b>71</b>
<b>Procedures .....</b>	<b>72</b>
Evaluation of Existing Models .....	72
Finite Element Model Study.....	72
<b>Results and Discussion .....</b>	<b>76</b>
Effect of Porosity on Elastic Modulus .....	76
Evaluation of Existing Models .....	78
<b>Finite Element Model .....</b>	<b>84</b>
Effect of Pore Orientation on Elastic Modulus Comparison of Finite Element Model with Analytical Models and Experimental Values .....	84
Comparison of Finite Element Model with Analytical Models and Experimental Values .....	86
<b>Conclusions .....</b>	<b>89</b>
<b>References .....</b>	<b>90</b>
<b>Chapter 4: Atomistic Uniaxial Tension Tests: Investigating various many-body potentials for their ability to produce accurate stress strain curves using molecular dynamics simulations</b>	<b>92</b>
<b>Abstract .....</b>	<b>93</b>
<b>Introduction .....</b>	<b>94</b>
<b>Molecular Dynamics.....</b>	<b>96</b>
Many-body Potentials.....	96
EAM/MEAM .....	97
Tersoff.....	98
ReaxFF.....	98
<b>Materials and Methods .....</b>	<b>99</b>
<b>Results .....</b>	<b>102</b>
EAM Potential .....	103

MEAM Potential.....	105
Tersoff Potential .....	106
ReaxFF Potential .....	107
Importance of Investigating Parameterization Testing Procedure .....	108
<b>Conclusion .....</b>	<b>109</b>
<b>References .....</b>	<b>110</b>
<b>Chapter 5: Considerations when assessing the applicability of interatomic force fields for predicting mechanical properties of single crystals and bulk polycrystals .....</b>	<b>112</b>
<b>Abstract .....</b>	<b>113</b>
<b>Introduction .....</b>	<b>114</b>
Obtaining Mechanical Properties in MD Simulations .....	114
The Importance of Potential Type .....	116
Single Crystals and Polycrystals .....	118
Purpose .....	121
<b>Methodology .....</b>	<b>122</b>
Atomistic Uniaxial Tension Test .....	123
Polycrystalline Elastic Modulus.....	124
Fixed Lateral Axis Tension Test .....	126
<b>Results .....</b>	<b>127</b>
Effect of Crystal Orientation .....	127
Importance of Potential Parameterization .....	131
Effect of Ensemble during Straining: fixed volume <i>NVT</i> and uniaxial <i>NPT</i> .....	132
Estimating Polycrystalline Mechanical Properties: The VRH Method.....	134
<b>Conclusion .....</b>	<b>136</b>
<b>References .....</b>	<b>138</b>
<b>Case Study 1: Hydrogen Embrittlement of Metals.....</b>	<b>140</b>
<b>Chapter 6: Hydrogen Embrittlement of Iron: A Molecular Dynamics simulation study on the effect of hydrogen on mechanical properties.....</b>	<b>140</b>
<b>Abstract .....</b>	<b>141</b>
<b>Introduction .....</b>	<b>142</b>
Importance of Interatomic Potential .....	144
Purpose .....	145
<b>Methodology .....</b>	<b>146</b>
Simulation Set-up.....	146
Atomistic Tension Test.....	148
<b>Results .....</b>	<b>149</b>
Effect of Hydrogen on Elastic Modulus.....	149
Comparison with Experimental data and Assessment of Potential .....	151
Effect of Hydrogen on Dislocation Formation.....	154
Effect of Hydrogen on Lattice and Deformation Mechanism .....	159
<b>Conclusions .....</b>	<b>161</b>
<b>References .....</b>	<b>162</b>

<b>Case Study 2: Atomic Impacts in Space .....</b>	<b>164</b>
<b>Chapter 7: Erosion of Spacecraft Metals due to Atomic Oxygen: A Molecular Dynamics Simulation .....</b>	<b>164</b>
<b>Abstract .....</b>	<b>165</b>
<b>Introduction .....</b>	<b>166</b>
<b>Purpose of Study: MD Simulations of Metals.....</b>	<b>168</b>
<b>Methodology .....</b>	<b>169</b>
ReaxFF reactive molecular simulation force field .....	169
Simulation Model for Atomic Oxygen Impact.....	170
<b>Results and Discussion .....</b>	<b>173</b>
Erosion Yields.....	173
Temperature and Heat Transfer Effects during Impact .....	178
<b>Conclusion .....</b>	<b>181</b>
<b>References .....</b>	<b>182</b>
<b>Chapter 8: The Effect of Atomic Oxygen Flux and Impact Energy on the Damage of Spacecraft Metals .....</b>	<b>184</b>
<b>Abstract .....</b>	<b>185</b>
<b>Introduction .....</b>	<b>186</b>
<b>Purpose.....</b>	<b>188</b>
<b>Methodology .....</b>	<b>188</b>
Molecular Dynamics and Force Field Selection .....	188
Atomic Oxygen Simulation Model .....	190
Damage Tracking .....	193
<b>Results .....</b>	<b>194</b>
Verification of Forcefields .....	194
Effect of Impact Energy.....	195
Effect of Thermostat and Importance of Temperature .....	197
Comparison of Substrates: Damage and Erosion.....	202
Depth of Damage .....	205
Evolution of Defects after Impact .....	206
<b>Conclusions .....</b>	<b>208</b>
<b>References .....</b>	<b>209</b>
<b>Summary .....</b>	<b>211</b>

## List of Tables

Table 2.1- Void volume fractions before and after hydrogen charging based on CT imaging of 6 samples.

Table 2.2 - Summary of Initial void volume ratios reported in literature

Table 2.3 - Axial void volume fraction distribution of samples before and after hydrogen charging

Table 2.4 - Weight percentage of an uncharged and charged surface using a thermo electron dispersive spectrometer

Table 3.1 - Finite Element Plate Specifications

Table 3.2 - Predicted Reduction in Modulus for the Finite Element Model, Various Common Relationships for Porosity, and a line of best fit for experimental values between 1-10%

Table 4.1 - Input parameters for *LAMMPS* simulations

Table 4.2 - Predicted elastic modulus for various potentials from atomistic uniaxial tension test

Table 4.3 - Predicted Poisson's ratio for various potentials from atomistic uniaxial tension test

Table 5.1 - Summary of potentials tested for BCC Iron and FCC Aluminum

Table 5.2 - Experimental elastic moduli for single crystal BCC iron and FCC aluminum as a function of temperature and crystal orientation

Table 5.3- Predicted elastic modulus for single crystal BCC iron (A) and FCC aluminum (B) from a uniaxial tension test with an *NPT* ensemble. Error is calculated relative to single crystal experimental values.

Table 5.4 - Predicted elastic modulus for single crystal BCC iron (A) and FCC aluminum (B) from a uniaxial tension test with an *NVT* ensemble. Error is calculated relative to single crystal experimental values

Table 5.5 - Predicted polycrystalline elastic modulus and shear modulus for BCC iron (A) and FCC aluminum (B) from a uniaxial tension test with an *NPT* ensemble using the VRH method. Error is calculated relative to bulk polycrystalline experimental values.

Table 6.1 - Summary of previous studies on hydrogen embrittlement simulations with relevant concentration

Table 6.2 - Average percent reduction in elastic modulus for various concentrations and temperatures using EAM and ReaxFF potentials

Table 6.3 - Predicted diffusion coefficients and associated error as compared to experimental values

Table 6.4 - Percent reduction in stress at dislocation initiation for various concentrations and temperatures using EAM potential

Table 6.5: Bond Distance changes between BCC atoms with and without interstitial hydrogen

Table 7.1 - Input parameters for molecular dynamics models.

Table 8.1 - Atomic oxygen impact energies and corresponding impact speeds tested

Table 8.2 - Predicted and experimental vacancy formation for silver and aluminum [18]

Table 8.3 - Number of eroded aluminum and silver atoms at various times as a function of impact energy using a thin bath layer

Table 8.4 - Number of defects per atom after impact and annealing for aluminum and silver after annealing for various impact energies using a thin bath layer

## List of Figures

Figure 2.1 – SEM image of initial microstructure of sample at x2000 (A) and x4000 (B) magnifications

Figure 2.2 - Dimensions of stainless steel samples for charging

Figure 2.3 - Schematic of Hydrogen Charging Procedure

Figure 2.4 - Void volume fraction before and after hydrogen charging

Figure 2.5 - 3D models of stainless steel samples pre and post charging for samples 1 and 6. Voids are shown as a color in the grey bulk material.

Figure 2.6 - Layout of slices used to determine void distribution axially

Figure 2.7 - Axial distributions of void volume fractions for 6 samples before (blue bars) and after (red bars) charging

Figure 2.8 - SEM image uncharged (A) and charged (B) sample at x23000 magnification

Figure 3.1 - Stress/Strain Plot for Finite Element model of steel plate with zero porosity.

Figure 3.2 - An example of the 6 different pore orientations (shown at 6% total porosity) tested in the Finite Element model. 1 center pore (A), 2 horizontal pores (B), 2 vertical pores (C), 5 horizontal pores (D), 5 unbalanced pores (E), 5 extreme unbalanced pores (F)

Figure 3.3 - A compilation of experimental data for the percent reduction in elastic for various materials with porosity between 1-10% (Alumina 1, Alumina 2, thermoset polyester resin, HfO<sub>2</sub>, sintered Iron, MgAl<sub>2</sub>O<sub>4</sub>)

Figure 3.4 - Predicted reduction in elastic modulus for various analytical models compared with experimental data for materials with porosity between 0-2% (A) and 2-10% (B)

Figure 3.5 - Effect of pore orientation on reduction of elastic modulus for low porosity materials. Note: There was no test for 5 pores spread along the vertical axis due to the required pore radii at 8 and 10% porosity.

Figure 3.6 - The predicted reduction in elastic modulus for porosities between 0-10% for the proposed Finite Element model as compared to analytical models.

Figure 3.7 - Predicted reduction in modulus for finite element model compared with experimental data for materials with porosity between 1-10% (Alumina 1, Alumina 2, thermoset polyester resin, HfO<sub>2</sub>, sintered Iron, MgAl<sub>2</sub>O<sub>4</sub>)

Figure 4.1 - Typical tensile test specimen with gage section (A) that then forms the iron simulation cell for molecular dynamics (B)

Figure 4.2 - Stress strain curves for EAM potentials

Figure 4.3 - Stress strain curves for MEAM potentials

Figure 4.4 - Stress strain curves for Tersoff potential

Figure 4.5 - Stress strain curves for ReaxFF potentials

Figure 5.1 - Initial structure of BCC iron (A) and FCC aluminum (B) prior to straining\*.

Figure 5.2 - Polycrystalline elastic modulus from using the VRH method as a function of temperature for iron and aluminum using various interatomic potentials

Figure 6.1 - Iron cube before (A) and after (B) addition of atomic hydrogen. Blue atoms are iron and red atoms are atomic hydrogen

Figure 6.2 - Reduction in elastic modulus as a function of hydrogen concentration for EAM (A) and ReaxFF (B) potentials

Figure 6.3 - MSD vs time for EAM (A) and ReaxFF (B) potentials used to calculate diffusion coefficient

Figure 6.4 - Microstructure of iron cube with 0.5% hydrogen at various strains with corresponding stresses. In figure A all atoms are in BCC structure (blue) and no dislocations have formed (hydrogen atoms filtered out). In figures B and C dislocations are nucleating or have formed as shown in the green and red atoms (other atoms are filtered out to show dislocations).

Figure 6.5 - Microstructure of iron cube with 5% hydrogen at various strains with corresponding stresses. In Figure A all atoms are in BCC structure (blue) and no dislocations have formed (hydrogen atoms filtered out). In Figures B and C dislocations are nucleating or have formed as shown in the green and red atoms (other atoms are filtered out to show dislocations).

Figure 6.6: BCC Iron lattice arrangement with and without hydrogen in the tetrahedral interstitial site

Figure 6.7: Stress strain curves for iron slab at 300K with various hydrogen concentrations in the lattice

Figure 6.8:  $a/2 \langle 111 \rangle$  Dislocations in iron sample after reaching peak stress for case of 0.5% hydrogen (A) and 5% hydrogen (B)

Figure 7.1 - Initial silver substrate set up in well prior to atomic oxygen impact

Figure 7.2 - Side view of silver lattice before impact (A), after 50 impacts (B) and after 100 oxygen impacts (C) where grey spheres are silver and red are oxygen. Eroded atoms have been removed.

Figure 7.3 - Number of atoms eroded from surface as a function of atomic oxygen impact for Silver and Gold

Figure 7.4 - Side view of gold lattice before impact (A), after 50 impacts (B) and after 100 oxygen impacts (C) where gold spheres are gold and red are oxygen. Eroded atoms have been removed.

Figure 7.5 - Substrate temperature for gold and silver as a function of atomic oxygen impacts

Figure 7.6 - Combined plot of number of eroded silver atoms and substrate temperature as a function of atomic oxygen impacts.

Figure 8.1 - Initial substrates of FCC silver (A) and FCC aluminum (B) in simulation box prior to impact

Figure 8.2 - Number of defects per atom in silver (A) and aluminum (B) as a function of time for various impact energies with a thin bath layer

Figure 8.3 - Relationship between the number of defects per atom and impact energy for both silver and aluminum

Figure 8.4 - Number of defects per atom for silver (A) and aluminum (B) as a function of time for various impact energies with no bath layer

Figure 8.5 - Number of defects per atom in silver as a function of time for various impact energies (A-D)

Figure 8.6 - Number of defects per atom in aluminum as a function of time for various impact energies (A-D)

Figure 8.7 - Temperature profiles for aluminum and silver with (A,B) and without (C,D) a bath layer

Figure 8.8 - Silver (A, B) and aluminum (C, D) substrates after 100 impacts at 4.5 eV and 30 eV, respectively. Red atoms are oxygen, grey are silver, and blue are aluminum

Figure 8.9 - Depth of defects in substrate for silver (A) and aluminum (B) as a function of impact energy using a thin bath layer

Figure 8.10 - Number of defects per atom after impact and annealing for silver and aluminum as a function of impact energy using a thin bath layer

## List of Abbreviations

HE: Hydrogen Embrittlement

MD: Molecular Dynamics

EAM: Embedded Atom Method

MEAM: Modified Embedded Atom Method

AO: Atomic Oxygen

LEO: Low Earth Orbit

HEDE: Hydrogen Induced Decohesion

HELP: Hydrogen Enhanced Localized Plasticity

FEA: Finite Element Analysis

FEM: Finite Element Model

*LAMMPS*: Large-scale Atomic/Molecular Massively Parallel Simulator

VRH: Voigt-Reuss-Hill

## Abstract

The purpose of this thesis was to use multiscale testing and simulation methods to better understand the role various atomistic processes play in the degradation of mechanical properties in harsh environments. Specifically, two environments were considered: the effect of atomic hydrogen in harsh offshore oil and gas environments and the effect of atomic oxygen impacts in space. This thesis is written in a manuscript format with 8 unique chapters all falling under the umbrella of atomistic processes and macroscale properties. The thesis begins with a detailed literature review of all necessary background research including a summary of molecular dynamics and a detailed explanation of the current gaps in knowledge. This is followed by 4 chapters that test various method and multiscale simulation tools. Finally, findings from these chapters are applied to two specific environments where multiscale challenges exist: hydrogen in offshore oil and gas, and atomic impacts in space. Each chapter is written as a standalone paper including separate cover pages, literature reviews and conclusions. The findings from these case studies are then summarized in a conclusion.

# Chapter 1: Literature Review

## Introduction and Overview

As engineering projects continue to push the boundaries of that was once thought impossible, materials are now being subjected to harsher more extreme environments. Materials in these new environments require extremely accurate remaining life predictions that cannot be achieved by simply applying industry standard safety factors. For example, as the more readily harvestable oil becomes depleted offshore, operations must move to harsher remote offshore environments containing higher contaminant petroleum. The  $H_2S$  typically found in this petroleum is aggressively corrosive and can poison the hydrogen recombination reaction, allowing atomic hydrogen to diffuse into the microstructure. This hydrogen can then form microcracks in the material, causing a degradation of performance and premature failure in a process known as hydrogen embrittlement (HE) [1]. While the exact mechanisms of HE continue to evade researchers, its detrimental effect on mechanical properties is unquestioned. Therefore, safe performance in these environments requires a better understanding of the embrittlement processes at hand. As another example, the Canadian Space Agency and NASA have mandated that missions into deep space are a top priority in the coming years. However, travel in these extreme environments provides unique challenges such as atomic impacts, extreme temperature fluctuations, long service times, and payload restrictions. Harsh long-term exposure combined with significant payload restrictions does not allow for simple over engineering or safety factors. Instead, a better understanding of the environment and how exactly it interacts with and degrades the material is imperative.

While failure is typically considered to be a catastrophic macroscale event, its occurrence can be foreshadowed on the atomistic and microscale long before any obvious signs have developed. For example, microscale defects such as impurities, voids, dislocations, and cracks are all critical to the onset

of yielding and degradation of mechanical properties. Therefore, any accurate understanding of these processes requires a method to identify and account for the initiation, interaction and growth of microscale defects. However, common macroscale testing and simulation methods are unable to capture the detail needed to observe and quantify the effect of these defects on mechanical properties. Moreover, linking micro and atomistic scale simulations to macroscale mechanical properties is still a developing field with significant uncertainty. As a result, the purpose of the project was to use multiscale testing and simulation methods to better understand the role various atomistic processes play in the degradation of mechanical properties in harsh environments. Specifically, two environments were considered: the effect of atomic hydrogen in harsh offshore oil and gas environments and the effect of atomic oxygen impacts in space.

Overall two major environments were considered: offshore HE environments and space. While both these environments may at first appear to have little in common they both feature atomistic processes that can rapidly degrade material performance. In harsh offshore environments the  $H_2S$  can poison the hydrogen recombination reaction, increasing the prevalence of atomic hydrogen and hydrogen embrittlement (HE). Similarly, the radiation in space separates the  $O_2$  molecule resulting in high energy atomic oxygen in the low earth orbit (LEO). This atomic oxygen can collide with materials and lead to sputtering, erosion, and damage. However what makes both of these environments unique is that while macroscale effects are obvious, the processes behind them occur on the micro or atomistic scales. Therefore they represent a significant multiscale challenge. The subsequent sections will delve into the literature behind both environments, their effects on materials, and the current state of knowledge.

## Hydrogen Embrittlement in the Offshore Environment

### Hydrogen Embrittlement Models

The introduction of diffuse hydrogen into a metal can result in HE or, in the extreme case, hydrogen induced blistering; which can lead to drastic changes in mechanical behavior [1]. Hydrogen blistering is generally understood to be a product of diffuse hydrogen accumulating and recombining at pre-existing voids. As the hydrogen recombines it increases pressure within the lattice, resulting in plastic deformation of the microstructure and migration of the metal matrix to the surface, forming a 'blister' [1], [2]. However, while it is accepted that void growth due to hydrogen accumulation at voids is required for blistering, a quantitative study on this void growth has never been completed.

In contrast, the actual processes behind the 'embrittlement' are much more complicated and have been the subject to extensive research forming many different theories [3]. Similar to blistering, HE first involves the diffusion of hydrogen into the microstructure of the metal. While concentrations are not high enough to cause blisters or fractures, upon loading there is a degradation of mechanical properties. Several models to explain this decreased strength have been postulated. Of these models, both hydrogen induced decohesion (HEDE) [4] and hydrogen enhanced localized plasticity (HELP) [5] have emerged as the most referenced.

First, the HEDE mechanism postulates that the accumulation of hydrogen in lattice sites weakens bond strength, which in turn leads to a reduction in the stress at rupture. Second, the HELP mechanism posits that hydrogen reduces the interaction energy between the dislocation-hydrogen pair, leading to increased mobility of dislocations and shear localization. However, while the ability for hydrogen to increase dislocation motion has been demonstrated, the resulting effect on failure still produces debate.

In addition to these models, a third, more recently developed model focuses less on the role of hydrogen in promoting failure and more on the role of hydrogen in producing and sustaining vacancies in the material; which may then ultimately lead to failure. In a series of experiments on charged and uncharged samples, Nagumo et al. [6] first demonstrated the role of hydrogen in promoting the growth of defects and vacancies during straining. First, samples were charged and strained to create resistance curves (R-curves) that showed the J-integral versus advanced crack length. In a comparison of curves with and without charging, charged samples showed a decrease in ductile crack growth resistance. Moreover, when attempting to match these values for calculations, increasing initial void volume fraction from 2 to 3.5% accurately reproduced the hydrogen charged sample's R-curve. Therefore, this suggests that hydrogen may be increasing the initial void fraction pre-loading. Because ductile crack growth resistance is controlled by defect formation, these studies proposed a mechanism of hydrogen related failure in which the role of hydrogen may be to enhance void formation and thus produce lower energy paths for crack propagation [6].

Related to these findings, Gao et al. [7] used finite element models to study the effect of initial void fraction on fracture toughness. This study tested various initial void fractions and demonstrated that a higher void volume fraction pre loading leads to more void interaction and a significantly higher crack growth rate. When combining the findings of Nagumo et al. and Gao et al., the need for further research becomes clear. Gao et al. has shown that increased voids pre loading can lead to faster crack growth. Moreover, Nagumo et al. has suggested, through best fitting, that hydrogen alone may be increasing initial void fractions pre loading. However, Nagumo et al. focused only on the role of hydrogen during loading and did not first quantify the role hydrogen charging (without strain) plays on the initial void fractions.

## The Effect of Hydrogen on Mechanical Properties

While particular attention has been paid to simulating the embrittlement mechanisms, there is considerably less research on the effect of hydrogen on mechanical properties. Previous experimental work has suggested that hydrogen will decrease both the elastic modulus and yield strength [8]-[10]. For example, Ortiz et al. [8] tested the effect of hydrogen on the modulus of various steels. Specimens were charged over 24 hours using a cathodic method that was chosen to avoid the formation of internal cracks and blisters. Samples were then coated to prevent hydrogen loss and modulus was calculated using a resonance frequency method. All samples showed a reduction in modulus after charging, and reduction in modulus was linearly correlated to the hardness of the sample. Similarly, Zhang et al. [10] also observed a reduction in modulus after charging. This study concluded that the hydrogen causes a partial stress relaxation but that below 10 wppm hydrogen did not change the interatomic cohesive force of iron. However, due to the difficulty in measuring the exact concentration of hydrogen in the microstructure these experiments are often unable to correlate the reduction in modulus to a concentration of hydrogen. Moreover, it can be challenging to delineate whether changes in modulus are due to hydrogen or other mechanisms such as pre-existing voids, grain boundaries, impurities etc.

### Molecular Dynamics Simulations: An alternative traditional testing

To determine the effect of this diffuse hydrogen on mechanical properties macroscale laboratory tests such as tension tests and resonance frequency tests are typically used. However, because these tests occur on the macroscale they often only able to determine associated macroscale properties. In other words, while they may be able determine the effect on elastic modulus, they cannot shed light on the mechanisms in which hydrogen is affecting the microstructure. Moreover, due to atomistic scale of HE it is important to consider the role various structural defects have on the both the diffuse hydrogen and on the subsequent mechanical properties. For example, defects such as vacancies,

pre-existing dislocations, and impurities can all affect resulting mechanical properties. Byggmatar et al. [11] studied the effect of Cr impurities in Fe-Cr nanowires and demonstrated a reduction in ultimate and yield strength with increasing Cr concentration. As discussed above, Gao et al. [7] compared stress strain curves for materials with various initial void fractions. Findings indicated that a higher initial void fraction lead to more void coalescence and a higher crack growth rate. Therefore, accounting for microscale defects is critical to an accurate prediction of macroscale mechanical behaviour. One potentially promising alternative is using molecular dynamics (MD) to conduct atomistic tension tests. MD simulations consider the system on an atomic scale and can model the interactions between atoms during loading. Therefore, these simulations allow for both the actual modelling of atomistic processes and the prediction of the resulting mechanical properties.

Atomistic scale uniaxial tension simulations, originally proposed by Brown and Clarke [12] can be used to deform a small slab of the material and produce a stress strain curve. A slab is first prepared with periodic boundary conditions in all directions. Periodic boundary conditions create a small representative unit cell that is surrounded by image cells. Particles in the unit cell behave as being connected to one's image cells, allowing for simulation of an essentially infinite bulk. The bulk is then equilibrated to the prescribed temperature using either a thermostat or barostat. Once equilibrated the slab is then deformed in a specific direction with a specified strain rate to a final deformation. During straining the stresses are calculated at each step using the virial atomic stress tensor, which has been shown to be equivalent to the continuum Cauchy stress [13] as per equation 1:

$$S_{ab} = -\sum_i m_i v_i^a v_i^b + \frac{1}{2} \sum_i \sum_{j \neq i} F_{ij}^a r_{ij}^b \quad (1)$$

Where  $m_i$  and  $v_i$  are the mass and velocity of the atom  $i$ ,  $F_{ij}$  is the force between atoms  $i$  and  $j$ ,  $r_{ij}$  is the distance between atoms  $i$  and  $j$ , and the indices  $a$  and  $b$  denote the Cartesian components.

As with the macroscale tension test, the slope in the linear region of this curve is then used to obtain an elastic modulus. This method has been used by several previous studies to predict the elastic modulus of both metals [11], [14], [15] and polymers [12]. One particular advantage of these tests is that they can also control the presence of defects in the sample. For example, macroscale tests on hydrogen charged samples will inevitably contain various defects. Therefore these studies cannot determine the effect hydrogen alone has on mechanical properties. In contrast, MD simulations can be used to add hydrogen to the perfect, 'defect-free', specimens prior to loading.

Given the atomistic scale at which straining is taking place, it is important to also consider the single crystal nature of these tension tests. On the macroscale metals are polycrystalline with several single crystals oriented in various random directions to form a polycrystal. As a result, the elastic modulus of these polycrystalline metals is essentially isotropic and therefore independent of direction or orientation [16]. Therefore, the modulus obtained from a macroscale tension test is actually the polycrystalline elastic modulus. This becomes an important distinction when moving the discussion to atomistic scale tension tests. Due to size limitations, atomistic scale tension tests are typically conducted on single crystals with prescribed orientations and strain directions. As opposed to their polycrystalline counterparts, individual crystals for most metals are no longer isotropic and their elastic modulus therefore depends on the orientation of the crystal prior to straining. When comparing the results of atomistic tension tests to experimental results it is critical to obtain data for macroscale single crystals with the proper orientation and not the polycrystalline bulk isotropic crystals that are typically reported.

As an alternative, the Voigt-Reuss-Hill (VRH) approximation can be used to determine the elastic modulus of a polycrystalline sample using elasticity concepts [16], [17]. In this method, two critical

assumptions are made. First, the local strain is assumed to be equivalent to the mean strain, thus all grains undergo the same strain. This assumption, known as the Voigt average, calculates the Young's modulus via equation 2 using the elastic stiffness constants  $c_{ij}$ :

(2)

$$E_v = \frac{(A - B + 3C)(A + 2B)}{(2A + 3B + C)}$$

where:

$$A = \frac{c_{11} + c_{22} + c_{33}}{3}$$

$$B = \frac{c_{23} + c_{13} + c_{12}}{3}$$

$$C = \frac{c_{44} + c_{55} + c_{66}}{3}$$

Second, the local stress is assumed to be equivalent to the mean stress, thus all grains undergo the same stress. This assumption, known as the Reuss average, calculates a lower bound of the Young's modulus via equation 3 using the elastic compliance constants  $s_{ij}$ :

(3)

$$E_r = \frac{5}{(3A' + 2B' + C')}$$

where:

$$A = \frac{s_{11} + s_{22} + s_{33}}{3}$$

$$B = \frac{s_{23} + s_{13} + s_{12}}{3}$$

$$C = \frac{s_{44} + s_{55} + s_{66}}{3}$$

Finally, an estimated polycrystalline elastic modulus can then be determined by taking an average of the Voigt and Reuss moduli. However, no study has tested the accuracy of using multiple atomistic single crystal simulations combined with the VRH theory to predict the elastic modulus of a mesoscale polycrystal.

### Previous Simulations on the Effect of Hydrogen

Recently, several MD simulations are beginning to shed light on the mechanisms in which hydrogen is affecting the microstructure of metals. For example, Song and Curtin [18] considered the mechanism of embrittlement in iron using MD. Samples with embedded cracks were simulated with various concentrations of atomic hydrogen and then placed in a type I loading condition. Hydrogen was shown to accumulate near the crack tip and, depending on the concentration, block the emission of dislocations. The formation and motion of dislocation corresponds to the yield point and beginning of plasticity. Therefore, the interaction of hydrogen with dislocations is a key area of focus to explain the resulting affect on mechanical properties. As a result of the blocked dislocation motion the crack tip was unable to blunt and propagated with cleavage like failure. Moreover, the mechanism was shown to be dependent on both the grain orientation and concentration of hydrogen. Similar to this work, Xie et al. [19] considered the effect of hydrogen on dislocation motion. This study modeled periodic slabs of iron that were deformed plastically prior to being concentrated with hydrogen. After hydrogen was added the sample was relaxed to the prescribed temperature and then further deformed. Results indicated that hydrogen was trapped at the dislocations and impeded their subsequent motion during deformation. In addition, the study demonstrated that yield stress was directly proportional to the concentration of hydrogen in the lattice. However, only one crystal orientation was considered and the authors commented on the importance of considered other orientations where the often-observed

[111] dislocation type could be present. Moreover, the study did not consider samples that were not deformed prior to hydrogen addition or the effect of hydrogen on elastic modulus.

In addition to considering the effect of hydrogen on dislocations, the interaction of hydrogen with vacancies and voids is another commonly discussed model of embrittlement. For example, Lee and Bernstein [20] used testing to demonstrate that hydrogen enhanced the nucleation of voids along characteristic slip bands. Similarly, in-situ measurements using x ray diffraction has shown that hydrogen reduced the vacancy formation energy, increasing the presence of vacancies; an important prerequisite for the formation of voids [21]. As opposed to traditional testing, Lv et al. [22] used MD to model the interaction of hydrogen with vacancies. Results demonstrated that hydrogen vacancy bonding was energetically preferred to hydrogen-hydrogen or vacancy-vacancy bonding at 1 nearest neighbor distance. As the percentage of vacancies increased the diffusion rate of hydrogen decreased, indicating a trapping of hydrogen with vacancies. However, this study did not consider the effect of hydrogen concentration or the effect the diffuse hydrogen and vacancies had on other mechanical properties. For example, while it is known that voids can decrease mechanical properties, the effect of hydrogen on this degradation is much less studied. Moreover, simulations are often limited to one crystal orientation or hydrogen concentration and are therefore applicable only to the specific case considered.

As with macroscale testing, there is significantly less research that uses MD to study the effect of hydrogen on mechanical properties. Yu et al. [23] used MD to simulate the effect of hydrogen on the mechanical properties of tungsten. Atomic hydrogen at various concentrations was added to a perfect lattice at room temperature. The periodic tungsten sample was then strained into the plastic region and the corresponding modulus and peak stress were studied. Results demonstrated that hydrogen lead to a

reduction in both modulus and yield strength with increasing lattice concentration. However, there is a lack of research on the effect diffuse atomic hydrogen alone has the mechanical properties of iron at various temperatures.

## Atomic Scale Collisions in Space

### The Low Earth Orbit and Deep Space

As missions continue to move to deeper space there is a pressing need to better understand the performance of the materials that will take us there. One of the biggest threats to these spacecraft materials is high energy atomic impacts. For example, in the low Earth orbit (LEO) atomic oxygen (AO) impacts represent a significant source of erosion and performance degradation [24]. These impacts can reach energies of 4.5 eV and, depending on the material, can lead to material loss and reduced performance [25]. Significant in-situ testing and simulations have been performed to better understand the effect of AO oxygen collisions in the LEO [24]. The results of these studies have allowed scientists to better understand how a material performs and which materials are most suitable for LEO exposure. Results show that while AO is highly reactive with many polymers, its effect on metals varies significantly. Two of the most common metals found on spacecrafts are gold and silver. Silver is a critical component for electrical applications while gold is commonly used as a coating its low erosion rates and ability to absorb visible light [24]. Moreover, while gold shows very little erosion due to AO, silver is highly reactive with significant material degradation over prolonged exposure [24]. Due to the large differences in performance that can exist amongst various materials they must each be tested in LEO for their performance prior to application. However, these tests are not always feasible due to the high cost of space launches and constant uncertainty in budgets. A way to accurately model the effect of atomic oxygen on surfaces could both enhance the accuracy of remaining life predictions and eliminate the

need to test new materials in LEO. While AO testing facilities certainly offer a viable option, they too are costly, require advanced equipment, and cannot always replicate the harsh space environment.

While the LEO has received fairly exhaustive research, as these materials move even deeper into space they can be subjected to significantly higher energy collisions with both cosmic dust and the interstellar medium. For example, the Cassini-Huygens Cosmic Dust Analyzer has detected nanoscale dust particles at speeds higher than 200 km/s [26]. While impacts with these dust particles would likely be catastrophic, in addition to nanoscale dust, impacts with high speed interplanetary/interstellar atomic gases may also hinder performance [27]. For example, Hoang et al. [28] considered the interaction of relativistic spacecrafts with the interstellar medium. The study attempted to quantify the potential effects of collisions with both interstellar gas and dust using theoretical predictions. Findings indicated that atomistic gas bombardment could result in macroscale surface damages for a quartz material traversing a gas column at 0.2 the speed of light. As a result, while many spacecraft materials may be assumed to be non reactive with AO and thus suitable for the LEO, there may exist an energy barrier that could be overcome with a harsh enough environment. In other words, suitability in the LEO does not guarantee performance with higher energy collisions. However, unlike the LEO environment, materials cannot be easily tested in-situ and simulating the conditions in a laboratory environment is both costly and extremely complex. As such, there is a need for more feasible methods of simulating and comparing the performance of materials in these extremely harsh environments.

### Molecular Dynamics Simulations: An Alternative to Testing in the Field

One alternative to traditional testing methods is the use of the molecular dynamics (MD) technique to simulate the atomistic impacts on various substrates. Depending on the force field used, these simulations are capable of effectively modelling the bond breaking, temperature evolution, and

damage of the substrate as impacts and chemical reactions occur. Therefore, these simulations offer the unique ability to view the evolution of the substrate during impact, as opposed to simply tracking its surface erosion after the impacts have occurred. Recently, studies by Rahnamoun and van Duin [29], and Zeng et al. [30] have used MD to model the effect of AO on several commonly used polymers in the space environment. First, Rahnamoun and van Duin used the ReaxFF force field to study the effect of atomic oxygen impacts on Kapton, POSS polyamide, and amorphous silica. In this study AO was propelled towards a small substrate of each material. As atoms were sputtered due to the high energy collisions, the mass loss, temperature growth, and erosion coefficients were calculated and compared to experimental values. Results showed good agreement with experimental data and concluded that the temperature evolution on the surface was critical to predicting whether erosion and material loss would occur [29]. Building on this study, Zeng et al. used the ReaxFF force field to study the impact of atomic oxygen on the disintegration of Polyvinylidene fluoride or polyvinylidene difluoride (PVDF) and fluoropropyl polyhedral oligomeric silsesquioxanes (FP-POSS), two commonly used spacecraft polymers. Again, small simulated substrates were impacted with atomic oxygen until material loss occurred. Results showed that PVDF continuously eroded due to atomic oxygen while FP-POSS did not erode until after a specific number of AO impacts [30].

However, while these studies clearly show the promising potential of using MD to model the effect of high energy impacts, there are several limitations to the current body of research. First, while research exists for the atomic oxygen erosion of polymers, the potential for molecular dynamics to model the effect of atomic oxygen on metals has yet to be studied. Because bonding for amorphous polymers and crystalline metals is quite different, accuracy for polymers cannot be used to conclude that molecular dynamics will be accurate for metals as well. In addition, because molecular dynamics is dependent on the force field chosen by the user, the force fields chosen for metals will be unique from

polymer force fields that consist mainly of C/H/O. Force fields are also sensitive to the partial charges of the atoms in the simulation model. However, this charge is not constant and is affected by factors like environmental condition and oxidation state of the metal. In addition, the outermost orbital for metals (d- or f-) can cause more complicated chemical bonding characteristics. Furthermore, there can be multiple oxidation states and coordination numbers for a metal. All of these factors increase the challenge of simulating systems that include metals.

Second, current research on the applicability of MD is limited to energies found in the LEO. Therefore, these studies did not attempt to understand the effect of impact energy on the substrate. Moreover, findings typically only report the erosion yield and often do not consider the effect collisions may have on the remaining substrate. With increased impact is the non-eroded substrate damaged? How does this damage evolve with increasing impact energy? Unlike traditional testing which occurs on the macroscale, MD simulations occur on the atomistic scale and should be able to answer these important questions. Further, understanding the effects of impact energy on damage is crucial to material selection for future deep space missions.

## Molecular Dynamics Fundamentals

A typical MD simulation begins with known initial positions and velocities of all atoms within the system. The atomic accelerations are then calculated using an interatomic potential that defines the forces between interacting particles. With the atomic acceleration known, Newton's equations of motion are then used to predict subsequent positions and velocities. Due to their atomistic nature there are several spatial and temporal limitations to simulations that must be considered when designing the

simulations. First, due to computational limitations simulations are commonly limited to nanoscale distances. However, periodic boundary conditions can be used to create a small representative unit cell that is surrounded by image cells. Particles in the unit cell behave as being connected to one's image cells, allowing for simulation of an essentially infinite bulk. However, these periodic bulk samples are unable to model the effects of free surfaces on subsequent properties and energies. Second, depending on the potential type used a typical timestep in MD is between 0.1 – 1 fs. This means that processes in MD must occur significantly faster than would be observed on the macroscale. Significant previous research has been conducted identifying recommended time steps and simulation times to reduce temporal effects on results.

As discussed previously, the interatomic potential defines forces between atoms and is a critical component to any MD simulation. Initially, interatomic potentials began as two-body potentials such as Lennard-Jones (for Van der Waals forces) and Coloumbic (for charged particles) [31]. While these potentials still have use for many non-bonded interactions, they are unable to account for the interactions that typically occur in a larger bonded system. In contrast, the more recently developed many-body potentials consider the effects of not just two atoms, but clusters of nearby atoms. Energy is typically calculated as a sum of these interactions, and bonds are dynamic depending on the current configuration [31]. Overall, several different many-body potential types exist including embedded atom method (EAM) [32], modified embedded atom method (MEAM) [33], Tersoff [34] and ReaxFF [35].

## EAM/MEAM

Originally proposed by Daw and Baskes, the EAM potential was formulated around the quasiautom theory and was developed to avoid the problem of defining an accurate volume [32]. This

method was originally proposed since an incorrect volume would prevent the accurate representation of elastic properties of the solid. Therefore, volume dependency was avoided by using the density, which is always definable in a system, to determine the electron embedding energy [32]. The total energy in the EAM potential is then defined as the summation of the pairwise interactions combined with a second term that describes the energy in embedding each atom into the electron based density formed by its nearest neighbour atoms as per equation 4:

$$E = \sum_i F_i(\rho_{h,i}) + \frac{1}{2} \sum_{\substack{i,j \\ i \neq j}} \phi_{ij}(r_{ij}) \quad (4)$$

where,  $\rho_{h,i}$  is the host electron density at atom  $i$  due to the remaining atoms in the system,  $F_i(\rho_{h,i})$  is the energy to embed atom  $i$  into the background electron density  $\rho$ , and  $\phi_{ij}(r_{ij})$  is the core-core pair repulsion between atoms  $i$  and  $j$  separated by the distance  $(r_{ij})$

This embedding energy term is calculated using two loops over all neighbour atoms. The first loop allows the function to be evaluated for each individual atom by summing electron densities, while the second is used to determine the force on each atom based on its energy contribution to neighbour atoms.

Building on the EAM potential, the MEAM potential, developed by Lee et al. [33], also follows the form of equation 1. However, the MEAM potential also adds an angle dependency to the embedding energy term. Therefore, the MEAM potential is likely more suitable for FCC, BCC, and hexagonal close packed (HCP) crystal structures commonly found in metals [33].

## Tersoff

In contrast to the EAM and MEAM potentials, the Tersoff potential is bond order based, and can therefore describe several different bonding states of an atom [34]. The key concept behind the Tersoff potential is that in real systems the strength of bonding is highly dependent on the local environment. Therefore, an effective coordination number is used to describe bonding in the system. Those atoms with many neighbours form significantly weaker bonds than atoms with fewer neighbours [34]. This coordination number takes into account the number of nearest atoms, relative distances, and bond angles and is therefore a function of the local environment in the system.

## ReaxFF

Similar to the Tersoff potential, ReaxFF is another bond order based potential that allows for the dynamic simulation of bond breaking and reformation in a body. The energy in the system is calculated as a combination of the partial energy contributions from the bond, over and under coordination, lone pair, valence, torsion, Van der Waals and Coulomb energy respectively [35]. Bond order is then used to determine the interactions between all atoms in the system. The bond order accounts for contributions from various covalent bond types (sigma, pi, and double pi-bonds) as a continuous function of the distance between atoms. ReaxFF models both connectivity dependent and non-bonded interactions. Connectivity dependent reactions, valence and torsion energy, are contingent on bond order such that when bonds are broken their energy is eliminated. Non-bonded interactions, Van der Waals and coulomb interactions are calculated regardless of connectivity between every atom pair in the set up. Therefore, this combination of bonded and non-bonded interactions allows ReaxFF to describe both covalent and metallic systems. More detail on the ReaxFF method can be found in van Duin et al. [35].

## Importance of Potential

Limited research has been conducted on the ability of atomistic tension tests to predict mechanical properties. Findings from these studies have indicated that the potential chosen to model atomistic interactions may be critical to obtaining realistic results. First, Komanduri et al. [14] conducted uniaxial tension tests on single crystal metals using MD. Results showed that while the Morse potential was able to describe mechanical properties of face centered cubic (FCC) metals, it was significantly less accurate for body centered cubic (BCC) metals and suggested further investigation into the accuracy of other potentials. Similarly, Byggmatar et al. [11] used MD to model the uniaxial tension of [100] BCC Fe and Fe-Cr nanowires. Simulations were conducted using one embedded atom method (EAM) potential and one Tersoff-like bond order potential. Results demonstrated a strong dependency on chromium concentration for the Tersoff potential but a much weaker dependency for the EAM style potential. Therefore, these findings were one of the first to indicate the importance of the potential on the results of atomistic uniaxial tension simulations. However, the study did not then consider the many types of EAM potentials, or the several other potential types outside of EAM and Tersoff. The importance of potential type is also supported by the previous work of Rajabour et al. [36] who tested EAM/MEAM and Tersoff potentials for their ability to predict bulk modulus. While the study did not conduct any tension tests or measure elastic modulus, the study found severe differences in the predicted bulk modulus. Moreover, these potentials are also often being used beyond the scope of their original development, thus potentially creating further sources of error. As an example, many iron potentials have been verified against elastic constants at 0K, a non-realistic temperature significantly lower than what would typically be seen during a macroscale laboratory test [37], [38]. Therefore, using these potentials to simulate processes at room temperature may introduce unintended error. Overall, prior to attempting to use MD to understand the role of defects on mechanical properties it is critical to assess which potentials are best suited for simulating uniaxial tension tests and why.

## Knowledge Gap

Overall there are several key gaps in knowledge that must be addressed to better understand the role of atomistic defects on mechanical properties in harsh environments. These gaps in knowledge can be separated into three categories: MD simulations and mechanical properties, effect of hydrogen on microstructure, atomistic impacts in space.

### MD simulations and Mechanical Properties

1. Research has suggested that the potential type is critical to obtaining an accurate MD simulation of uniaxial tension tests. However, there is a lack of research on the effect of potential type on mechanical properties and on which potentials are most accurate for elastic modulus of BCC metals.
2. Current uniaxial tension tests typically simulate a single crystal only. On this single crystal scale the elastic modulus is dependent on the orientation and therefore cannot be compared to the experimental polycrystalline elastic moduli that is most often seen in literature. As an alternative the VRH theory can be used to estimate the polycrystalline elastic modulus given the bulk modulus and compliance matrix. However, no study has tested the accuracy of estimating macroscale polycrystalline elastic modulus from atomistic scale single crystal simulations.

### Effect of Hydrogen on Microstructure

3. Despite the importance of hydrogen accumulation at voids for both blistering and embrittlement, no study has actually quantified the effect of hydrogen alone on void formation.

4. Many studies that use MD to model the HE mechanism often do not consider the effect on both the yield stress and elastic modulus. For example, previous work was conducted on samples that were plastically deformed prior to the introduction of hydrogen and did not quantify the effect on elastic modulus. Moreover, simulations are often limited to one crystal orientation or hydrogen concentration and are therefore applicable only to the specific case considered.

#### Effect of Atomic Oxygen on Microstructure

5. AO in the LEO represents a significant source of performance degradation and a unique multiscale challenge. MD simulations however are limited only to polymers and no research has been conducted on using ReaxFF to model AO impacts on spacecraft metals.
6. Future deep space missions are likely to encounter higher energy atomistic collisions. However testing in these environments is extremely costly and complex. Current MD simulations are limited to energies found in the LEO and cannot be used to comment on the effect of impact energy on the substrate. Moreover, previous studies have focused only on the erosion rate of the substrate. While the erosion rate is an important value to consider, it does not provide an insight into the state of the substrate. As a result, there is a gap in knowledge on the damage in the remaining substrate as a function of AO impact energy

The following research papers have been prepared with the goal of better understanding the role atomistic defects play on the microstructure and mechanical properties of materials in harsh environments. The papers have been developed to address the above gaps in knowledge, all of which are essential to one day being able to better predict the performance and remaining life of materials in the harshest environments.

## References

- [1] Louthan, M., 2008, "Hydrogen Embrittlement of Metals: A Primer for the Failure Analyst," *Journal of Failure Analysis and Prevention*, **8**(3) pp. 289-307.
- [2] Ren, X., Zhou, Q., Shan, G., 2008, "A Nucleation Mechanism of Hydrogen Blister in Metals and Alloys," *Metallurgical and Materials Transactions A*, **39**(1) pp. 87-97.
- [3] Robertson, I. M., Sofronis, P., Nagao, A., 2015, "Hydrogen Embrittlement Understood," *Metallurgical and Materials Transactions A*, **46**(6) pp. 2323-2341.
- [4] Oriani, R., and Josephic, P., 1974, "Equilibrium Aspects of Hydrogen-Induced Cracking of Steels," *Acta Metallurgica*, **22**(9) pp. 1065-1074.
- [5] Birnbaum, H. K., and Sofronis, P., 1994, "Hydrogen-Enhanced Localized Plasticity—a Mechanism for Hydrogen-Related Fracture," *Materials Science and Engineering: A*, **176**(1-2) pp. 191-202.
- [6] Nagumo, M., 2004, "Hydrogen Related Failure of Steels—a New Aspect," *Materials Science and Technology*, **20**(8) pp. 940-950.
- [7] Gao, X., Wang, T., and Kim, J., 2005, "On Ductile Fracture Initiation Toughness: Effects of Void Volume Fraction, Void Shape and Void Distribution," *International Journal of Solids and Structures*, **42**(18) pp. 5097-5117.
- [8] Ortiz, M., and Ovejero-Garcia, J., 1992, "Effect of Hydrogen on Young's Modulus of AISI 1005 and 1070 Steels," *Journal of Materials Science*, **27**(24) pp. 6777-6781.
- [9] Kuopanportti, P., Hayward, E., Fu, C., 2016, "Interatomic Fe-H Potential for Irradiation and Embrittlement Simulations," *Computational Materials Science*, **111**pp. 525-531.

- [10] Zhang, T., Jiang, F., Chu, W., 1985, "Effect of Hydrogen on the Young's Modulus of Iron," Metallurgical Transactions A, **16**(9) pp. 1655-1662.
- [11] Byggmästar, J., Granberg, F., Kuronen, A., 2015, "Tensile Testing of Fe and FeCr Nanowires using Molecular Dynamics Simulations," Journal of Applied Physics, **117**(1) pp. 014313.
- [12] Brown, D., and Clarke, J. H., 1991, "Molecular Dynamics Simulation of an Amorphous Polymer Under Tension. 1. Phenomenology," Macromolecules, **24**(8) pp. 2075-2082.
- [13] Subramaniyan, A. K., and Sun, C. T., 2008, "Continuum Interpretation of Virial Stress in Molecular Simulations," International Journal of Solids and Structures, **45**(14) pp. 4340-4346.
- [14] Komanduri, R., Chandrasekaran, N., and Raff, L. M., 2001, "Molecular Dynamics (MD) Simulation of Uniaxial Tension of some Single-Crystal Cubic Metals at Nanolevel," International Journal of Mechanical Sciences, **43**(10) pp. 2237-2260.
- [15] Morrissey, L. S., Handrigan, S. M., Subedi, S., 2019, "Atomistic Uniaxial Tension Tests: Investigating various Many-Body Potentials for their Ability to Produce Accurate Stress Strain Curves using Molecular Dynamics Simulations," Molecular Simulation, **45**(6) pp. 501-508.
- [16] Meyers, M.A., and Chawla, K.K., 2008, "Mechanical behavior of materials," Cambridge university press, .
- [17] Den Toonder, J., Van Dommelen, J., and Baaijens, F., 1999, "The Relation between Single Crystal Elasticity and the Effective Elastic Behaviour of Polycrystalline Materials: Theory, Measurement and Computation," Modelling and Simulation in Materials Science and Engineering, **7**(6) pp. 909.

- [18] Song, J., and Curtin, W., 2013, "Atomic Mechanism and Prediction of Hydrogen Embrittlement in Iron," *Nature Materials*, **12**(2) pp. 145-151.
- [19] Xie, W., Liu, X., Chen, W., 2011, "Hydrogen Hardening Effect in Heavily Deformed Single Crystal A-Fe," *Computational Materials Science*, **50**(12) pp. 3397-3402.
- [20] Le, T., and Bernstein, I., 1991, "Effects of Hydrogen on Dislocation Morphology in Spheroidized Steel," *Acta Metallurgica Et Materialia*, **39**(3) pp. 363-372.
- [21] Huang, Y., Chen, Q., Wang, Y., 1998, "Hydrogen-Induced Cracking by Nanovoids in 310 Stainless Steel," *Science in China Series E: Technological Sciences*, **41**(4) pp. 372-382.
- [22] Lv, G., Zhang, M., Zhang, H., 2018, "Hydrogen Diffusion and Vacancy Clusterization in Iron," *International Journal of Hydrogen Energy*, **43**(32) pp. 15378-15385.
- [23] Yu, X., Gou, F., and Tian, X., 2013, "Molecular Dynamics Study of the Effect of Hydrogen on the Mechanical Properties of Tungsten," *Journal of Nuclear Materials*, **441**(1-3) pp. 324-330.
- [24] Banks, B. A., Rutledge, S. K., Brady, J. A., 1989, "Atomic Oxygen Effects on Materials," .
- [25] Zhang, J., and Minton, T. K., 2001, "Production of Volatile CO and CO<sub>2</sub> from Oxidized Polyethylene and Graphite Surfaces by Hyperthermal Atom-Surface Collisions," *High Performance Polymers*, **13**(3) pp. S467-S482.
- [26] Srama, R., Ahrens, T.J., Altobelli, N., 2004, "The Cassini-Huygens Mission: Orbiter in Situ Investigations Volume 2," Springer Netherlands, Dordrecht, pp. 465-518.

- [27] Parker, E. N., 1953, "The Interstellar Structures. I. Gas Clouds." *The Astrophysical Journal*, **117**pp. 169.
- [28] Hoang, T., Lazarian, A., Burkhart, B., 2017, "The Interaction of Relativistic Spacecrafts with the Interstellar Medium," *The Astrophysical Journal*, **837**(1) pp. 5.
- [29] Rahnamoun, A., and Van Duin, A., 2014, "Reactive Molecular Dynamics Simulation on the Disintegration of Kapton, POSS Polyimide, Amorphous Silica, and Teflon during Atomic Oxygen Impact using the Reaxff Reactive Force-Field Method," *The Journal of Physical Chemistry A*, **118**(15) pp. 2780-2787.
- [30] Zeng, F., Peng, C., Liu, Y., 2015, "Reactive Molecular Dynamics Simulations on the Disintegration of PVDF, FP-POSS, and their Composite during Atomic Oxygen Impact," *The Journal of Physical Chemistry A*, **119**(30) pp. 8359-8368.
- [31] Plimpton, S. J., and Thompson, A. P., 2012, "Computational Aspects of Many-Body Potentials," *MRS Bulletin*, **37**(5) pp. 513-521.
- [32] Daw, M. S., and Baskes, M. I., 1984, "Embedded-Atom Method: Derivation and Application to Impurities, Surfaces, and Other Defects in Metals," *Physical Review B*, **29**(12) pp. 6443-6453.
- [33] Lee, T., Robertson, I., and Birnbaum, H., 1990, "TEM in Situ Deformation Study of the Interaction of Lattice Dislocations with Grain Boundaries in Metals," *Philosophical Magazine A*, **62**(1) pp. 131-153.
- [34] Tersoff, J., 1988, "New Empirical Approach for the Structure and Energy of Covalent Systems," *Physical Review B*, **37**(12) pp. 6991.

[35] van Duin, A. C. T., Dasgupta, S., Lorant, F., 2001, "ReaxFF: A Reactive Force Field for Hydrocarbons," The Journal of Physical Chemistry A, **105**(41) pp. 9396-9409.

[36] Rajabpour, A., Seidabadi, L., and Soltanpour, M., 2015, "Calculating the Bulk Modulus of Iron and Steel using Equilibrium Molecular Dynamics Simulation," Procedia Materials Science, **11**pp. 391-396.

[37] Chamati, H., Papanicolaou, N., Mishin, Y., 2006, "Embedded-Atom Potential for Fe and its Application to Self-Diffusion on Fe (1 0 0)," Surface Science, **600**(9) pp. 1793-1803.

[38] Mendeleev, M., Han, S., Srolovitz, D., 2003, "Development of New Interatomic Potentials Appropriate for Crystalline and Liquid Iron," Philosophical Magazine, **83**(35) pp. 3977-3994.

## Co-authorship Statement

Given the collaborative nature of science and engineering the following chapters include work that involves the contributions of co-authors. In each of the chapters below the thesis author (Liam Morrissey) is the principal author and has lead the research and manuscript preparation. Co-authors include the thesis author's supervisor (Dr. Sam Nakhla), fellow research team members (Stephen Handrigan, Doug Pratt, Sabir Subedi) and collaborators at other universities (Dr. Ali Rahnamoun). This collaboration is critical to obtaining impactful and thorough research. Specifically, contributions by the thesis author have been made in:

- i) Design and Identification of the Research Proposal: The thesis author helped develop the overall research theme with his supervisor and Suncor Energy. The thesis author along with Stephen Handrigan then demonstrated the applicability of molecular dynamics to solve many multiscale harsh environment problems. Building on these findings, the thesis author suggested and lead the expansion of the research into the space environment where molecular dynamics was used to simulate erosion and damage.
- ii) Practical Aspects of the Research: For all chapters below the thesis author developed the research question, lead the design of experiments/simulations and ran the simulations. Co-authors in these chapters assisted with initial simulation design and error solving during development of scripts.
- iii) Data Analysis: For all chapters below the thesis author conducted the data analysis from experiments and simulations and developed all figures and tables.
- iv) Manuscript Preparation: For all chapters below the thesis author was principle author, corresponding author, and prepared all manuscripts. Co-authors assisted with editing and review.

## Chapter 2: Quantifying Void Formation and Changes to Microstructure during Hydrogen Charging: A precursor to Embrittlement and Blistering

### **Authors:**

**Liam S. Morrissey\***, **Stephen M. Handrigan** and **Sam Nakhla**

### **CRedit author statement:**

**Liam S. Morrissey:** conceptualization, methodology, formal analysis, investigation, writing – original draft, **Stephen M. Handrigan:** methodology, formal analysis, investigation, writing – review and editing, **Sam Nakhla:** validation, resources, writing – review and editing, supervision

**Published:** **Morrissey, L. S.**, Handrigan, S. M., & Nakhla, S. (2019). Quantifying Void Formation and Changes to Microstructure During Hydrogen Charging: A Precursor to Embrittlement and Blistering. *Metallurgical and Materials Transactions A*, 50(3), 1460-1467.

**Abstract:** Hydrogen diffusion into the microstructure is a key first step for both hydrogen embrittlement and hydrogen blistering. Previous research has suggested that an increase in voids pre-loading can significantly affect the void growth and failure of samples during loading. However, there is a lack of knowledge on the effect of hydrogen alone on initial void fraction. Therefore, the microstructures of six samples of 13% chromium stainless steel were imaged using a computed tomography technique before and after hydrogen charging. These images were then formed into a 3D model to quantify the total void volume fraction before and after charging. Overall, charging was shown to increase void fraction by 18 times. This work provides support to the theory that an important role of hydrogen in promoting failure is to increase void production through recombination into H<sub>2</sub>.

## Introduction

### Hydrogen Damage

The introduction of diffuse hydrogen into a metal can result in hydrogen embrittlement or, in the extreme case, hydrogen induced blistering; which can lead to drastic changes in mechanical behavior [1]. Hydrogen blistering is generally understood to be a product of diffuse hydrogen accumulating and recombining at pre-existing voids. Voids are flaws in a materials microstructure where a small gap or pore exists due to either the accumulation of vacancies or the result of defects. The size of voids can range from atomistic to macroscale. As the hydrogen recombines it increases pressure within the lattice, resulting in plastic deformation of the microstructure and migration of the metal matrix to the surface, forming a 'blister' [1-2]. However, while it is accepted that void growth due to hydrogen accumulation at voids is required for blistering, a quantitative study on this void growth has never been completed.

In contrast, the actual processes behind the 'embrittlement' are much more complicated and have been the subject to extensive research forming many different theories [3]. Similar to blistering, hydrogen embrittlement first involves the diffusion of hydrogen into the microstructure of the metal. While concentrations are not high enough to cause blisters or fractures, upon loading there is a degradation of mechanical properties. Several models to explain this decreased strength have been postulated. Of these models, both hydrogen induced decohesion (HEDE) [4] and hydrogen enhanced localized plasticity (HELP) [5] have emerged as the most referenced.

First, the HEDE mechanism postulates that the accumulation of hydrogen in lattice sites weakens bond strength, which in turn leads to a reduction in the stress at rupture. Second, the HELP mechanism posits that hydrogen reduces the interaction energy between the dislocation-hydrogen pair, leading to

increased mobility of dislocations and shear localization. However, while the ability for hydrogen to increase dislocation motion has been demonstrated, the resulting effect on failure still produces debate.

### Effect of Hydrogen in Producing Vacancies

In addition to these models, a third, more recently developed model focuses less on the role of hydrogen in promoting failure and more on the role of hydrogen in producing and sustaining vacancies in the material; which may then ultimately lead to failure. In a series of experiments on charged and uncharged samples, Nagumo et al. [6] first demonstrated the role of hydrogen in promoting the growth of defects and vacancies during straining. First, samples were charged and strained to create resistance curves (R-curves) that showed the J-integral versus advanced crack length. In a comparison of curves with and without charging, charged samples showed a decrease in ductile crack growth resistance. Moreover, when attempting to match these values for calculations, increasing initial void volume fraction from 2 to 3.5% accurately reproduced the hydrogen charged sample's R-curve. Therefore, this suggests that hydrogen may be increasing the initial void fraction pre-loading. Because ductile crack growth resistance is controlled by defect formation, these studies proposed a mechanism of hydrogen related failure in which the role of hydrogen may be to enhance void formation and thus produce lower energy paths for crack propagation [6].

Related to these findings, Gao et al. [7] used finite element models to study the effect of initial void fraction on fracture toughness. This study tested various initial void fractions and demonstrated that a higher void volume fraction pre loading leads to more void interaction and a significantly higher crack growth rate. When combining the findings of Nagumo et al. and Gao et al., the need for further research becomes clear. Gao et al. has shown that increased voids pre loading can lead to faster crack growth. Moreover, Nagumo et al. has suggested, through best fitting, that hydrogen alone may be increasing initial

void fractions pre loading. However, Nagumo et al. focused only on the role of hydrogen during loading and did not first quantify the role hydrogen charging (without strain) plays on the initial void fractions.

## Purpose of Study

As can be seen from the above review, hydrogen diffusion into voids is an important first step to both hydrogen blistering and hydrogen embrittlement. In blistering, hydrogen recombines at voids and internal pressures induce plastic deformation of the metal lattice. Similarly, for embrittlement, research has suggested that hydrogen may influence initial void fraction, which, in turn, has a direct influence on behavior under loading. However, despite the importance of hydrogen accumulation at voids for both blistering and embrittlement, no study has actually quantified the effect of hydrogen on void formation. Therefore, the objective of the current study is to quantitatively determine the role hydrogen charging alone has on the void volume fraction of steel samples.

## Materials and Methods

### Sample Microstructure

The first step in this study was to determine the microstructure of the material being tested. Prior to charging, a sample of 13-Cr was cut from the bulk rod and imaged using a scanning electron microscope (SEM). The surface of the sample was polished using a series of successively finer grit sizes and etched for 20 seconds in a Villela etching reagent. Referring to Figure 2.1, the sample is an annealed 420 stainless steel with a ferritic microstructure showing clear carbide precipitates. In addition, the etching process has revealed the large primary austenite grains throughout the sample.

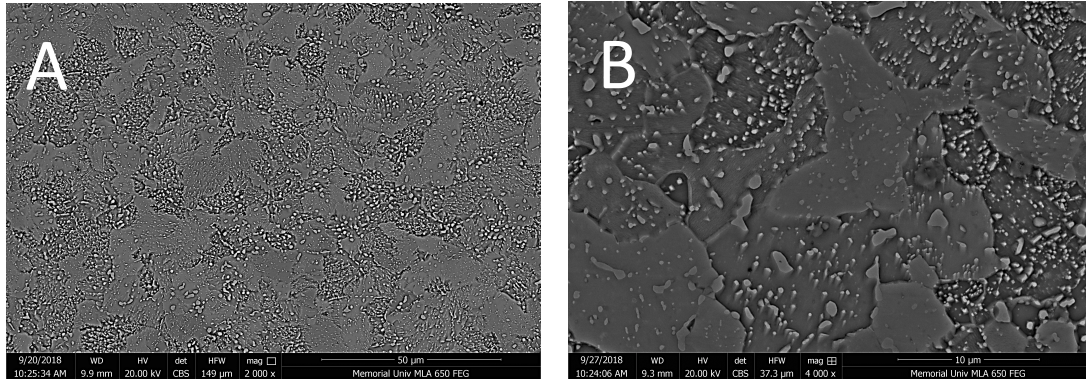


Figure 2.1 – SEM image of initial microstructure of sample at x2000 (A) and x4000 (B) magnifications

### CT Imaging

Next, six cylindrical steel samples were cut from a rod of 13-Cr stainless steel as per the dimensions of Figure 2.2. Each sample was then tapped with a screw threading that would be used in the charging process. After preparing the sample, a computed tomography (CT) imaging technique was used to quantify the initial void volume fraction pre charging. Prior to imaging scanner calibration was completed and error was no more than 0.5%, ensuring repeatability of the results. Samples were then notched on the top surface to establish an origin. Next, each sample was imaged using a Reflection Rotating 225 target head and tungsten target material from Nikon XT H225 ST system with the help of Inspect X software from Nikon. For each sample, 2000 images were taken while rotating the specimen 360 degrees. The specimen was fixed on a holder to ensure no movement occurred during rotation and two randomly positioned slices were chosen and validated to ensure information was consistently

collected. These projections were then reconstructed into a 3D model using CT pro 3D software. The spatial resolution (voxel size) of this method was 10 micron for both and pre and post charging samples.

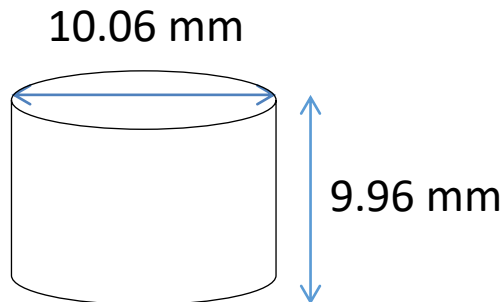


Figure 2.2 – Dimensions of stainless steel samples for charging

### Thresholding

After obtaining the 3D model the next step was to use a segmentation technique to identify and measure voids. Several different methods exist to segment 3D images of porous materials. In an effort to determine the relative accuracy of these methods, Iassonov et al. [8] compared 14 different techniques for their accuracy in quantifying porosity in various materials. The study considered global thresholding, locally adaptive, region growing, deformable surfaces, and probabilistic methods. Findings indicated that the global thresholding method was the most commonly used, was applicable to a range of materials and did not require the use of complex algorithms found in several other techniques. In addition, the resolution of this method ranged from approximately 5 to 400 micron depending on the material used. Therefore, the 10 micron resolution of the CT images tested in the current study falls within this range. Overall, Iassonov et al. [8] concluded that the Otsu global thresholding method was the only global method to be both applicable and accurate for all samples. Similar to the work of Iassonov et al., Leszczynski et al. [9] compared the Otsu global thresholding method to a local thresholding method applied to pore analysis of aluminum and nickel-chromium metallic foams. Findings indicated that both methods were accurate in predicting pore distribution and pore fraction in

the metallic foams. Therefore, given its accuracy, simplicity, and universal application, the Otsu global thresholding method was chosen for the present study.

Next, with the help of VGStudioMax 3.0 [10], this method was used to identify and measure voids in steel. The global thresholding method, as described in the work of Otsu [11], segments pores using a single gray scale threshold value. This value, as determined by the software, was defined based on the two separate regions: air and material bulk. Those gray levels that were closed in (surrounded by bulk) and were below the air threshold were then analyzed as potential pores. Similar to previous work looking at micropores, a pore was defined as being a combination of 24 or more voxels, corresponding to a minimum volume of  $0.000024 \text{ mm}^3$ [12]. Finally, the software then assigned the pores and provided statistical information on each pore. For consistency, the same set of parameters was used for scanning and analysis before and after charging.

Overall, the global thresholding method has been studied and used extensively to image the microstructure of various samples. For example, Otsuki et al. [13] used micro-CT imaging to study the structure of porous bioactive titanium implants. Pores were identified using the global grey scale method discussed above. This method was able to successfully image pore throats in the implant. In a study on the drying of asphalt, Jerjen et al. [14] used VGStudioMax and global thresholding to study pore structure in concrete aggregate. Similarly, Seo et al [15] used CT-imaging to study individual void growth during straining of steel. However, this work focused more on growth of individual voids and did not attempt to quantify total void fractions in the samples.

## Noise Reduction

Due to the nature of the material minor artifacts (e.g. beam hardening) can be present in the scans. Therefore, methods were employed both during and after imaging to reduce these effects. First, during scanning samples were imaged on a tilt to reduce overall hardening in the images. Next, a post-processing method of beam hardening correction and scattering reduction was employed to minimize the remaining artifacts from each data set. Finally, this corrected data set was used to determine the total volume fraction of voids registered. It is important to note that significant beam hardening was observed in the regions very near the surfaces due to the fact that less x-rays are observed at the surfaces relative to the center. Therefore, for both pre and post charging, volume calculation was conducted eliminating the boundary where beam hardening prevented void observation.

### Hydrogen Charging

Next, as per Figure 2.3, samples were then cathodically charged in a 0.5 mol/L  $\text{H}_2\text{SO}_4$  solution with 250 mg/L of  $\text{As}_2\text{O}_3$  added to poison the recombination reaction. A current density of  $100\text{A}/\text{m}^2$  was applied between the samples and a graphite anode for 24 hours as per the methodology described by Kim et al. [16] for charging of 316 Stainless samples. This current density was chosen to match other studies that simulated hydrogen embrittlement (without blistering) of similar carbon steels for petrochemical applications [17]. While this current rate may produce harsher embrittlement than typically found in the field, it allows for a clearer image of the effects of hydrogen on the microstructure. Samples were then submerged approximately 8mm such that the top surface with the screw was protected from galvanic corrosion. Finally, the hydrogen charged samples were then reimaged and void fraction post charging was determined using the same technique as above. Sample reimaging occurred 2 weeks after hydrogen charging, ensuring that hydrogen was able to outgas and that any changes to the microstructure were permanent.

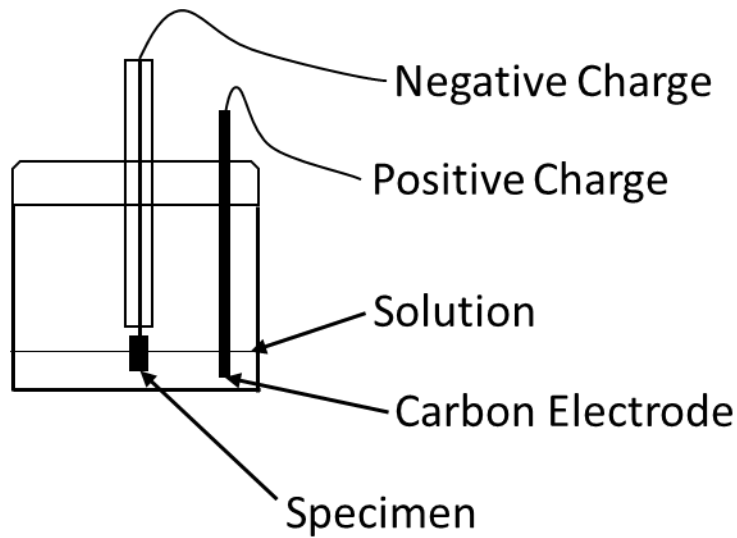


Figure 2.3 – Schematic of Hydrogen Charging Procedure

### Limitations

While the above method provides an opportunity to study void microstructure, there are limitations due to the image resolution that cannot be ignored. First, the 10 micron spatial resolution of this method means that voids and inclusions below this point will not be considered. Therefore, void expansions due to the presence of atomistic hydrogen are also obviously too small for detection. However, as per the work of Seo et al. [15], several voids are observable at this resolution. While the imaging of the smallest individual voids may not be possible, as voids grow they are more likely to coalesce and accumulate into observable larger flaws. Moreover, it is these larger scale voids, not the individual micro-vacancies, which result in higher stress concentrations and are critical to influencing behavior under loading [1, 15]. Therefore, given that thresholding and resolution was kept consistent same pre and post charging, even if the smallest micro-voids are not being accounted for, a comparison of void fraction due to hydrogen charging is still possible.

## Results and Discussion

### Initial Void Volume Fraction

Table 2.1 summarizes the void volume fraction for each sample before hydrogen charging. Coefficients of variations (COV) were used to demonstrate the relative standard deviations of samples before and after charging as per equation 1:

$$COV = \frac{100 * Std Dev}{Mean}$$

Overall, the average initial void volume fraction for the samples was 0.0035. However, the range of initial void volume fractions was between 0.0001 and 0.0068, with a COV of 81%. Therefore, the large variability of initial void ratio in the samples indicates that void volume fraction varied along the length of the pre-cut rod.

While no other study has directly measured the volume of voids in a steel sample, the initial void fraction is a commonly estimated parameter due to its necessity as an input for the GTN porosity plasticity model in *Abaqus* [18]. The initial void fraction is typically estimated by tensile tests with best fitting methods or through image analysis of a fracture surface. However, neither of these methods actually image the entire 3D structure or quantify physical void volume [19]. Reported initial void volume estimates for steels range between 0.0003 and 0.006 (Table 2.2). Therefore, five of six initial void volume fractions obtained via CT imaging in the current study fell within this range.

Table 2.1- Void volume fractions before and after hydrogen charging based on CT imaging of 6 samples.

Sample	Initial Void Volume Fraction	Final Void Volume Fraction	Ratio Final/Initial
1	0.0035	0.0062	1.77
2	0.0052	0.0067	1.29
3	0.0068	0.0078	1.15
4	0.0001	0.0039	47.18
5	0.0054	0.0088	1.63
6	0.0001	0.0053	53.00
<b>Mean:</b>	0.0035	0.0065	17.67
<b>Coefficient of Variation:</b>	81%	27%	

Table 2.2 - Summary of Initial void volume ratios reported in literature

Reference	Model or Experimental	Initial Void Volume Fraction (f <sub>0</sub> )
Hardin [16]	Analytical Simulations of WCB Steel	0.002
Springmann [12]	Experimental/Analytical Optimization of Structural Steel (STE 690)	0.0012
Gao [7]	Effect of Void Fraction using Finite Element Models	0.001-0.006
Kossakowski [17]	Fracture Surface examination of S235JR Steel	0.0017
Wcislik [18]	Experimental determination of GTN parameters	0.0009
Uthaisangsuk [19]	Fracture surface examination	0.0003

## Post-Charging Void Volume Fraction

Next, when looking at void volume fractions post-charging, it can be seen that the void volume fraction for all samples increased (Table 2.1) (Figure 2.4). The average post-charging void volume fraction was 0.0065 – an increase of 18 times. Overall, hydrogen charging alone, without loading, was shown to increase the void fraction in steel.

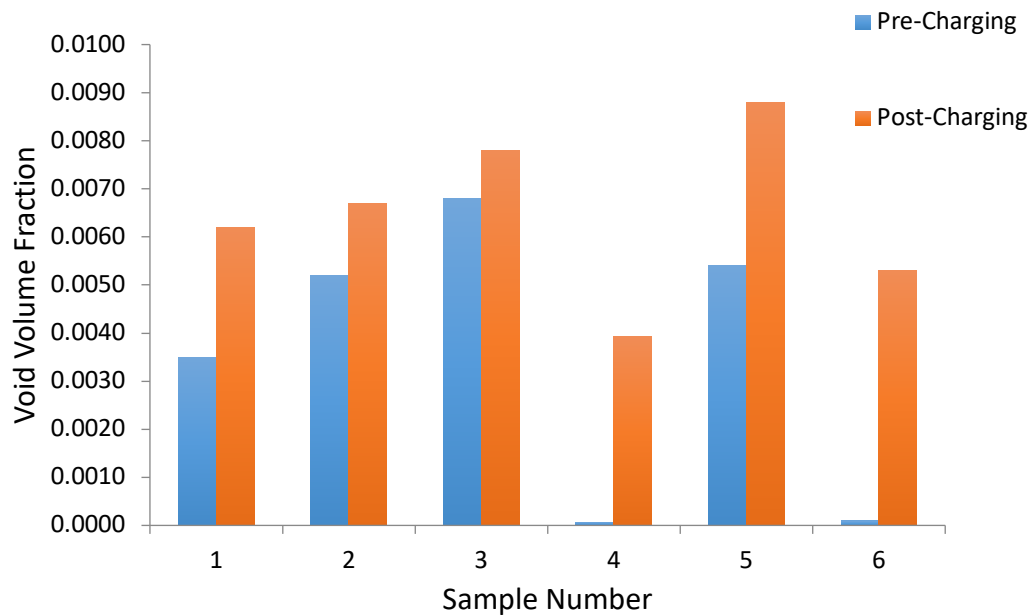


Figure 2. 4 – Void volume fraction before and after hydrogen charging

As discussed above, when attempting to explain the source of void growth, it is important to first recognize that, due to resolution restrictions in CT imaging, it is not possible for the observed voids to be simply due to atomic hydrogen. As a result, some other phenomena must be occurring to explain the void increase and microstructure damage. One potential explanation for the source of the void

growth is a micro void nucleation theory first proposed by Ren et al. [2]. In this study, SEM was used to study blister formation on various metals. After analyzing fracture surfaces, the authors proposed a nucleation mechanism in which atomic hydrogen first introduces super abundant micro vacancies into the metal. Then, under the presence of hydrogen, these micro vacancies migrate and aggregate, allowing for the formation of a hydrogen molecule. This hydrogen molecule then introduces further stresses into the material and leads to the formation of a larger vacancy cluster. Therefore, the growth of voids being imaged in the current study is likely the aggregation of microvoids as atomic hydrogen recombines into hydrogen gas, a preliminary step that could lead to a surface blister. Moreover, the current study builds on the work of Ren et al. [2] by actually quantifying this void growth.

Upon closer inspection, it can also be seen that the initial void volume fraction of the samples did not appear to significantly affect the final void volume fraction post-charging. For example, when examining the 3D reconstructed models in Figure 2.5, it is clear that samples 1 and 6 had extremely different initial void fractions (0.0035 and 0.001, respectively). However, despite this initial discrepancy, both reached a similar final void fraction after charging (0.0062 and 0.0053, respectively). This concept falls in line with void nucleation theory, which states that the role of hydrogen is to fill pre existing voids and then ultimately increase the size of these voids depending on the concentration of hydrogen. Therefore, since all samples were charged for 24 hours, it is logical that all samples would reach a similar final void fraction and that samples with a lower initial fraction would see a larger increase.

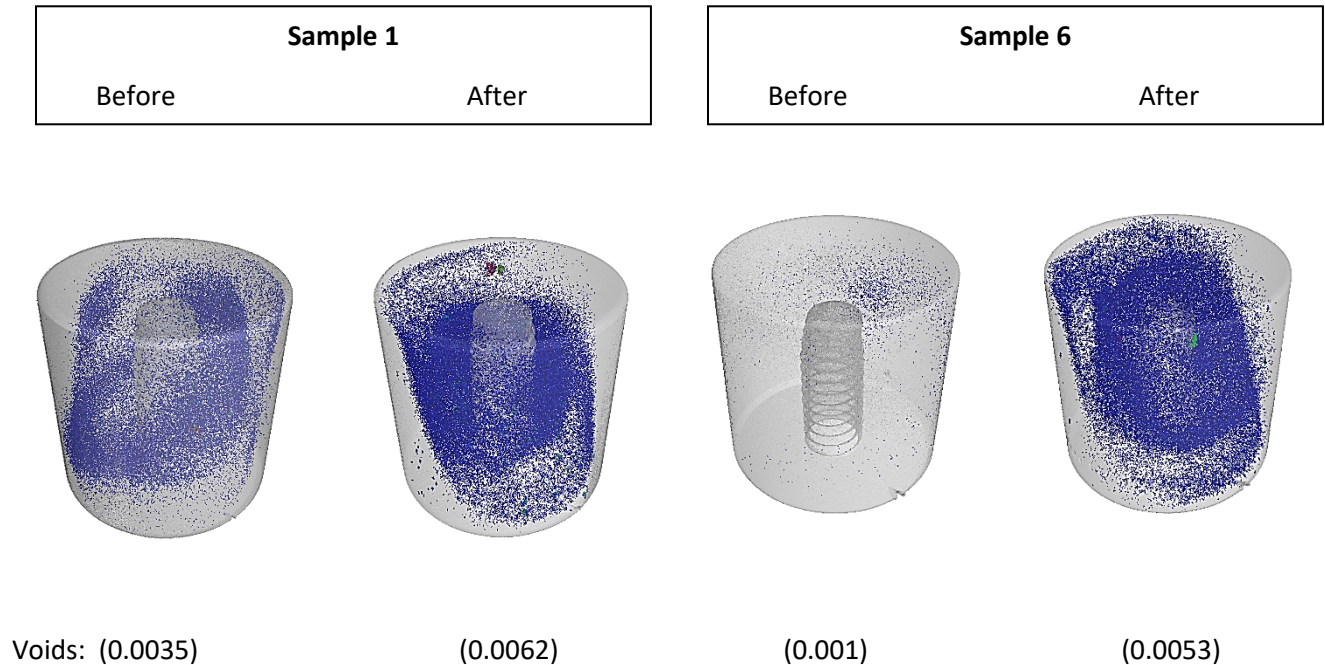


Figure 2.5 – 3D models of stainless steel samples pre and post charging for samples 1 and 6. Voids are shown as a color in the grey bulk material.

### Effect of Hydrogen on Void Distribution

While the above results show the net effect of hydrogen on void volume, they do not shed light on the distribution of these voids within the microstructure. Does hydrogen charging cause a redistribution of voids? Are voids focused in specific areas of the microstructure? To help answer these questions the 3D models of each microstructure were used to develop a dataset of all voids as a function of their x-, y-, and z-location. First, moving axially along the length of the sample, the void volume in ten 1mm ‘slices’ of the sample was calculated. In this case, the base of the sample was 0mm and the top of the sample (where the screw was placed) was 10mm (as per Figure 2.6). The total void

volume in each slice was then calculated and divided by the volume of the slice to observe how void volume fraction changes axially in the sample.

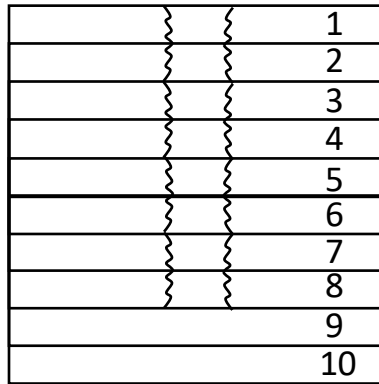
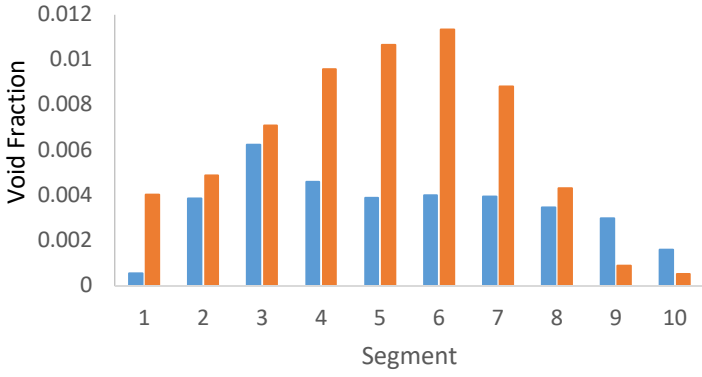


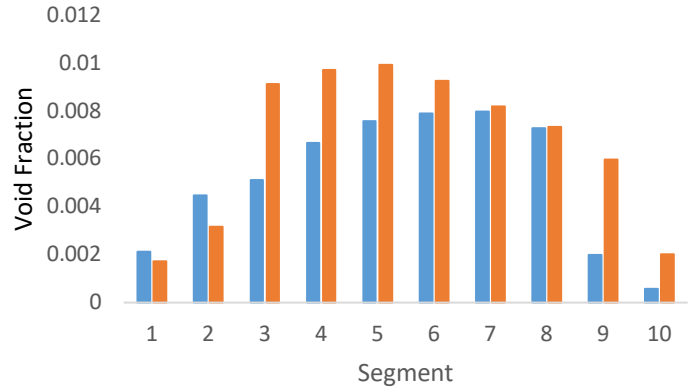
Figure 2.6 – Layout of slices used to determine void distribution axially

Referring to Figure 2.7 and Table 2.3, the highest concentrations of voids pre charging were found between 3-7mm (bulk of the sample) for all samples, with fairly even distribution within this section for four of six samples. In contrast, samples 4 and 6 had a much lower initial void fraction than the other samples and the voids were less evenly distributed throughout each sample. Post-charging, there was a net increase in void fractions, with the highest void fractions again observed between 3-7mm. The lower void volumes in the top 2-3mm of the samples is likely due to the fact that, during charging, a small part of the sample was left out of the solution to avoid interaction with the screw and solution. In addition to void fractions increasing between 3-7mm, the COV was also reduced post-charging in all samples, meaning voids were more evenly distributed axially.

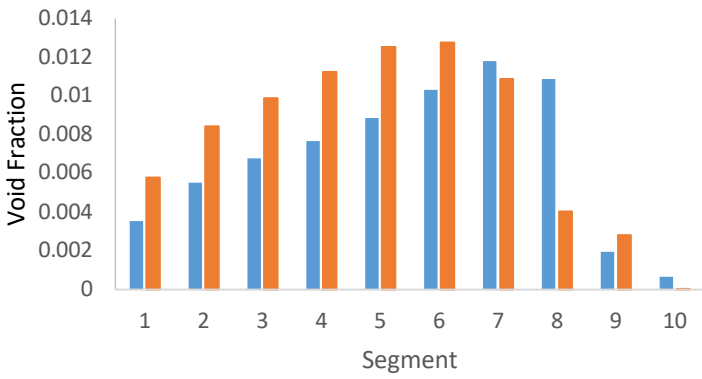
Sample 1



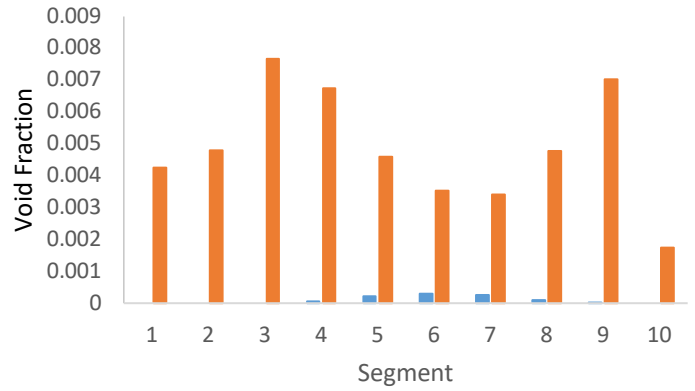
Sample 2



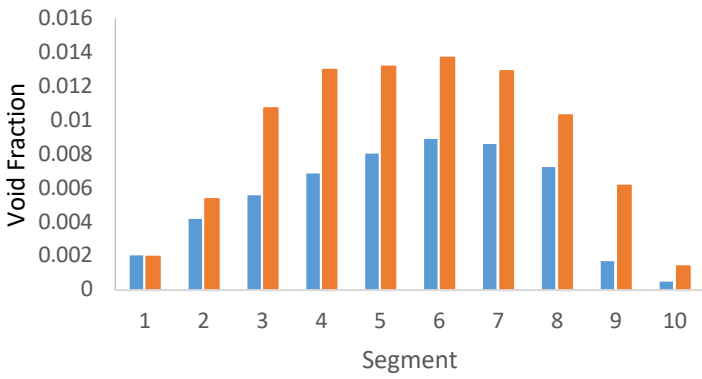
Sample 3



Sample 4



Sample 5



Sample 6

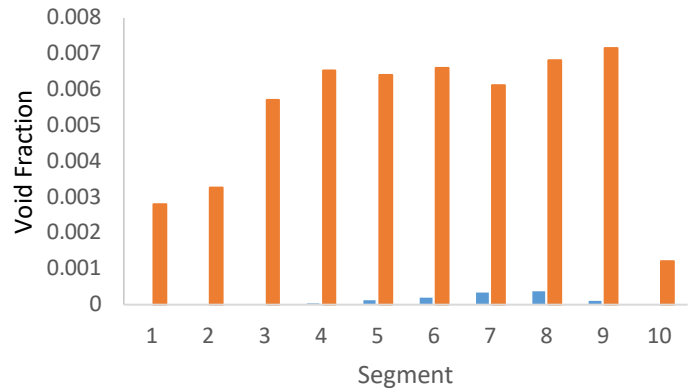


Figure 2.7 – Axial distributions of void volume fractions for 6 samples before (blue bars) and after (orange bars) charging

Table 2.3 - Axial void volume fraction distribution of samples before and after hydrogen charging

Sample	Before		After	
	Average Void Volume Fraction per Slice btw 3-7mm	Coefficient of Variation (3-7mm)	Average Void Volume Fraction per Slice btw 3-7mm	Coefficient of Variation (3-7mm)
1	0.0045	21.96%	0.0095	17.38%
2	0.0071	16.93%	0.0093	7.27%
3	0.0091	22.17%	0.0115	10.36%
4	0.0002	81.49%	0.0052	37.20%
5	0.0076	18.02%	0.0127	8.99%
6	0.0001	94.56%	0.0063	5.80%

Samples 4 and 6 also demonstrate the effect of hydrogen charging on axial distribution when initial void fractions are low and unevenly distributed. In these samples, initial void fractions between 3-7mm were low with a large COV (0.0002 with a COV of 81% and 0.0001 with a COV of 95%, respectively). After charging, void fractions increased significantly and these voids were much more evenly distributed throughout the samples than before (COV of 37% and 6%, respectively). Therefore, in the case of a sample with evenly distributed voids in the bulk, hydrogen charging increases total void volume and maintains the even distribution in the bulk of the sample. Moreover, if voids are unevenly distributed, the increased voids will be more evenly distributed throughout the bulk (3-7mm).

### SEM Analysis

After analyzing the effect of hydrogen on void fraction and distribution, the next step was to use SEM to view the surfaces of the material. First, as discussed above, the microstructure of the samples tested are ferritic with carbide precipitates and no observable martensite. However, previous research has suggested that grain structure may influence susceptibility to void growth [20]. For example, when

martensite is present within a microstructure, higher void growth is more likely due to the significant difference in hardness at the interface between ferrite and martensite [20]. Therefore, had this microstructure contained martensite, it is plausible that void growth may have been even more extreme. Future research will study various microstructures and their susceptibility to void growth.

Next, SEM was used to further investigate the two samples (one charged and one uncharged) at a better resolution than possible with the CT method. Samples were imaged using a JEOL JSM-7100F SEM with a field emission source operating at 15 kV and surfaces were not polished to allow for imaging of the voids. Figure 2.8 shows the presence of voids at sizes smaller than the 10 micron resolution from the CT scanning methods. Therefore, this both advocates the findings of the CT method used and demonstrates the need for even better accuracy in CT imaging. However, sample size optimization for CT imaging requires the balancing of two competing constraints. First, the environment of the solution requires a minimum size to ensure the sample does not degrade during charging. Second, a sample that is too large cannot be imaged with precision in the CT scanner. Therefore, the 10mm radius and height of the sample was chosen based on an optimization that balanced the two competing constraints. In addition, the voids present after charging (Figure 2.8B) were both spherically and irregularly shaped; potentially indicating some void nucleation. Therefore, while no surface blisters were observed, void nucleation likely supports the migration and clustering of microvoids initially posited by Ren [2].

Finally, a thermo electron dispersive spectrometer (EDS) was used to analyze the chemical composition of the samples and ensure that the charging process did not cause chemical changes. As can be seen in Table 2.4, there was no significant change in the atomic percentage on a cut surface of a charged and uncharged sample. The small variance observed was expected as samples, while cut from

the same initial rod, were unique and not necessarily identical, but are within a reasonable range. In addition, there was some expected local variance depending on the location selected on the surface. Therefore, the hydrogen charging process did not cause any chemical change to the sample.

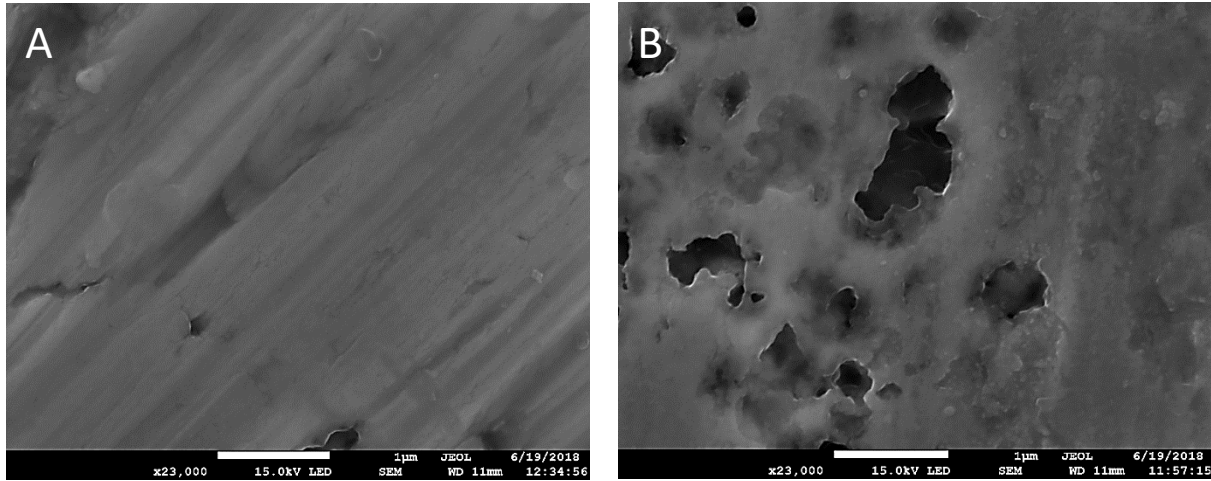


Figure 2.8 – SEM image of uncharged (A) and charged (B) sample at x23000 magnification

Table 2.4 - Atomic percentage of an uncharged and charged surface using a thermo electron dispersive spectrometer

	Atomic Percentage on Surface				
Sample	Manganese	Silicon	Chromium	Carbon	Iron
Uncharged	0.51	0.72	9.19	18.82	70.76
Charged	0.69	0.76	8.90	21.92	67.74

### Effect on Mechanical Behavior

After quantifying the role hydrogen plays on void formation, the next question to be asked is whether this increase in voids (pre-loading) can affect the material’s subsequent behavior. As observed by Chawla et al. [21] and verified by Morrissey and Nakhla using finite element analysis (FEA) [22],

increased porosity reduced the elastic modulus of a material. At low porosities, this reduction follows a fairly linear trend with increasing porosity [22]. Using the FEA model by Morrissey and Nakhla, the highest observed void fraction post charging would result in predicted reduction of 2.92%.

However, initial void volume fraction pre-loading has also been shown to affect fracture toughness of steels upon loading. As discussed above, Gao et al. [7] used finite element models to study the effect of void fraction on fracture toughness. This study tested initial void fractions of 0.001 and 0.005 and demonstrated that, despite the low net void fraction, a higher initial void fraction leads to more void interaction and a significantly higher crack growth rate. Therefore, given the fact that all charged samples saw an increase in void fraction, these newly formed voids must be considered when discussing forms of hydrogen damage. First, hydrogen blistering is generally considered a product of a harsh charging environment resulting in displaced material on the surface. However, even though the environment was not harsh enough to produce obvious surface blisters, the current study has still shown a significant effect on void microstructure. Second, hydrogen embrittlement is typically studied as a combination of hydrogen diffusion with loading [6]. However, based on the findings of the current study, hydrogen alone can cause a significant increase in void production without loading. Therefore, even if the hydrogen source were removed prior to loading and no surface blisters were observed, the increased initial void fraction could affect subsequent behavior [7]. As a result, this study supports the conclusion that hydrogen sustaining void growth should be a key feature of any hydrogen damage model.

## Conclusion

Samples of stainless steel had their microstructures imaged using a CT imaging technique. These microstructures were then used to determine void fraction pre and post charging. This is the first study to use CT imaging to demonstrate and quantify the effect of hydrogen on voids in the microstructure during charging. Hydrogen charging was shown to significantly increase initial void fraction in a material without loading. Overall, void growth due to hydrogen diffusion is an important precursor to both embrittlement and, in the extreme case, hydrogen blistering. The current work provides strong evidence that hydrogen recombination in voids can cause significant changes to the microstructure, even without loading, and obvious surface blisters.

## References

- [1] Louthan, M. R., 2008, "Hydrogen Embrittlement of Metals: A Primer for the Failure Analyst," *J. Fail. Anal. Prev.*, **8**(3), pp. 289–307.
- [2] Ren, X. C., Zhou, Q. J., Shan, G. B., Chu, W. Y., Li, J. X., Su, Y. J., and Qiao, L. J., 2008, "A Nucleation Mechanism of Hydrogen Blister in Metals and Alloys," *Metall. Mater. Trans. A*, **39**(1), pp. 87–97.
- [3] Robertson, I. M., Sofronis, P., Nagao, A., Martin, M. L., Wang, S., Gross, D. W., and Nygren, K. E., 2015, "Hydrogen Embrittlement Understood," *Metall. Mater. Trans. A*, **46**(6), pp. 2323–2341.
- [4] Oriani, R. A., and Josephic, P. H., 1974, "Equilibrium Aspects of Hydrogen-Induced Cracking of Steels," *Acta Metall.*, **22**(9), pp. 1065–1074.
- [5] Birnbaum, H. K., and Sofronis, P., 1994, "Hydrogen-Enhanced Localized Plasticity—a Mechanism for Hydrogen-Related Fracture," *Mater. Sci. Eng. A*, **176**(1–2), pp. 191–202.
- [6] Nagumo, M., 2004, "Hydrogen Related Failure of Steels—a New Aspect," *Mater. Sci. Technol.*, **20**(8), pp. 940–950.
- [7] Gao, X., Wang, T., and Kim, J., 2005, "On Ductile Fracture Initiation Toughness: Effects of Void Volume Fraction, Void Shape and Void Distribution," *Int. J. Solids Struct.*, **42**(18–19), pp. 5097–5117.
- [8] Iassonov, P., Gebrenegus, T., and Tuller, M., 2009, "Segmentation of X-ray Computed Tomography Images of Porous Materials: A Crucial Step for Characterization and Quantitative Analysis of Pore Structures," *Water Resour. Res.*, **45**(9).
- [9] Leszczyński, B., Gancarczyk, A., Wróbel, A., Piątek, M., Łojewska, J., Kołodziej, A., and Pędrys, R., 2016, "Global and Local Thresholding Methods Applied to X-Ray Microtomographic Analysis of Metallic Foams," *J. Nondestruct. Eval.*, **35**(2), p. 35.

- [10] Reinhart, C., 2008, "Industrial Computer Tomography—a Universal Inspection Tool," *17th World Conference on Nondestructive Testing*, Citeseer, pp. 25–28.
- [11] Otsu, N., 1979, "A Threshold Selection Method from Gray-Level Histograms," *IEEE Trans. Syst. Man. Cybern.*, **9**(1), pp. 62–66.
- [12] Laustsen, S., Bentz, D. P., Hasholt, M. T., and Jensen, O. M., 2010, "CT Measurement of SAP Voids in Concrete," *International RILEM Conference on Use of Superabsorbent Polymers and Other New Additives in Concrete*, RILEM Publications SARL, pp. 153–162.
- [13] Otsuki, B., Takemoto, M., Fujibayashi, S., Neo, M., Kokubo, T., and Nakamura, T., 2006, "Pore Throat Size and Connectivity Determine Bone and Tissue Ingrowth into Porous Implants: Three-Dimensional Micro-CT Based Structural Analyses of Porous Bioactive Titanium Implants," *Biomaterials*, **27**(35), pp. 5892–5900.
- [14] Jerjen, I., Poulidakos, L. D., Plamondon, M., Schuetz, P., Luethi, T., and Flisch, A., 2015, "Drying of Porous Asphalt Concrete Investigated by X-Ray Computed Tomography," *Phys. Procedia*, **69**, pp. 451–456.
- [15] Seo, D., Toda, H., Kobayashi, M., Uesugi, K., Takeuchi, A., and Suzuki, Y., 2015, "In Situ Observation of Void Nucleation and Growth in a Steel Using X-Ray Tomography," *ISIJ Int.*, **55**(7), pp. 1474–1482.
- [16] Kim, Y., Kim, Y., Kim, D., Kim, S., Nam, W., and Choe, H., 2011, "Effects of Hydrogen Diffusion on the Mechanical Properties of Austenite 316L Steel at Ambient Temperature," *Mater. Trans.*, **52**(3), pp. 507–513.
- [17] Siddiqui, R. A., and Abdullah, H. A., 2005, "Hydrogen Embrittlement in 0.31% Carbon Steel Used for Petrochemical Applications," *J. Mater. Process. Technol.*, **170**(1–2), pp. 430–435.
- [18] ABAQUS, I., 2005, "ABAQUS/Theory Manual, Version 6.5."
- [19] Springmann, M., and Kuna, M., 2005, "Identification of Material Parameters of the Gurson–Tvergaard–Needleman Model by Combined Experimental and Numerical Techniques," *Comput. Mater. Sci.*, **33**(4), pp. 501–509.
- [20] Azuma, M., Goutianos, S., Hansen, N., Winther, G., and Huang, X., 2012, "Effect of Hardness of Martensite and Ferrite on Void Formation in Dual Phase Steel," *Mater. Sci. Technol.*, **28**(9–10), pp. 1092–1100.
- [21] Chawla, N., and Deng, X., 2005, "Microstructure and Mechanical Behavior of Porous Sintered Steels," *Mater. Sci. Eng. A*, **390**(1–2), pp. 98–112.
- [22] Morrissey, L. S., and Nakhla, S., 2018, "A Finite Element Model to Predict the Effect of Porosity on Elastic Modulus in Low-Porosity Materials," *Metall. Mater. Trans. A*, **49**(7), pp. 2622–2630.

### Chapter 3: A Finite Element Model to Predict the Effect of Porosity on Elastic Modulus in Low Porosity Materials

**Authors:**

**Liam S. Morrissey\* and Sam Nakhla**

**CRedit author statement:**

**Liam S. Morrissey:** conceptualization, methodology, software, investigation, writing – original draft, **Sam Nakhla:** validation, resources, writing – review and editing, supervision

**Published:** Morrissey, L. S., & Nakhla, S. (2018). A finite element model to predict the effect of porosity on elastic modulus in low-porosity materials. *Metallurgical and Materials Transactions A*, 49(7), 2622-2630.

**Abstract:** The effect of porosity on elastic modulus in low porosity materials is investigated. First, several models used to predict the reduction in elastic modulus due to porosity are compared with a compilation of experimental data to determine their ranges of validity and accuracy. The overlapping

solid spheres model is found to be most accurate with the experimental data and valid between 3-10% porosity. Next, a FEM is developed with the objective of demonstrating that a macroscale plate with a center hole can be used to model the effect of microscale porosity on elastic modulus. The FEM agrees shows higher accuracy with experimental data than the overlapping solid spheres model.

[Introduction](#)

[Background](#)

Porosity can cause changes to a material's behavior under loading that is different than predicted. In the extreme case, these changes, if unaccounted for, could lead to major safety and economic concerns. Therefore, the ability to accurately and easily model the effect of porosity is of paramount importance during the design and testing stages. While metals are typically not intended to contain significant pores, micro pores can be present due to manufacturing defects. These pores, which at first glance may appear inconspicuous, can increase in size during service in harsh environmental conditions. For example, as discussed in chapter 1, hydrogen embrittlement is a significant concern for materials subjected to high concentrations of hydrogen. Over time, hydrogen can diffuse into the material and recombine into  $H_2$ , increasing the size of the initial voids and thus raising the porosity to a level that may effect the elastic modulus of the material [1-2]. As another example, in the emerging field of additive manufacturing micro particles are being using to create parts via the bottoms-up method. However, this method often results in porosity in the part between 0-10% [3]. Overall, while the effect of low levels of porosity on the yield stress has been comprehensively studied and captured in finite element software, the effect on the elastic modulus requires further research [4].

### Porosity and its Effect on Modulus

Significant research has been completed on the relationship between porosity and elastic modulus. Models typically agree that the relationship falls into categories based on the level of porosity. For example, the work of Zhang and Wang in [5] has recommend subdividing porosity levels into low, medium and high porosity. Where low porosity is less than 10%, medium porosity is 10-70% and, finally, high porosity is greater than 70%. Therefore the approach taken to predict the effect of porosity on elastic modulus depends first on the degree of porosity in the material. For example in low porosity materials the fundamental assumption is that voids are distributed such that there is no pore interaction, This assumption then leads to the conclusion that only void fraction, and not void

orientation or other material specific constants, effects the reduction in elastic modulus [6-7]. However, when in intermediate porosity zone the distance between pores is such that pores interact and material specific values must also be considered [8]. It is important to remember that the numbers in these ranges are not necessarily exact and could possibly be better described as extremely low porosity, extremely high porosity, and then the large middle level [8]. In low porosity materials (<10% porosity) there are several suggested relationships between porosity and elastic modulus that depend only on porosity. However, they do not predict the same influence of porosity and create a potential confusion when attempting to model a porous material. Therefore, this study attempted to clarify this confusion by evaluating these models and then demonstrating the applicability of a finite element model (FEM) to accurately predict the change in elastic modulus due to porosity.

### Low Porosity Materials

For materials of low porosity there have been both analytical and experimental studies that developed a relationship to predict the elastic modulus in terms of the porosity. In this porosity level the elastic modulus is typically determined based on the assumption that voids are not interacting and that void fraction, and not void orientation, effects the materials behavior [6]. As a result, models in the low porosity level are independent of the material and depend only on the degree of porosity [6-7].

For example, it has been suggested that a more simplified approach to modelling the elastic modulus of a porous material can be to consider the rule of mixtures used in composites to relate the modulus of two phases based on a volumetric fraction. In this case, one of the phases is considered as the solid non porous material and the other phase is the empty voids [8-9]. However, there is a lack of research on the validity of this model or its ranges of accuracy as compared to experimental data. As another example, Coble and Kingery in [10] developed a model to describe materials with spherical

pores through testing of cast alumina with porosity from 5-50%. Elastic modulus was then measured using samples in transverse bending and a model was generated that best fit experimental findings. Similarly, Maiti et al. in [11] developed a relationship between modulus and porosity by measuring the mechanical properties of three types of cellular solids as a function of density. An analytical model was then developed based on the concept that the loading of foam first causes deflection in the cells walls, which can be calculated by relating the densities of the foams to the cell walls. While this study was initially developed to model properties as a function of density, the ratio of the densities can also be related to a porosity ratio; allowing for the subsequent development of a model to predict the behavior of porous materials. Next, in [12] Lu et al. studied the effect of porosity on common industrial materials such as carbon rods, woods, ceramics and foams. The authors developed a micromechanical model that related the elastic modulus to the porosity for porosity less than 30%. This model considered the material as an isotropic matrix with  $n$  spherical voids of varying sizes. Average shear strains were then calculated for a given shear stress, allowing the shear and elastic modulus to be calculated as a function of porosity. The theoretical model showed good agreement with the experimental data presented[12]. Finally, in [13], Boccaccini and Fan developed a model to determine the effect of porosity on the elastic constants of porous ceramics. This model considers porosity as a zero density second phase and requires grain size and pore diameters that, in practice, may be cumbersome to obtain for each material in question. However, as seen in [14], if topological parameters are unavailable a power law can be used to generate a series of curves that are then matched to experimental data.

## Intermediate Porosity

It is important to note that some models developed for the intermediate porosity level have also shown accuracy with experimental values in the low porosity level. As a result, some of these analytical models were also considered for their accuracy in predicting the elastic modulus in low porosity materials. In medium porosity materials pores can interact and lead to stress redistribution in the material. Moreover, there exists a critical porosity fraction that, when reached, the material loses all stiffness and load carrying capability. Accounting for this critical porosity value, data Bert et al. in [15] presented Eq. 1 to predict the elastic modulus of medium porosity materials through an empirical observation of trends in experimental data. This model was developed based on the assumption that the ratio of porous material property to the solid material property is proportional to the ratio of minimum solid contact area to total cross-section area in the porous material [16]. The parameters  $\phi_0$  and  $n$  must be determined for each model/material by best fitting to experimental/analytical results.

$$E(\phi) = E_0 \left(1 - \frac{\phi}{\phi_0}\right)^n \quad (1)$$

Where  $E_0$  is the elastic modulus of the material without pores,  $\phi_0$  is the critical porosity value for the given material (between .37 and .97),  $\phi$  is the porosity of the material, and  $n$  is a power exponent that must be determined for each model/material.

Building on this model, in [17] Roberts and Garboczi used finite element analysis to study the influence of porosity and pore shape on the elastic properties of model porous ceramics. The study developed three different FEMs by placing spheres/ellipses in a unit cell to create various pore shapes and then best fitting the results to the model suggested by Bert in [8] to determine the  $\phi_0$  and  $n$

parameters. Predicted elastic moduli agreed well with experimental data and several models also accurately predicted the elastic modulus of materials with porosity below 10%. Therefore these models will also be considered as potential models for the low porosity level.

Similarly, Hardin and Beckermann in [8] used a FEM to determine the best fit parameters for cast steel. First, a simple tension test and radiographic measurement was performed and a FE mesh was mapped onto an object in *Abaqus*. However, due to the microscopic nature of the pores, a small representative volume with a defined porosity fraction was used. A relationship for porosity was then determined by minimizing the difference between the FEM and experimental values and best fitting the results to the model suggested by Bert in [8]. Results demonstrated that this method was accurate in the prediction of strains but had significant error in predicting the elastic modulus. The paper concluded that there was no correlation between average porosity and elastic modulus and that the reason for this error in modulus was because the FEM was a representative sample of the total porosity [8]. However, while the results may not be as useful in the prediction of elastic modulus, they serve to shed light on the importance of a FEM fully accounting for variations in porosity in the material.

### Finite Element Models

Perhaps the most commonly referenced FEM for porous metals is the porous plasticity model found in *Abaqus* [18]. This model is based on the Gurson-Needleman-Tvergaard (GTN) model originally developed by Gurson in [7] and later extended by Tvergaard in [4] for the failure of ductile materials due to void coalescence. This model defines a yield potential based on an isolated spherical void and forms the basis of the porous plasticity model currently used in *Abaqus* to predict the behavior of mildly voided materials. However, while the model is able to accurately predict micromechanical parameters such as yield stress, it is unable to account for the macro scale effects of the micro scale pores. For

example, Hardin and Beckermann in [19] investigated using the porous plasticity model to model the influence of porosity on the yielding of cast steel. As porosity was changed the only observable difference in the stress strain curves was a change in yield stress [19]. Therefore, because there was no change in the slope of linear portion of the plot, the model does not predict a change in elastic modulus due to porosity. This finding serves to highlight the confusion at hand. While studies and intuition dictate that porosity should affect the modulus, one of the most commonly used microscale models found in *Abaqus* appears to ignore or not account for the effect on elastic modulus [19].

## Purpose of Study

As can be seen from the above review, several models exist to predict the influence of porosity on elastic modulus. However, because there is no study on the ranges of validity and relative accuracy of these models there is a potential confusion when attempting to predict the elastic modulus of a low porosity material. Moreover, the GTN model, a popular microscale model in *Abaqus* for low porosity materials, only adds to the confusion by predicting a change in the yield stress and no change in the elastic modulus. As a result, *Abaqus* does not have the capability to accurately predict the elastic modulus of a porous material. To help eliminate this gap in knowledge this study focused on the evaluation of models used for materials in the low porosity level. The first objective of this study was to compare the present models and to clearly identify their validity when compared to experimental data. Next, a FEM was developed with the objective of demonstrating that a macroscale plate with a consolidated center hole can be used to account for the effect of microscale porosity on elastic modulus. Current work is devoted to study the effect of low porosity on elastic modulus in tension. Meanwhile, effort is also underway to extend the study to also include compression [5].

## Procedures

### Evaluation of Existing Models

The first step in this study was to examine experimental data to verify that there was indeed an effect of porosity on elastic modulus. This was achieved by compiling a set of previously conducted experimental data on the elastic modulus of materials with porosity ranging from 0-10%. Next, this experimental data was used to evaluate the previously suggested relationships between porosity and elastic modulus to determine their relative accuracy.

### Finite Element Model Study

After determining which relationship best predicted the effect of porosity on elastic modulus a simplified FEM was then developed using the finite element software *Abaqus*. First, a large 2D steel plate in plane stress was developed and a pressure load was applied in tension along the width. The plate was fixed in the U1 direction on its left edge to model a tension test. Dimensions and details on the plate can be found in Table 3.1. To simulate porosity in this plate varying sizes and orientations of circular pores were removed from the material. Pore sizes were identified as percentage values of the total area (Table 3.1). In other words, the proposed model can operate in a non-dimensional fashion and the geometry indicated in Table 3.1 is provided for illustration purposes.

First, a simulation was run for the plate with zero porosity and a stress strain curve was produced using the applied pressure and change in length of the plate. The slope of this curve was used to obtain the expected effective elastic modulus of 200 GPa; matching the inputted value and therefore verifying the model (Figure 2.1).

<b>Width</b>	8m
<b>Height</b>	4m
<b>Material</b>	SS Steel
<b>Elastic Modulus</b>	200 Gpa
<b>Poisson's Ratio</b>	0.2
<b>Applied Load</b>	50000Pa (tensile)
<b>Boundary Conditions</b>	Left edge: U1=0, U2 = UNSET

Table 3.1: Finite Element Plate Specifications

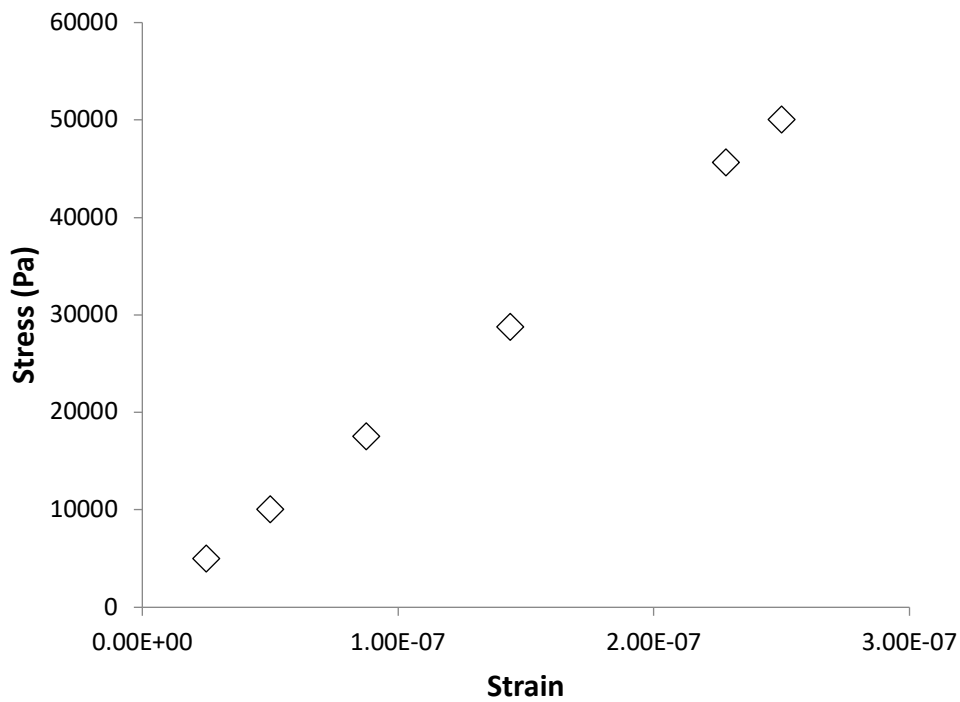


Fig. 3.1 - Stress/Strain Plot for Finite Element model of steel plate with zero porosity. The slope of the plot matches the inputted elastic modulus of 200Gpa

Next, using the python scripting language a computer code was developed in the *Abaqus* interface. This compute code enables the user to modify the pore sizes and locations and automate running their corresponding FE model in *Abaqus*. Using this script, the above test was replicated for a range of pore orientations and stress strain curves were used to calculate the elastic modulus at 2,4,6 8 and 10% porosity. A summary of the pore orientations tested is shown in Figure 2. Modified elastic moduli were then calculated based on the slope of the resulting stress strain curve and then compared to the sound modulus that was assigned to the model in *Abaqus*.

Finally, based on the findings of pore orientation, the above script was used to automate the testing of plates with a center pore accounting for 1-10% of the total surface area of the plate in *Abaqus*. The center pore simulated various degrees of consolidated porosity in the plate. Moreover, because there was no pore interaction in the model the assumption for low porosity models was supported and material specific parameters did not need to be considered [6-7]. The slope of the stress strain curve was then used to obtain the effective elastic modulus for the steel at various degrees of porosity relative to the assigned sound modulus. These results were then compared with experimental data and the most accurate models from above to demonstrate that a macroscale FEM accurately predicted the influence of porosity on elastic modulus.

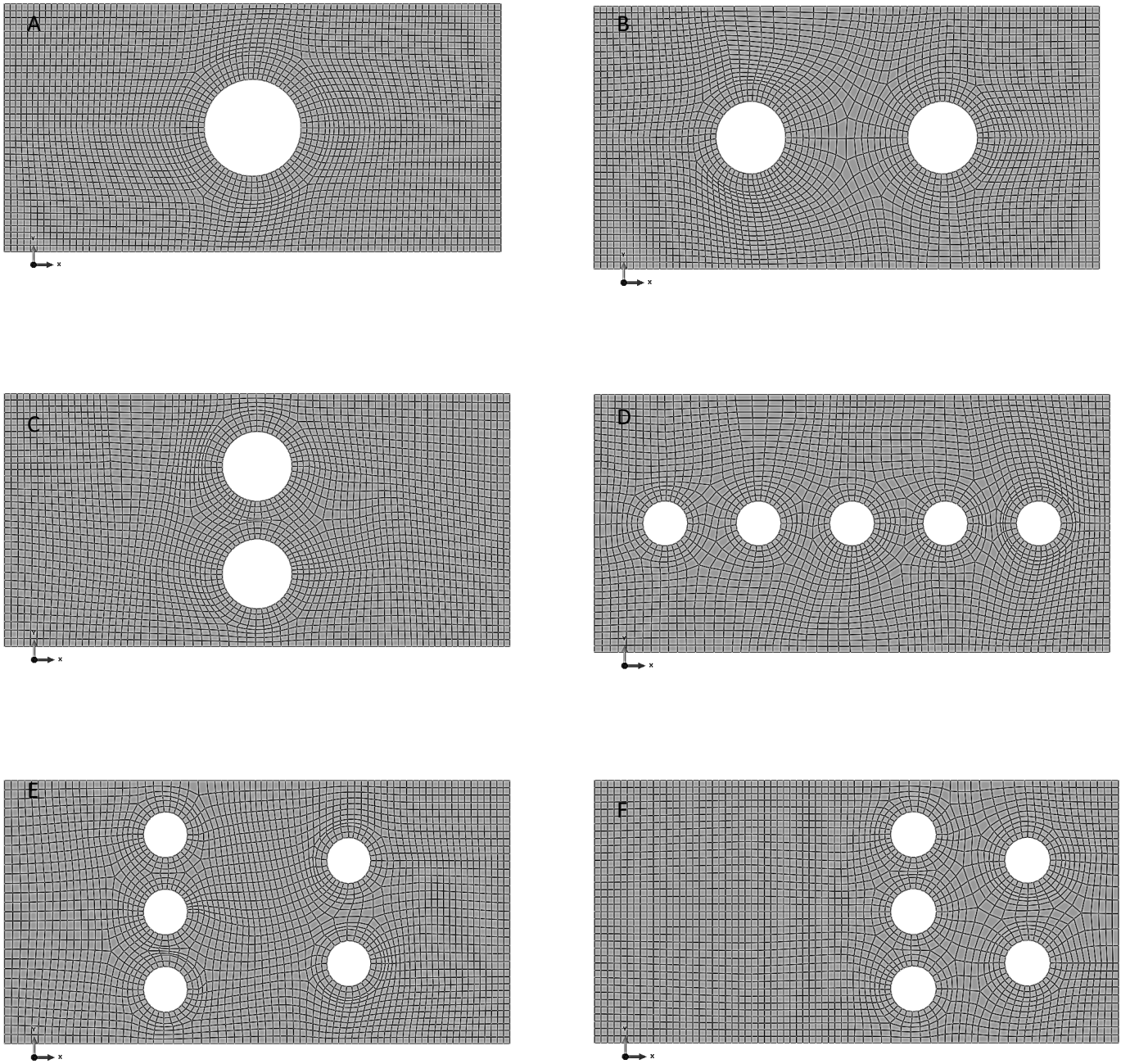


Fig. 3.2 - An example of the 6 different pore orientations (shown at 6% total porosity) tested in the Finite Element model. 1 center pore (A), 2 horizontal pores (B), 2 vertical pores (C), 5 horizontal pores (D), 5 unbalanced pores (E), 5 extreme unbalanced pores (F)

## Results and Discussion

### Effect of Porosity on Elastic Modulus

While several models exist to predict the change in elastic modulus due to porosity, their relative accuracy and ranges of validity remains unknown. To close this knowledge gap a comparison between several models and experimental data was conducted. Figure 3.2 compiles a set of experimental data on the percent reduction in elastic modulus for a range of porous materials. The data observed a linear trend of increasing percent reduction in elastic modulus with increasing porosity ( $R^2 = .77$ ). Therefore, it is clear that porosity has a direct effect on the elastic modulus of a material. The wide range of materials and preparation techniques for the experimental data also shed light upon the variables that should be considered when modelling porosity. For example, alumina values were obtained from two different sources [20-21]. In [21], Asmani et al. shaped alumina pellets via uniaxial pressing and then sintered these pellets at various temperatures to produce closed porosity shapes. The elastic modulus was then measured using a pulse echo method that calculated the transit time and longitudinal/transverse wave velocities. In contrast, the data provided by Knudsen in [20] was a compilation for a range of tests on the elastic modulus of alumina. Samples were prepared via cold and hot pressing and elastic modulus was determined both statically and dynamically. Therefore, given that both data sets closely follow the same trend, it appears that preparation/measuring techniques do not influence the reduction in elastic modulus. While the majority of materials closely followed this trend, porosity in  $\text{HfO}_2$  resulted in a lower reduction in elastic modulus than other materials. As the authors explained in [22], the  $\text{HfO}_2$  samples were prepared using a dried powder that was formed calcined, and then stabilized with approximately 30%  $\text{Er}_2\text{O}_3$ . However, this additive was shown to change the microstructure and effect the baseline elastic modulus [22]. As a result, the stabilizer may have changed the porosity of the material and lead to less of a reduction in elastic modulus. Therefore, this set of data

is included only for the sake of completeness. Moreover, when the data for  $\text{HfO}_2$  is ignored the linearity of the experimental values raises to an R-squared value of .87. Overall, because the data for several different materials followed the same linear trend it supports the conclusion that models for low porosity materials do not need to be material specific and that the pore volume is critical parameter.

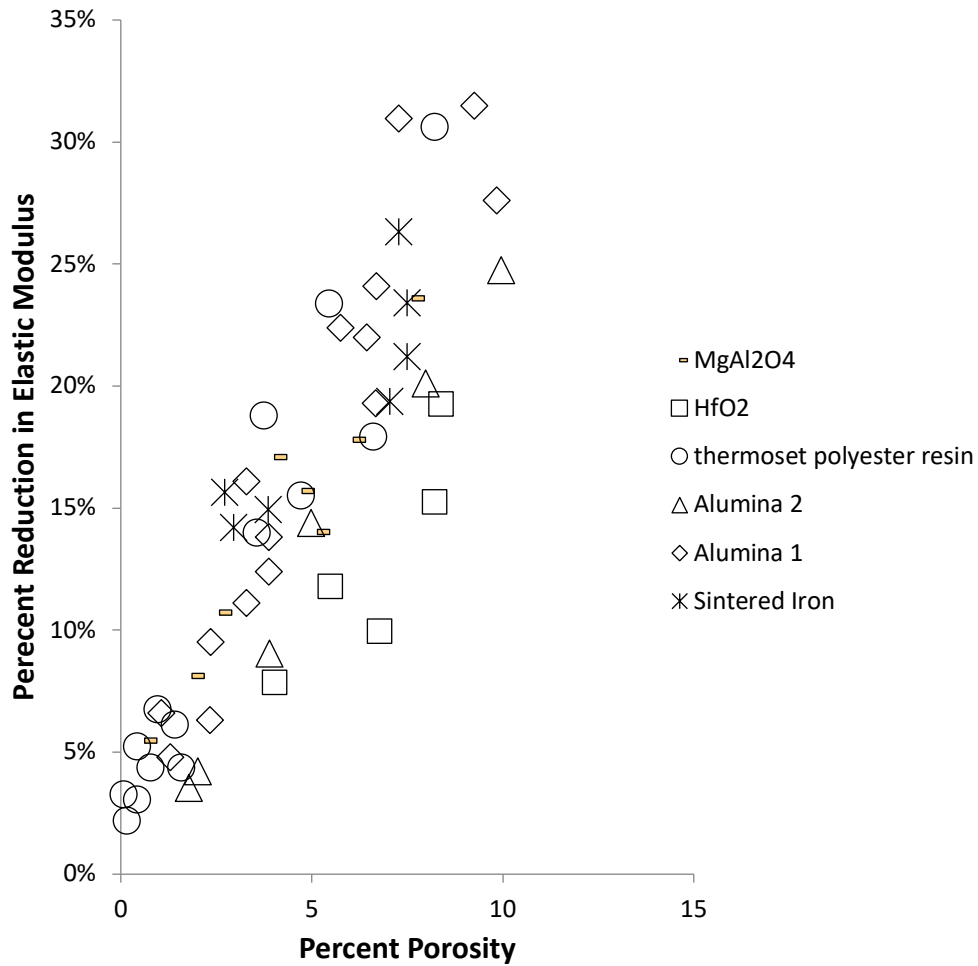


Fig. 3.3 – A compilation of experimental data for the percent reduction in elastic for various materials with porosity between 1-10% (Alumina 1 [20], Alumina 2[21], thermoset polyester resin [23],  $\text{HfO}_2$  [22], sintered Iron [24] ,  $\text{MgAl}_2\text{O}_4$  ([25])

## Evaluation of Existing Models

Next, 6 models for low porosity materials were evaluated against the experimental data above. First, the three relationships modelled by Roberts and Garboczi in [17] based on various pore orientations were considered (Eq. 2-4). These equations were developed by placing either spheres or ellipses into a unit cell such that the orientations of these pores created various pore shapes. This unit cell was then analyzed using FEA and it was found that the relative elastic modulus was independent of Poisson's ratio and followed the trend predicted by equation 1. Therefore, the analytical results of this model were best fit to Eq. 1 to determine the  $\varphi_0$  and  $n$  parameters for each geometry [17].

$$E_{ss}(\phi) = E_0 \left(1 - \frac{\phi}{0.652}\right)^{2.23} \quad (2)$$

$$E_{sp}(\phi) = E_0 \left(1 - \frac{\phi}{0.818}\right)^{1.65} \quad (3)$$

$$E_{ep}(\phi) = E_0 \left(1 - \frac{\phi}{0.798}\right)^{2.23} \quad (4)$$

Where Eq. 2 was developed for overlapping solid spheres by placing solid spheres at random points in a unit cell ( $E_{ss}$ ), Eq. 3 was developed for overlapping spherical pores by interchanging the roles of the solid and pore phase of the overlapping solid sphere mode ( $E_{sp}$ ), and Eq. 4 was developed for overlapping ellipsoidal pores by changing to spherical pores to overlapping oblate ellipsoidal pores bound by a surface ( $E_{ep}$ ).

In addition to these models, the rule of mixtures (Eq. 5) in [9], the model for materials with spherical holes developed by Coble and Kingery (Eq. 6) in [10], the model for closed cell porous materials developed by Maiti et al. (Eq. 7) in [11], the micromechanical model suggested by Lu et al. (Eq. 8) in [12], and the power law model suggested by [14] were also considered.

$$E(\phi) = E_0(1 - \phi) \quad (5)$$

$$E(\phi) = E_0(1 - 1.86\phi + 0.86\phi^2) \quad (6)$$

$$E(\phi) = E_0(1 - \phi)^3 \quad (7)$$

$$E(\phi) = E_0(1 - 2\phi)(1 + 4\phi^2) \quad (8)$$

$$E(\phi) = E_0(1 - \phi)^{2.4} \quad (9)$$

Where  $\phi$  is the porosity of the material

Figure 3.4 and table 3.2 present the predicted percent reduction in elastic modulus for each model as compared to the experimental data for low porosity materials. First from an overall perspective, all analytical models considered captured the trend of increasing percent reduction in elastic modulus with increasing porosity demonstrated by the experimental values. Between 0-2% porosity (Figure 3.4A) it is difficult to discern a clear trend and the range of predicted values was closely clustered between a 2-6% reduction in elastic modulus. However, as the porosity increased (Figure 3.4B) the range of predicted percent reduction grew to over 20% and there were stark differences in the models.

<b>Percent Porosity:</b>	<b>1</b>	<b>2</b>	<b>3</b>	<b>4</b>	<b>5</b>	<b>6</b>	<b>7</b>	<b>8</b>	<b>9</b>	<b>10</b>
FE Model	3.13%	6.29%	9.42%	12.54%	15.63%	18.47%	21.73%	24.71%	27.65%	30.54%
Eq 2 - overlapping SS	3.39%	6.71%	9.97%	13.17%	16.30%	19.37%	22.37%	25.32%	28.20%	31.02%
Eq 3 - Spherical Pores	2.01%	4.00%	5.98%	7.94%	21.73%	11.81%	13.72%	15.62%	17.50%	19.36%
Eq 4- Elliptical Pores	2.80%	5.55%	8.26%	10.93%	13.55%	16.13%	18.66%	21.16%	23.60%	26.01%
Eq 5 - Sumitomo	1.00%	2.00%	3.00%	4.00%	5.00%	6.00%	7.00%	8.00%	9.00%	10.00%
Eq 6 - Coble and Kingery	1.85%	3.69%	5.50%	7.30%	9.09%	10.85%	12.60%	14.33%	16.04%	17.74%
Eq 7 - Maiti	2.97%	5.88%	8.73%	11.53%	14.26%	16.94%	19.56%	22.13%	24.64%	27.10%
Eq 8 - Lu	1.96%	3.85%	5.66%	7.41%	9.10%	10.73%	12.31%	13.85%	15.34%	16.80%
Eq 9 – Power Law	2.38%	4.73%	7.05%	9.33%	11.58%	13.80%	15.98%	18.14%	20.26%	22.34%
Exp. Line of Best Fit	5.59%	8.16%	10.73%	13.30%	15.87%	18.44%	21.01%	23.58%	26.15%	28.72%

Table 3.2: Predicted Reduction in Modulus for the Finite Element Model, Various Common Relationships for Porosity, and a line of best fit for experimental values between 1-10%

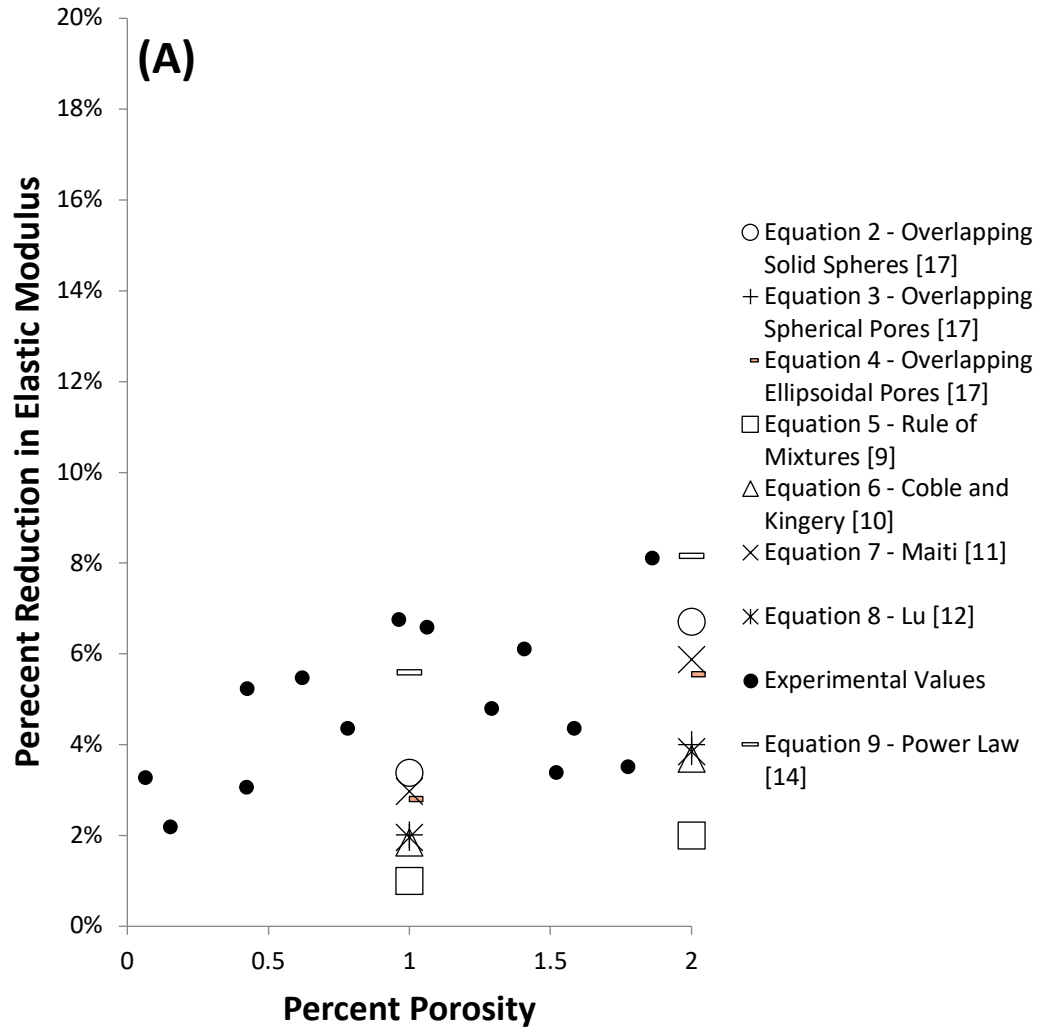
For the FEMs presented by Roberts and Garboczi in [17] it can be seen that the overlapping solid spheres model and ellipsoidal pores model both fell within the range of experimental values and were more accurate than the spherical pores model. Moreover, when compared to line of best fit of the experimental data the overlapping solid spheres model was the most accurate model tested. However, these models were all based on best fitting to equation 1, an equation developed to describe the porosity of intermediate porosity materials. A key feature in this intermediate porosity range is that pores become macroscopically connected and violate the assumption found in low porosity models; that pores do not interact. Therefore, the micromechanical geometries of these models may create potential limitations to their validity in the low porosity range. For example, in the overlapping spherical pores

model pores only become macroscopically connected at porosities above 30%. Therefore, an overlapping solid spheres microstructure is not applicable for low porosity materials, potentially explaining the inaccuracy with the experimental values between 0-10% porosity. Similarly, pores in the overlapping ellipsoidal pores model only become macroscopically connected at porosities above 20%. However, while the range of validity for this model was also outside the porosity level in question, its validity was closer to the 0-10% level than the overlapping solid spheres model. This may help explain why it followed the experimental line of best fit closer than the overlapping solid spheres model. Finally, the overlapping spherical pores model was the most accurate of the three and, unlike the other models, has a microstructure that becomes macroscopically connected at porosities above 3%. Therefore, this model is valid within the majority of the low porosity range and was most accurate when compared to the experimental line of best fit. Overall, the inaccuracies in these models are likely due to the fact that they were intended for use in the intermediate porosity zone where pores interact and orientations effect elastic modulus.

When examining the other models considered it can clearly be seen that Eq. 5, the rule of mixtures model, drastically under predicted the percent reduction in elastic modulus and did not agree with any experimental data. These findings were supported by [14] who also showed that the rule of mixtures under predicted the reduction in elastic modulus for silicon carbide. Similarly, the model suggested by Coble and Kingery (Eq. 6) under predicted the reduction in elastic modulus and agreed only with the experimental data for  $\text{HfO}_2$  presented by Dole et al. in [22]. Upon closer inspection, the constants in this equation were developed for materials with a Poisson's ratio of 0.3 [10]. Therefore material parameters have been included and the model is likely better suited for intermediate porosity where pores interact and should not be used for 0-10% porosity [10]. The model described by Lu (Eq. 8) also under predicted elastic modulus. This model was designed for materials between 0-30% porosity; a

range wider than typically seen that should encompass both the low and intermediate porosity zones [12]. Moreover, similar to the Coble and Kingery model, this equation was developed for materials with a Poisson's ratio of 0.3. As a result, this model is also likely better suited for intermediate porosity where material parameters are included and pores interact [12].

In contrast, Eq. 7, the model for closed cell porous materials developed by Maiti et al. [11] closely followed the experimental data and was the second most accurate model when compared to the line of best fit. This model was actually derived during the development of a model to predict mechanical properties of a cellular material in compression [11]. The initial model predicted the elastic modulus of a foam through the ratio of the relative densities and the elastic modulus of the solid cell wall. Eq. 7 was then derived by replacing the ratio of the densities of foam to solid by one minus the porosity, and by then replacing the elastic modulus of the cell wall with the elastic modulus of the solid material. Similarly, the power law model proposed by [14] for porous silicon carbides followed experimental values well between 0-3% porosity but increased in error at higher porosities. The reason for this discrepancy is likely because the exponent 2.4 was generated by matching curves for the power law to four data experimental data points between 0-3% porosity [14]. Therefore, the model was really only a best fit for a small portion of the low porosity range.



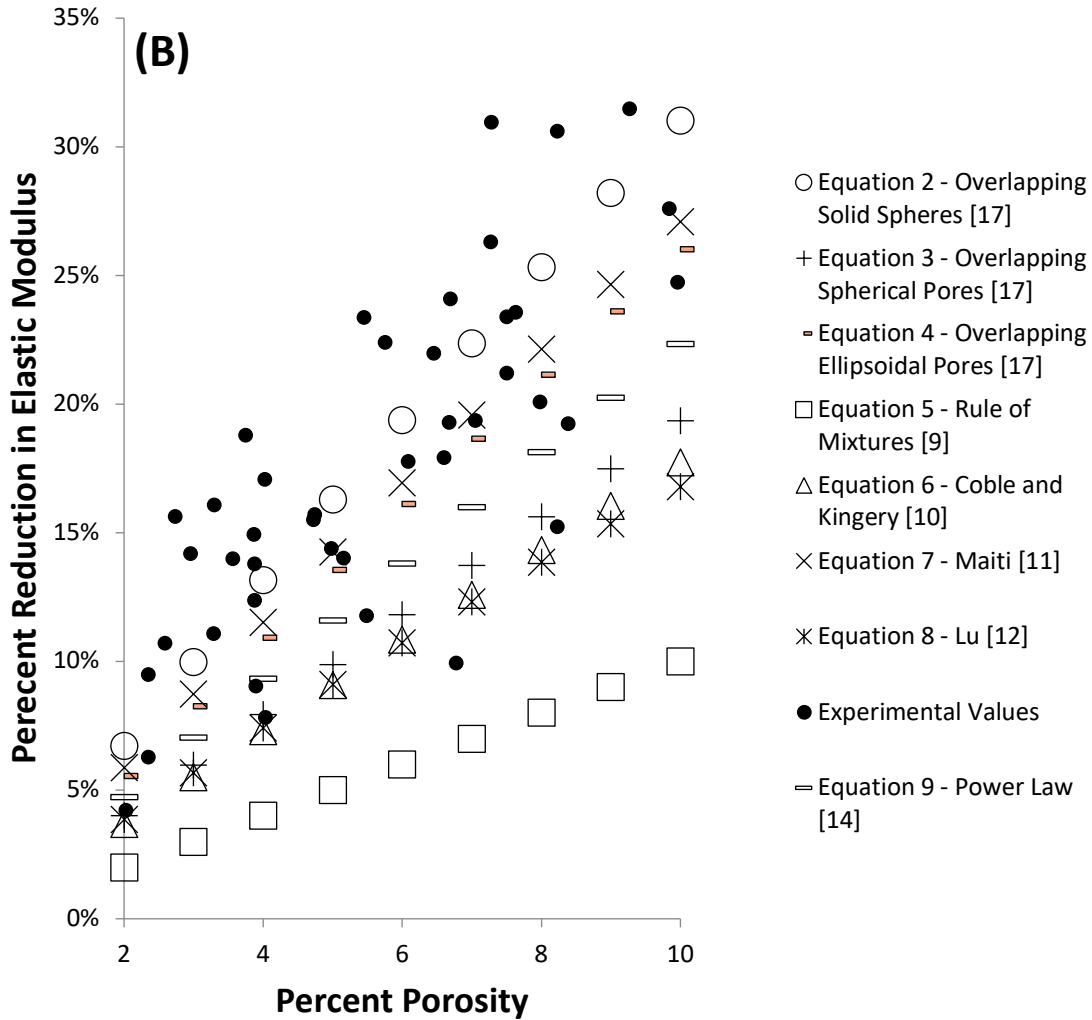


Fig. 3.4 - Predicted reduction in elastic modulus for various analytical models compared with experimental data for materials with porosity between 0-2% (A) and 2-10% (B)

### Finite Element Model

#### Effect of Pore Orientation on Elastic Modulus Comparison of Finite Element Model with Analytical Models and Experimental Values

After comparing and evaluating the existing models, the next step was to examine the applicability of a FEM for low porosity materials in *Abaqus*. Although porosity is a microscale phenomenon, its effect can be seen on both the yield stress (a microscale property) and on elastic

modulus (a macroscale property). Therefore, the fundamental question asked by this FEM was whether microscopic pores can be approximated as one bulk macroscopic hole and then be used to accurately obtain the elastic modulus, a macroscopic property. The first step to answering this question was to investigate the effect of pore orientation on elastic modulus. Therefore, the plate as described in Table 3.1 was first put in tension in *Abaqus* with various pore orientations and the resulting slope of the stress strain curve was compared to the sound nominal modulus from Table 3.1.

The effect of porosity on elastic modulus for various pore orientations was compared in Figure 5. Several different pore orientations were considered that varied the size, number, and location of the pores. The maximum error between orientations occurred at 10% porosity (8.32%), while all other errors were below 6%. Therefore, changing pore orientation did not appear to cause a significant effect of the percent reduction of elastic modulus. However, it is important to note that as porosity increased the standard deviation between the various orientations also increased. For example, at 2% porosity the standard deviation between all orientations was only 0.004 and the range in predicted reduction in elastic modulus was 5.9%-6.9%. However, at 10% porosity the standard deviation was raised by approximately seven times to 0.025 and range in values was between 27-34%. This error is likely due to the beginning of pore interactions as the model leaves the low porosity zone (where it is assumed pores do not interact and material parameters do not need to be considered) and enters the intermediate porosity zone (where pore orientations and material parameters are important). Therefore, when the total porosity in the model reaches 10% the pores are likely beginning to interact and material specific intermediate models should also be considered. In addition, it can be seen that the 1 center pore always fell within the middle of the ranges of percent reduction in elastic modulus. Therefore, to ensure that the results were not biased by orientation, the center pore was used for comparison with analytical and experimental results.

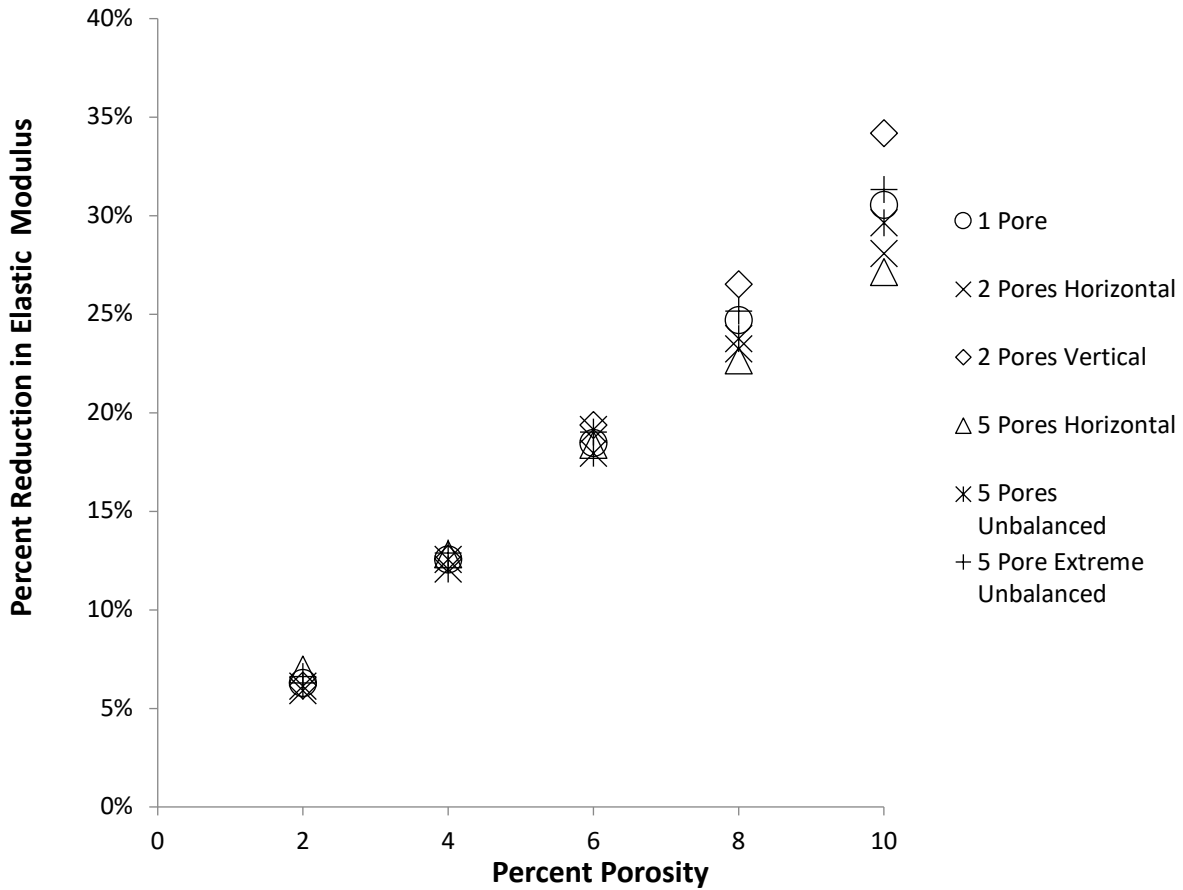


Fig. 3.5 - Effect of pore orientation on reduction of elastic modulus for low porosity materials. Note: There was no test for 5 pores spread along the vertical axis due to the required pore radii at 8 and 10% porosity.

### Comparison of Finite Element Model with Analytical Models and Experimental Values

After investigating the effect of pore orientation in a FEM, the next step was to compare the FEM with analytical and experimental results. First, Figure 3.6 compares the predicted reduction in elastic modulus for porosities between 0-10% for the proposed FEM with the analytical models. The FEM produced a highly linear relationship between porosity and elastic modulus between 1-10% porosity ( $R^2 = .9983$ ). Simulating the models response to applied load is associated to a change in porosity since all FE simulations were conducted with the same sound nominal modulus (Table 3.1).

Over the entire porosity range the overlapping solid spheres model had the lowest average error when compared to the FEM (average error of -4.38% with standard deviation of .0216) followed by Eq. 7 (average error of 8.67% with standard deviation of .0199). Therefore, the two models shown to be most accurate to the experimental data also matched best with the proposed FEM.

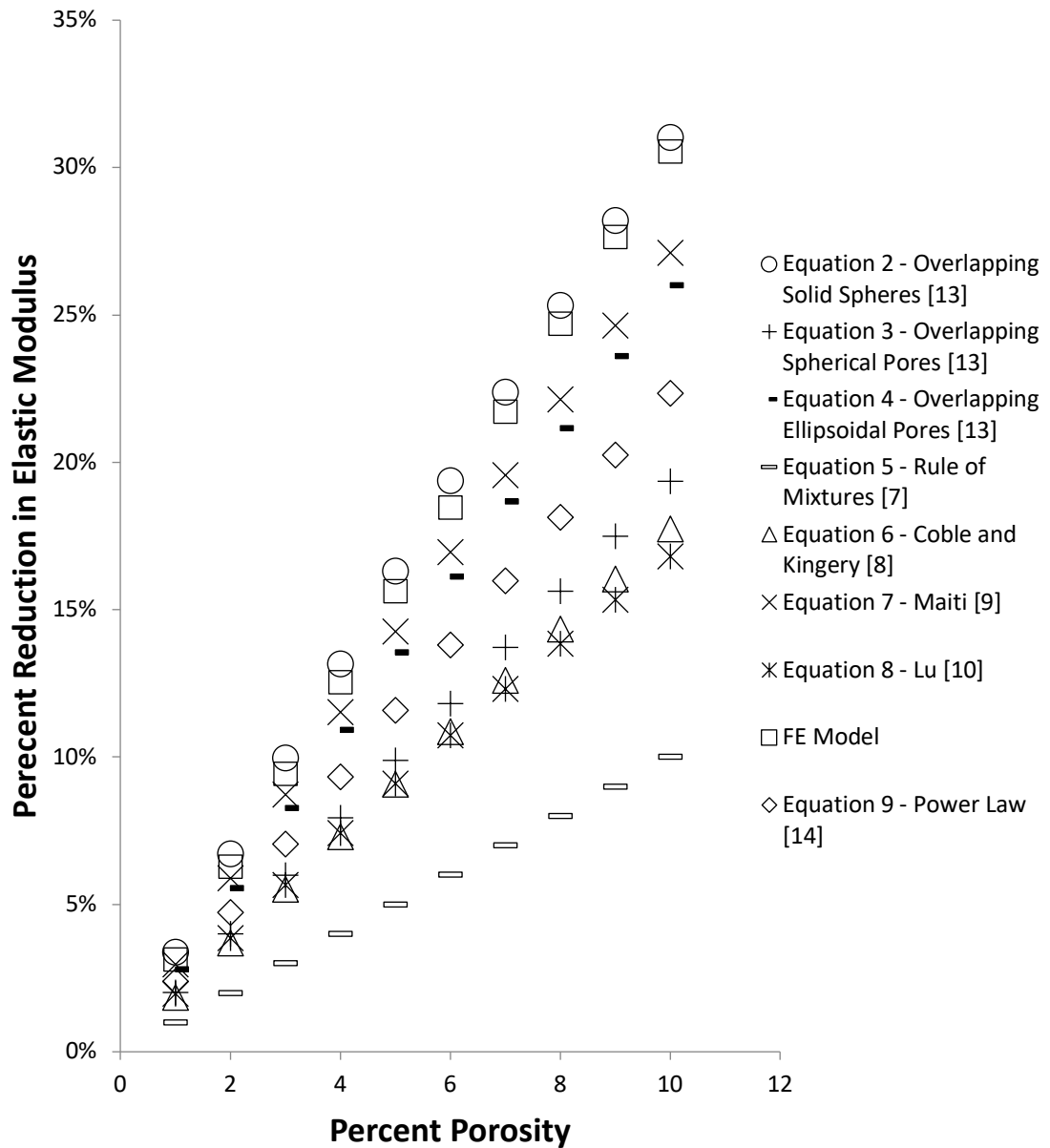


Fig. 3.6 – The predicted reduction in elastic modulus for porosities between 0-10% for the proposed Finite Element model as compared to analytical models.

Next, Figure 3.7 and Table 3.2 compare the results of the FEM with experimental data from several different low porosity materials. The experimental data and FEM both closely followed a similar linear trend with the FEM falling within the range determined by the various experiments. When comparing the FEM to a linear trend line of experimental data (as shown in Table 3.2), it can be seen that the FEM followed the experimental data better than all other models for porosities between 5-10% and was second only to the overlapping solid spheres model for all other porosities. Moreover, because the overlapping solid spheres model is not valid between 0-2%, the FEM was both more accurate and applicable over a larger range of validity. Therefore, a macroscale plate with a hole was shown to successfully predict the elastic modulus of materials with micro pores.

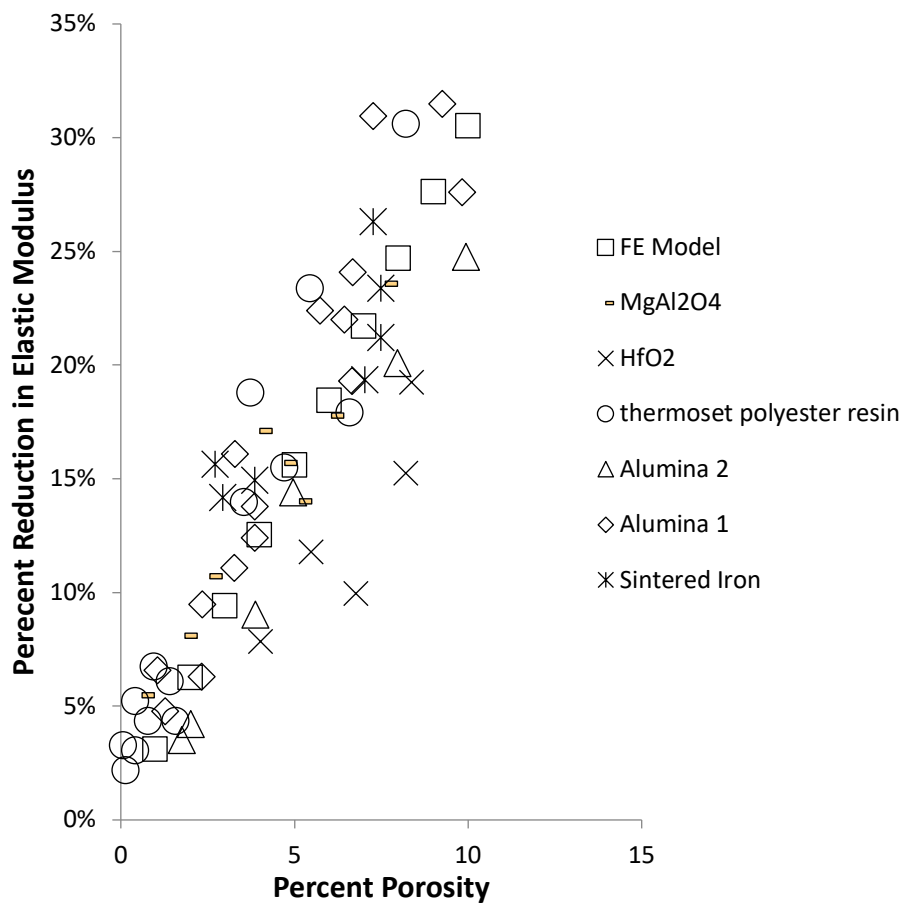


Fig. 3.7 - Predicted reduction in modulus for finite element model compared with experimental data for materials with porosity between 1-10% (Alumina 1 [20], Alumina 2[21], thermoset polyester resin [23], HfO<sub>2</sub> [22], sintered Iron [24] , MgAl<sub>2</sub>O<sub>4</sub> ([25])

## Conclusions

An accurate relationship between elastic modulus and porosity is critical to safely using materials with porosity. However, while several models exist to predict the effect of porosity on elastic modulus for low porosity materials, these relationships predict varying effects of porosity. This can potentially create confusion for engineers looking to predict the behavior of a porous material. Therefore, this study compared the commonly used models against a compilation of experimental values. While several models did not match well with experimental values, the overlapping solid spheres model Eq. (2) best agreed with the data. Next, this paper considered a large plate with a center pore in tension to demonstrate the validity of using a macroscale model to predict the effect of microscale pores on the elastic modulus using FEA. The FEM matched with experimental data better than the overlapping solid spheres model and, unlike this model, was applicable for the entire range of porosity in low porosity materials. Therefore, this study successfully demonstrated the most accurate relationship between porosity and reduction in elastic modulus and then used a FEM to improve upon this model.

## References

- [1] Liang, Y., Ahn, D. C., Sofronis, P., Dodds Jr, R. H., and Bammann, D., 2008, "Effect of Hydrogen Trapping on Void Growth and Coalescence in Metals and Alloys," *Mech. Mater.*, **40**(3), pp. 115–132.
- [2] Nagumo, M., 2004, "Hydrogen Related Failure of Steels—a New Aspect," *Mater. Sci. Technol.*, **20**(8), pp. 940–950.
- [3] Frazier, W. E., 2014, "Metal Additive Manufacturing: A Review," *J. Mater. Eng. Perform.*, **23**(6), pp. 1917–1928.
- [4] Tvergaard, V., 1981, "Influence of Voids on Shear Band Instabilities under Plane Strain Conditions," *Int. J. Fract.*, **17**(4), pp. 389–407.
- [5] Zhang, E., and Wang, B., 2005, "On the Compressive Behaviour of Sintered Porous Coppers with Low to Medium Porosities—Part I: Experimental Study," *Int. J. Mech. Sci.*, **47**(4–5), pp. 744–756.
- [6] Dewey, J. M., 1947, "The Elastic Constants of Materials Loaded with Non-rigid Fillers," *J. Appl. Phys.*, **18**(6), pp. 578–581.
- [7] Gurson, A. L., 1977, "Continuum Theory of Ductile Rupture by Void Nucleation and Growth: Part I—Yield Criteria and Flow Rules for Porous Ductile Media."
- [8] Hardin, R. A., and Beckermann, C., 2007, "Effect of Porosity on the Stiffness of Cast Steel," *Metall. Mater. Trans. A*, **38**(12), pp. 2992–3006.
- [9] Sumitomo, T., Caceres, C. H., and Veidt, M., 2002, "The Elastic Modulus of Cast Mg–Al–Zn Alloys," *J. Light Met.*, **2**(1), pp. 49–56.
- [10] Coble, R. L., and Kingery, W. D., 1956, "Effect of Porosity on Physical Properties of Sintered Alumina," *J. Am. Ceram. Soc.*, **39**(11), pp. 377–385.
- [11] Maiti, S. K., Gibson, L. J., and Ashby, M. F., 1984, "Deformation and Energy Absorption Diagrams for Cellular Solids," *Acta Metall.*, **32**(11), pp. 1963–1975.
- [12] Lu, G., Lu, G. Q. M., and Xiao, Z. M., 1999, "Mechanical Properties of Porous Materials," *J. Porous Mater.*, **6**(4), pp. 359–368.
- [13] Boccaccini, A. R., and Fan, Z., 1997, "A New Approach for the Young's Modulus-Porosity Correlation of Ceramic Materials," *Ceram. Int.*, **23**(3), pp. 239–245.
- [14] Bartkowski, P., and Spletzer, S., 2001, "Porosity Effects on the Elastic Constants of Five Varieties of Silicon Carbide Ceramic," *ARMY Res. LAB ABERDEEN PROVING Gr. MD*.
- [15] Bert, C. W., 1985, "Prediction of Elastic Moduli of Solids with Oriented Porosity," *J. Mater. Sci.*, **20**(6), pp. 2220–2224.
- [16] Rice, R. W., 2005, "Use of Normalized Porosity in Models for the Porosity Dependence of Mechanical Properties," *J. Mater. Sci.*, **40**(4), pp. 983–989.
- [17] Roberts, A. P., and Garboczi, E. J., 2000, "Elastic Properties of Model Porous Ceramics," *J. Am. Ceram. Soc.*, **83**(12), pp. 3041–3048.

- [18] ABAQUS, I., 2005, "ABAQUS/Theory Manual, Version 6.5."
- [19] Hardin, R. A., and Beckermann, C., 2011, "Measurement and Prediction of Mechanical Behavior of Cast Steel Plates with Centerline Porosity," *Proceedings of the 65th SFGA Technical and Operating Conference, Paper*.
- [20] Knudsen, F. P., 1962, "Effect of Porosity on Young's Modulus of Alumina," *J. Am. Ceram. Soc.*, **45**(2), pp. 94–95.
- [21] Asmani, M., Kermel, C., Leriche, A., and Ourak, M., 2001, "Influence of Porosity on Young's Modulus and Poisson's Ratio in Alumina Ceramics," *J. Eur. Ceram. Soc.*, **21**(8), pp. 1081–1086.
- [22] Dole, S. L., Hunter Jr, O., and Calderwood, F. W., 1980, "Elastic Properties of Stabilized HfO<sub>2</sub> Compositions," *J. Am. Ceram. Soc.*, **63**(3-4), pp. 136–139.
- [23] Phani, K. K., and Mukerjee, R. N., 1987, "Elastic Properties of Porous Thermosetting Polymers," *J. Mater. Sci.*, **22**(10), pp. 3453–3458.
- [24] Panakkal, J. P., Willems, H., and Arnold, W., 1990, "Nondestructive Evaluation of Elastic Parameters of Sintered Iron Powder Compacts," *J. Mater. Sci.*, **25**(2), pp. 1397–1402.
- [25] Porter, D. F., Reed, J. S., and III, D. L., 1977, "Elastic Moduli of Refractory Spinels," *J. Am. Ceram. Soc.*, **60**(7-8), pp. 345–349.

## Chapter 4: Atomistic Uniaxial Tension Tests: Investigating various many-body potentials for their ability to produce accurate stress strain curves using molecular dynamics simulations

### **Authors:**

**Liam S. Morrissey\***, **Stephen M. Handrigan**, **Sabir Subedi**, **Sam Nakhla**

### **CRedit author statement:**

**Liam S. Morrissey**: conceptualization, methodology, software, formal analysis, investigation, writing – original draft, **Stephen M. Handrigan**: software, validation writing – review and editing, **Sabir Subedi**: software, investigation, **Sam Nakhla**: validation, resources, writing – review and editing, supervision

**Published:** **Morrissey, L. S.**, Handrigan, S. M., Subedi, S., & Nakhla, S. (2019). Atomistic uniaxial tension tests: investigating various many-body potentials for their ability to produce accurate stress strain curves using molecular dynamics simulations. *Molecular Simulation*, 45(6), 501-508.

## Abstract

Molecular dynamics simulations, which take place on the atomistic scale, are now being used to predict the influence of atomistic processes on macro-scale mechanical properties. However, there is a lack of clear understanding on which potential should be used when attempting to obtain these properties. Moreover, many MD studies that do test mechanical properties do not actually simulate the macro-scale laboratory tension tests used to obtain them. As such, the purpose of the current study was to evaluate the various types of potentials for their accuracy in predicting the mechanical properties of iron from an atomistic uniaxial tension test at room temperature. Results demonstrated that accuracy as compared to experimental values varied significantly depending on the potential considered. In an attempt to explain this error the parametrization and testing procedures for each potential was closely investigated. Those potentials parameterized with elastic constants were significantly more accurate at predicted the elastic modulus at room temperature. Overall, these findings highlight the need to understand the capabilities and limitations of each potential before application to a problem outside of the initial intended use.

## Introduction

As described in Chapter 2, porosity and pre-existing defects can have a significant effect on subsequent macroscale elastic modulus. However, the model in Chapter 2 is applicable only on the macroscale and therefore cannot provide insight into the degradation processes that are actually occurring on the atomistic/microscale. As such, research is needed on methods to model material degradation on the scale in which these processes are physically occurring.

Molecular dynamics (MD), a specialized tool once used almost exclusively by chemists and physicists, is now being applied to a wider range of disciplines and purposes than ever before. As an example, these simulations, which take place on the atomistic/microscale scale, are now being used to predict the influence of atomistic processes on macro-scale mechanical properties. Traditionally, material properties are calculated based on uniaxial tension testing to generate stress strain curves. However, these tests occur on the macroscale and are unable to determine the effect of defects such as vacancies or impurities. While these defects may not be obvious or visible with the naked eye, they can lead to significant changes to macroscale properties. For example, Byggmatar et al. [1] studied the effect of Cr impurities in Fe-Cr nanowires and demonstrated a reduction in ultimate and yield strength with increasing Cr concentration. Similarly, in the field of additive manufacturing (3D printing) overlapping spherical particles are generating microscale porosity in many complex structures. In a study on the effect of microscale voids, Gao et al. [2] compared stress strain curves for materials with various initial void fractions. Findings indicated that a higher initial void fraction lead to more void coalescence and a higher crack growth rate. Therefore, accounting for microscale/atomistic defects is critical to an accurate prediction of macroscale mechanical behavior. One potentially promising solution to the challenge of accounting for defects is using MD to conduct atomistic tension tests. MD

simulations consider the system on an atomic scale and can model the interactions between atoms during loading. Therefore, these simulations allow for both the actual modelling of defects and the prediction of the resulting mechanical properties.

Limited research has been conducted on the ability of atomistic tension tests to predict mechanical properties. Findings from these studies have indicated that the potential chosen to model atomistic interactions may be critical to obtaining realistic results. First, Komanduri et al. [3] conducted uniaxial tension tests on single crystal metals using MD. Results showed that while the Morse potential was able to describe mechanical properties of face centered cubic (FCC) metals, it was significantly less accurate for body centered cubic (BCC) metals and suggested further investigation into the accuracy of other potentials. Similarly, Byggmatar et al. [1] used MD to model the uniaxial tension of [100] BCC Fe and Fe-Cr nanowires. Simulations were conducted using one embedded atom method (EAM) potential and one Tersoff-like bond order potential. Results demonstrated a strong dependency on chromium concentration for the Tersoff potential but a much weaker dependency for the EAM style potential. Therefore, these findings were one of the first to indicate the importance of the potential on the results of atomistic uniaxial tension simulations. However, the study did not then consider the many types of EAM potentials, or the several other potential types outside of EAM and Tersoff. The importance of potential type is also supported by the previous work of Rajabour et al. [4] who tested EAM/MEAM and Tersoff potentials for their ability to predict bulk modulus. While the study did not conduct any tension tests or measure elastic modulus, the study found severe differences in the predicted bulk modulus. Moreover, these potentials are also often being used beyond the scope of their original development, thus potentially creating further sources of error. As an example, many iron potentials have been verified against elastic constants at 0K, a non-realistic temperature significantly lower than what would

typically be seen during a macroscale laboratory test [5, 6]. Therefore, using these potentials to simulate processes at room temperature may introduce unintended error.

In summary, while research has suggested that the potential type is important in the simulation of uniaxial tension tests, further research is needed on the various potentials and their effect on predicting mechanical properties. As a result, the purpose of the current study was to address this gap by evaluating all the various types of many-body potentials available for their accuracy in predicting the mechanical properties of iron from an atomistic uniaxial tension test at room temperature.

## Molecular Dynamics

### Many-body Potentials

MD simulates the movement of atoms and molecules within a body. A typical simulation begins with known initial positions and velocities of all atoms within the system. The atomic accelerations are then calculated using an interatomic potential that defines the forces between interacting particles. With the atomic acceleration known, Newton's equations of motion are then used to predict subsequent positions and velocities. Therefore, the interatomic potential is a critical component to any MD simulation. Initially, interatomic potentials began as two-body potentials such as Lennard-Jones (for Van der Waals forces) and Coloumbic (for charged particles) [7]. While these potentials still have use for many non-bonded interactions, they are unable to account for the interactions that typically occur in a larger bonded system. In contrast, the more recently developed many-body potentials consider the effects of not just two atoms, but clusters of nearby atoms. Energy is typically calculated as a sum of these interactions, and bonds are dynamic depending on the current configuration [7]. Overall, several different many-body potential types exist including embedded atom method (EAM) [8], modified

embedded atom method (MEAM) [9], Tersoff [10] and ReaxFF [11]. Therefore, given the ability of many-body potentials to consider interactions between larger sets of atoms, the current study tested different many-body potential types for their ability to model a uniaxial tension test.

## EAM/MEAM

Originally proposed by Daw and Baskes, the EAM potential was formulated around the quasiatom theory and was developed to avoid the problem of defining an accurate volume [8]. This method was originally proposed since an incorrect volume would prevent the accurate representation of elastic properties of the solid. Therefore, volume dependency was avoided by using the density, which is always definable in a system, to determine the electron embedding energy [8]. The total energy in the EAM potential is then defined as the summation of the pairwise interactions combined with a second term that describes the energy in embedding each atom into the electron based density formed by its nearest neighbour atoms as per equation 1:

$$E = \sum_i F_i(\rho_{n,i}) + \frac{1}{2} \sum_{\substack{i,j \\ i \neq j}} \phi_{ij}(r_{ij}) \quad (1)$$

where,  $\rho_{n,i}$  is the host electron density at atom  $i$  due to the remaining atoms in the system,  $F_i(\rho_{n,i})$  is the energy to embed atom  $i$  into the background electron density  $\rho$ , and  $\phi_{ij}(r_{ij})$  is the core-core pair repulsion between atoms  $i$  and  $j$  separated by the distance  $(r_{ij})$

This embedding energy term is calculated using two loops over all neighbour atoms. The first loop allows the function to be evaluated for each individual atom by summing electron densities, while the second is used to determine the force on each atom based on its energy contribution to neighbour atoms.

Building on the EAM potential, the MEAM potential, developed by Lee et al. [9], also follows the form of equation 1. However, the MEAM potential also adds an angle dependency to the embedding energy term. Therefore, the MEAM potential is likely more suitable for FCC, BCC, and hexagonal close packed (HCP) crystal structures commonly found in metals [9].

### Tersoff

In contrast to the EAM and MEAM potentials, the Tersoff potential is bond order based, and can therefore describe several different bonding states of an atom [10]. The key concept behind the Tersoff potential is that in real systems the strength of bonding is highly dependent on the local environment. Therefore, an effective coordination number is used to describe bonding in the system. Those atoms with many neighbours form significantly weaker bonds than atoms with fewer neighbours [10]. This coordination number takes into account the number of nearest atoms, relative distances, and bond angles and is therefore a function of the local environment in the system

### ReaxFF

Similar to the Tersoff potential, ReaxFF is another bond order based potential that allows for the dynamic simulation of bond breaking and reformation in a body. The energy in the system is calculated as a combination of the partial energy contributions from the bond, over and under coordination, lone pair, valence, torsion, Van der Waals and Coulomb energy respectively (equation 2)[11]:

$$E_{system} = E_{bond} + E_{over} + E_{under} + E_{lp} + E_{val} + E_{tor} + E_{vdWaals} + E_{Coulomb} \quad (2)$$

Bond order is then used to determine the interactions between all atoms in the system. The bond order accounts for contributions from various covalent bond types (sigma, pi, and double pi-bonds) as a continuous function of the distance between atoms via equation 3:

$$BO_{ij}^i = BO_{ij}^\sigma + BO_{ij}^\pi + BO_{ij}^{\pi\pi}$$

(3)

ReaxFF models both connectivity dependent and non-bonded interactions. Connectivity dependent reactions, valence and torsion energy, are contingent on bond order such that when bonds are broken their energy is eliminated. Non-bonded interactions, Van der Waals and coulomb interactions are calculated regardless of connectivity between every atom pair in the set up. Therefore, this combination of bonded and non-bonded interactions allows ReaxFF to describe both covalent and metallic systems. More detail on the ReaxFF method can be found in van Duin et al. [11].

## Materials and Methods

To test the effectiveness of the various many-body potentials in predicting mechanical properties, atomistic scale structures were placed in tension at room temperature to generate a stress strain curve. The resulting curves were then used to determine mechanical properties of BCC iron. Simulations were performed utilizing Large-scale atomistic/molecular massively parallel simulator (*LAMMPS*), a molecular dynamics program from Sandia National Laboratories [12, 13].

First, referring to Figure 1, a 28.5 x 28.5 x 28.5 Å BCC iron structure with <100> orientations in the x, y and z directions was prepared. Similar to the work of Komanduri [3], the geometry and volume was chosen to represent the gage section found in a typical laboratory tension test (Figure 4.1A). Future

work will consider the effect of specimen simulation size and shape on properties. In total, the structure contained 2000 total atoms and periodic boundary conditions were employed in all directions. Next, for each potential a time step was selected based on a balance of computational efficiency along with maintaining minimal energy fluctuations and thus ensuring conservation of energy. For the EAM, MEAM, and Tersoff, a timestep of 1 femtosecond was chosen. In contrast, the ReaxFF potential was parameterized with a different set of units and recommends a time step no larger than 0.5 femtoseconds [14]. Therefore, for ReaxFF simulations a time step of 0.25 femtoseconds was used.

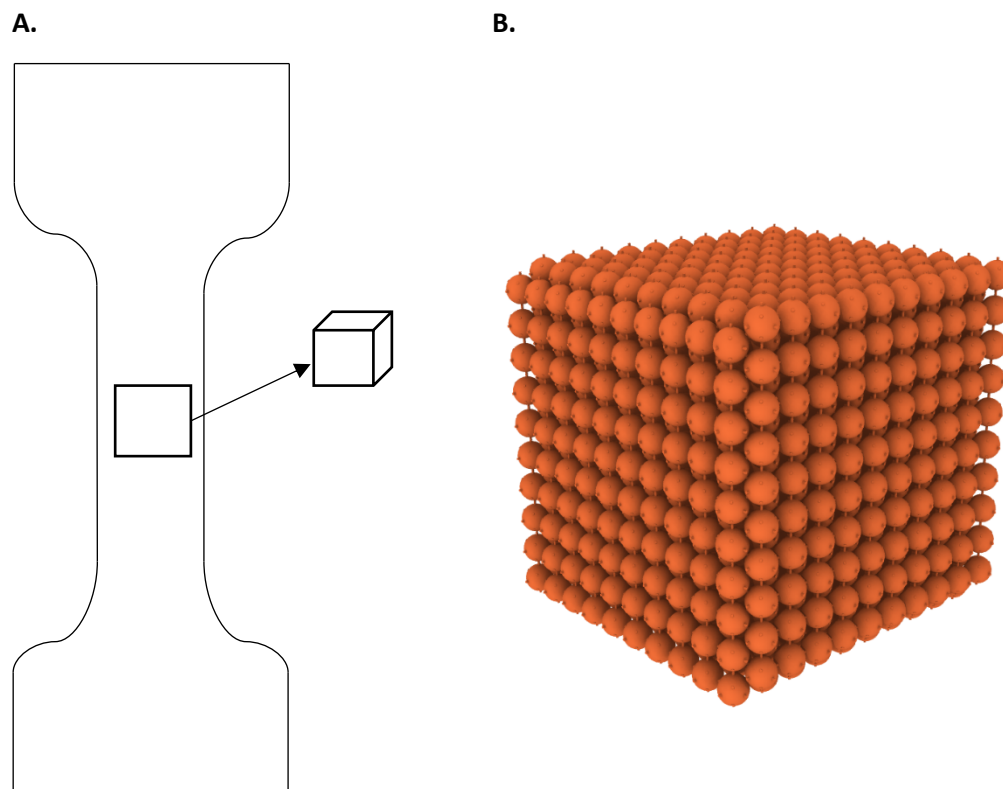


Figure 4.1 - Typical tensile test specimen with gage section (A) that then forms the iron simulation cell for molecular dynamics (B)

Next, each structure was equilibrated to room temperature (300K) using a number, pressure and temperature (*NPT*) barostat that allows the lattice to expand to a temperature of 300K while keeping the number of atoms fixed. Equilibration occurred within 50 picoseconds for all potentials tested and a damping coefficient of 100 and 1000 time steps was used for the pressure and temperature damping coefficients respectively.

After equilibration, the structure was then ready to perform the atomistic uniaxial tension test. To perform this test, each structure was deformed in the x-direction at 300K with lateral boundaries controlled to zero pressure using an *NPT* barostat to allow for natural Poisson contractions [15]. In a study on the effect of strain rate on stress strain response for molecular dynamics tension tests, Jensen et al. [15] tested a range of strain rates on various materials and concluded that strain rate did not effect the mechanical response in the linear region. Therefore, a strain rate of 0.01 per picosecond, which was within the range tested by Jensen et al., was applied to the structure (Table 4.1). Moreover, to ensure that comparable tension tests were being conducted, the strain rates were kept equal for all potentials. Total strains were 2% of the original length to ensure sampling occurred within the linear region of the stress strain curve where Hooke's law is applicable.

	<b>Potential</b>			
	<b>EAM</b>	<b>MEAM</b>	<b>Tersoff</b>	<b>ReaxFF</b>
Temperature(K)	300	300	300	300
Time Step (fs)	1	1	1	0.25
Total Simulation Time (fs)	2000	2000	2000	8000
Strain Rate (1/fs)	0.00001	0.00001	0.00001	0.00001
Temperature Damping (fs)	100	100	100	25
Pressure Damping (fs)	1000	1000	1000	250

Table 4.1 - Input parameters for *LAMMPS* simulations

Utilizing the National Institute of Standards and Technology (NIST) interatomic potentials repository, several options for each potential type were used to simulate the atomistic tension test [16]. Table 4.2 summarizes the potentials and their relevant references. In total, 3 EAM, 2 MEAM, 1 Tersoff, and 5 ReaxFF potentials were tested for their ability to predict mechanical properties from an atomistic uniaxial tension test.

## Results

Figures 2-5 provide the stress strain curves for the EAM, MEAM, Tersoff, and ReaxFF potentials, respectively. Overall, all atomistic uniaxial tension tests produced highly linear stress strain curves, thus indicating that straining was occurring in the elastic region. The slope of each stress strain curve was then used to predict an elastic modulus for each potential considered (Table 4.2). This value was then compared to previously reported experimental data for the elastic modulus of single crystal [100] pure iron at room temperature, 133.7 GPa [17]

Potential	Potential Name	Predicted Modulus (GPa)	R-Squared Value	Error relative to pure iron (133.7 GPa)
EAM	Fe_Mishin2006	130	0.9962	3.00%
	Fe_mm	142	0.9989	-5.80%
	MCM2011	172	0.9922	-28.60%
MEAM	FE_Asadi	93	0.9945	30.60%
	FE_Etesami	116	0.9925	12.90%
Tersoff	FeC_Henriksson	219	0.9983	-63.60%
Reax	FeOCHCl	182	0.9991	-36.40%
	CHOFeAlNiCuS	165	0.9988	23.30%
	Fe_O_C_H	186	0.9934	-39.10%

Table 4.2 - Predicted elastic modulus for various potentials from atomistic uniaxial tension test

### EAM Potential

There was a wide range of error for the different EAM potentials tested based on the experimental elastic modulus for single crystal iron in the [100] direction. In total, 3 different EAM potentials were tested, with predicted error ranging from only 3% to 29% (Figure 4.2). However, the methods and data used to develop these potentials sheds light upon the potential sources of this discrepancy. First, the Fe\_Mishin2006 potential by Chamati et al. [5] was the most accurate potential and tested. This potential was originally developed to describe self-diffusion of BCC iron. During parameterization the potential accurately predicted lattice properties, surface energies and elastic constants. Moreover, the potential was shown to accurately predict the thermal expansion of iron at various temperatures. Second, the Fe\_mm potential by Mendeleev et al. [6] had an error of only 5%. This potential was originally developed to describe atomic interactions of crystalline and liquid iron. Similar

to Chamati et al., the potential was accurate in predicting lattice properties and elastic constants at 0K [6]. However, no mention was made of thermal expansion coefficients. Therefore, this potential was also inaccurate in predicting elastic modulus from an atomistic stress strain curve. Finally, the MCM2011 potential by Proville et al. [18] was the least accurate of the 3 and had an error of only 29%. This potential was developed to describe dislocation motion in BCC iron crystals using quantum mechanical methods and made no attempt to test or parameterize against macro-scale elastic properties [18]. Therefore, this highlights the importance of considering single crystal elastic constants during the parameterization and testing stages of a potential.

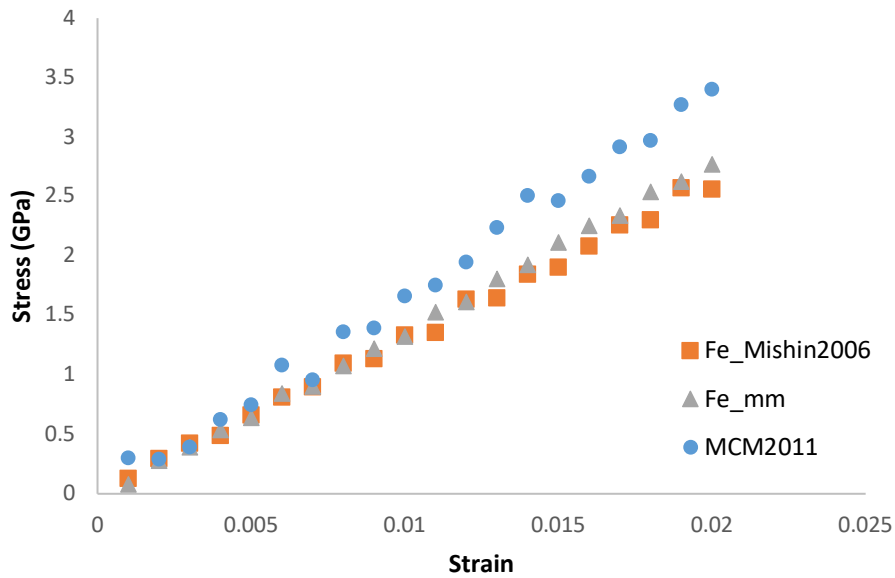


Figure 4.2 - Stress strain curves for EAM potentials

## MEAM Potential

The MEAM potential extends EAM by accounting for angular forces between the atoms. However, similar to EAM, the MEAM potentials tested also had a large range of error when compared to experimental values (12-31%) (Figure 4.3). First, the Fe\_Asadi potential by Asadi et al. was developed to investigate the solid-liquid properties of iron near its melting point [19]. Results were able to accurately describe many important high temperature properties such as melting point, latent heat, and expansion in melting but did not attempt to describe any mechanical properties [19]. Building on this work, Etesami et al. modified this iron force field (Fe\_Etesami) to include high temperature and melting point elastic constants in its development [20]. Physical properties of the iron simulations were compared against experimental values and several elastic constants showed strong agreement. However, while this study did accurately predict many elastic constants, they were generated based on indirect atom fluctuation based methods that did not physically deform the simulation box or replicate a typical tension test [20]. Therefore, as observed with the EAM potential, including single crystal elastic constants in the parameterization procedure is critical to accurately predicting the elastic modulus from a uniaxial tension test.

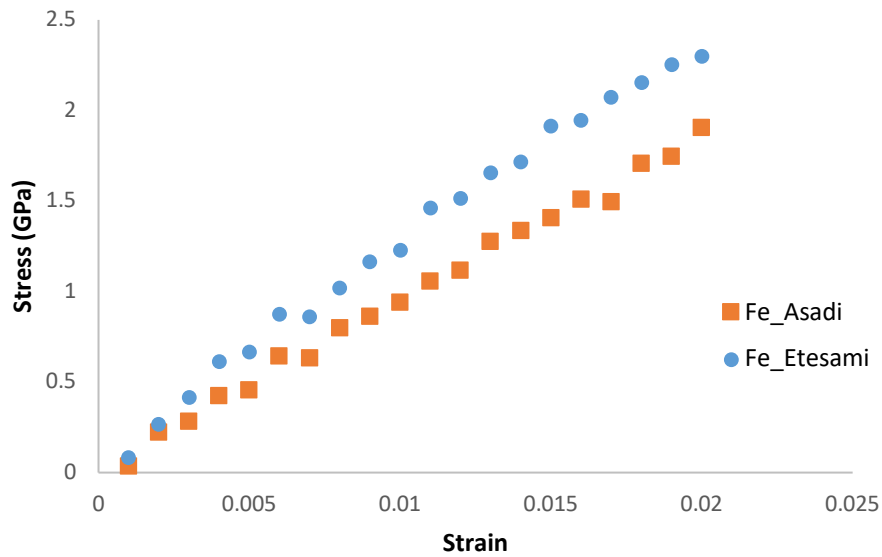


Figure 4.3 - Stress strain curves for MEAM potentials

#### Tersoff Potential

In contrast to the above EAM/MEAM potentials, the FeC\_Henriksson potential by Henriksson et al. significantly under-predicted the elastic modulus of BCC iron by over 60% (Figure 4.4). This potential was intended for use with stainless steels and was therefore parameterized based on Fe-Cr interactions and pure Cr [21]. However, elastic constants were only parameterized for cementite and not effort was made to consider elastic constants or lattice properties for pure iron. Therefore, despite the fact that this potential may at first glance appear suitable for iron systems, it was not parameterized or intended for use in pure iron simulations. This highlights the importance of closely investigating the potential development prior to application for a new simulation problem.

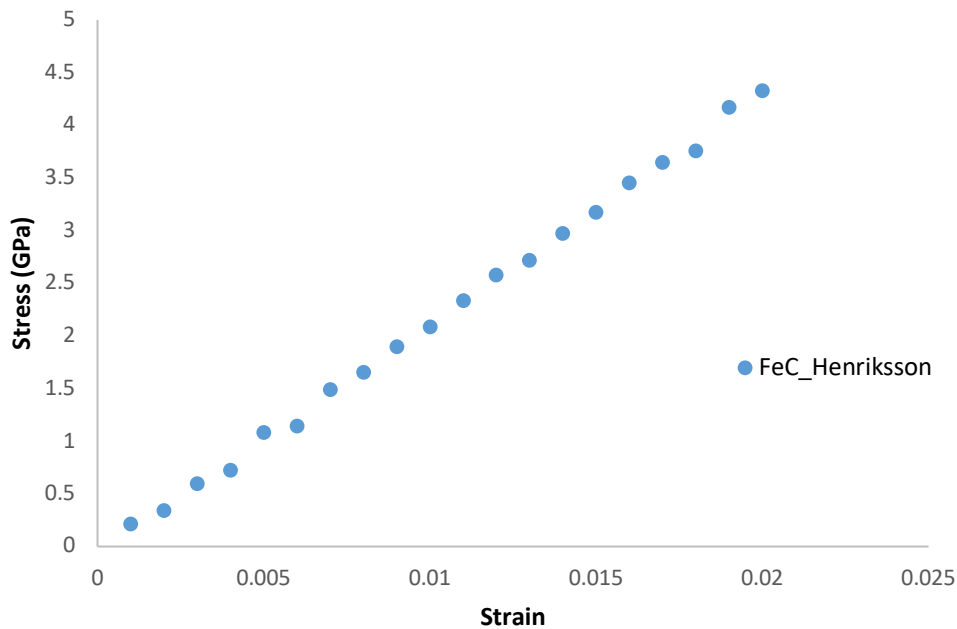


Figure 4.4 - Stress strain curves for Tersoff potential

#### ReaxFF Potential

Finally, all ReaxFF potentials had error over 20%. Depending on the potential used the single crystal elastic modulus was either over or under predicted (Figure 4.5). Similar to the Tersoff potential, ReaxFF is bond order based and is capable of handling both the covalent bonding contributions along with modelling the chemical formation and breaking of bonds. First, the CHOFeAlNiCuS potential by Rahaman et al. [22] over predicted the elastic modulus by 23%. However, this potential included several other elements and is actually a combination of two sets of potentials. The iron component of this potential was developed to describe Fe/Al/Ni alloys and no parameterization was done for iron alone [22, 23]. Moreover, a warning is included for the potential because not all crosslinking between the two potentials is completed. Therefore, this potential is not recommended to describe iron systems. In

contrast, the Fe\_O\_C\_H potential developed by Aryanpour et al. [24] under predicted the elastic modulus of BCC iron by 39%. Parameters were trained against the thermodynamics of iron oxides and energetics of several redox reactions. Moreover, Fe-Fe interactions were taken from potential developments on bulk BCC and FCC iron metals. In an extension of this potential, included Rahaman included Cl parameters that were trained against energies derived for chloride/water clusters were added to the potential (FeOCHCl) [25]. However, in both cases there was again no parameterization of testing with elastic properties as the initial purpose was to reproduce iron-oxyhydroxide systems [24].

### Importance of Investigating Parameterization Testing Procedure

Overall, when selecting a potential it is imperative to consider the specific parameterizations and testing conducted during potential development. While some potentials have been developed specifically with elastic constants for iron, others are not even intended to be used for pure iron. Therefore, it is not sufficient to simply select a potential because it includes the element in question. Moreover, error was shown to depend more on the potential specific parameterizations and less on the general type of potential used. Further, it is clear that parameterization and testing with single crystal elastic constants indicates a suitability for predicting the elastic modulus from uniaxial tension tests.

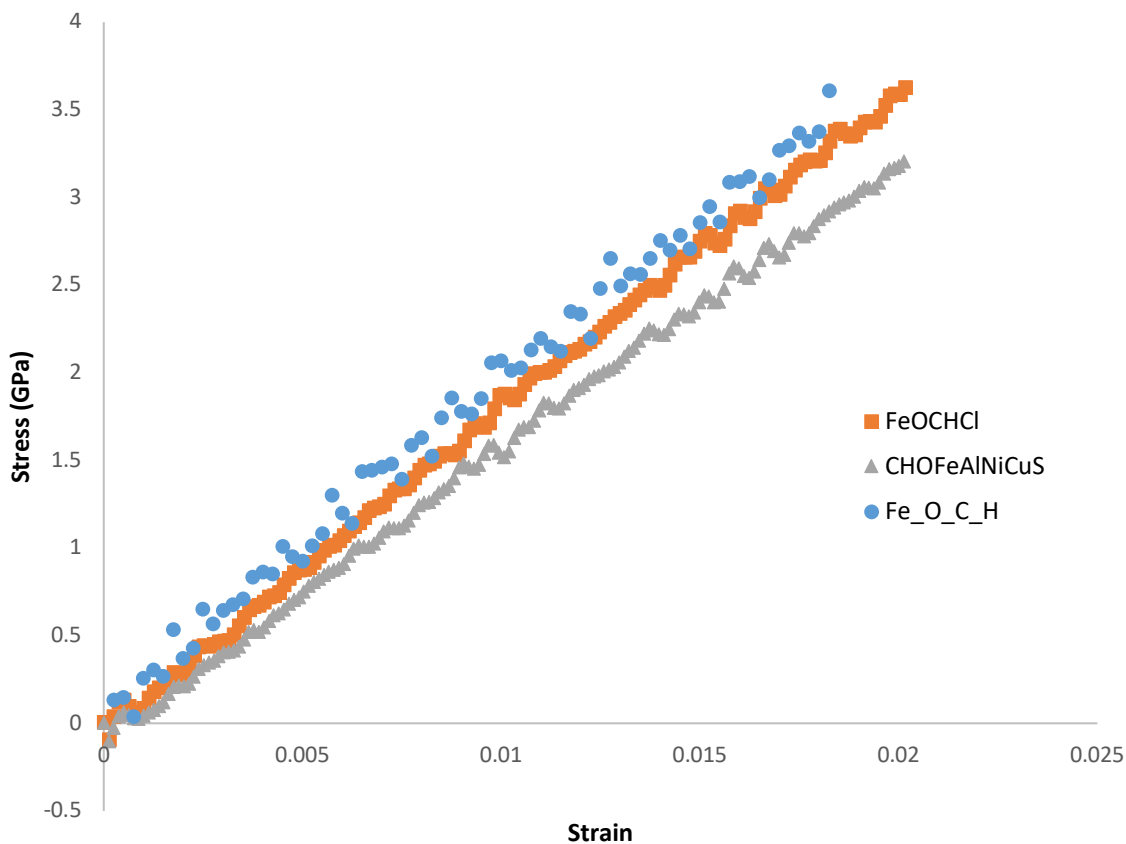


Figure 4.5 - Stress strain curves for ReaxFF potentials

## Conclusion

Molecular dynamics offers an exciting and more efficient opportunity to obtain macro-scale properties from atomistic simulations. Moreover, these simulations can be used to determine the effects of atomistic defects on mechanical properties. However, when attempting to model a structure there are several potentials available. In the current study EAM, MEAM, Tersoff, and ReaxFF many-body iron potentials were tested for their ability to replicate the tension tests typically used to obtain mechanical properties. Findings demonstrated that the error in predicted elastic modulus varied significantly depending on the potential considered. However, those potentials parameterized with

elastic constants were significantly more accurate at predicted the elastic modulus at room temperature. In summary, the current study highlights the clear need to understand the capabilities and limitations of each potential before application to a problem outside of the initial intended use.

## References

- [1] Byggmästar, J., Granberg, F., Kuronen, A., Nordlund, K., and Henriksson, K. O. E., 2015, "Tensile Testing of Fe and FeCr Nanowires Using Molecular Dynamics Simulations," *J. Appl. Phys.*, **117**(1), p. 14313.
- [2] Gao, X., Wang, T., and Kim, J., 2005, "On Ductile Fracture Initiation Toughness: Effects of Void Volume Fraction, Void Shape and Void Distribution," *Int. J. Solids Struct.*, **42**(18–19), pp. 5097–5117.
- [3] Komanduri, R., Chandrasekaran, N., and Raff, L. M., 2001, "Molecular Dynamics (MD) Simulation of Uniaxial Tension of Some Single-Crystal Cubic Metals at Nanolevel," *Int. J. Mech. Sci.*, **43**(10), pp. 2237–2260.
- [4] Rajabpour, A., Seidabadi, L., and Soltanpour, M., 2015, "Calculating the Bulk Modulus of Iron and Steel Using Equilibrium Molecular Dynamics Simulation," *Procedia Mater. Sci.*, **11**, pp. 391–396.
- [5] Chamati, H., Papanicolaou, N. I., Mishin, Y., and Papaconstantopoulos, D. A., 2006, "Embedded-Atom Potential for Fe and Its Application to Self-Diffusion on Fe (1 0 0)," *Surf. Sci.*, **600**(9), pp. 1793–1803.
- [6] Mendeleev, M. I., Han, S., Srolovitz, D. J., Ackland, G. J., Sun, D. Y., and Asta, M., 2003, "Development of New Interatomic Potentials Appropriate for Crystalline and Liquid Iron," *Philos. Mag.*, **83**(35), pp. 3977–3994.
- [7] Plimpton, S. J., and Thompson, A. P., 2012, "Computational Aspects of Many-Body Potentials," *MRS Bull.*, **37**(5), pp. 513–521.
- [8] Daw, M. S., and Baskes, M. I., 1984, "Embedded-Atom Method: Derivation and Application to Impurities, Surfaces, and Other Defects in Metals," *Phys. Rev. B*, **29**(12), p. 6443.
- [9] Lee, B.-J., Baskes, M. I., Kim, H., and Cho, Y. K., 2001, "Second Nearest-Neighbor Modified Embedded Atom Method Potentials for Bcc Transition Metals," *Phys. Rev. B*, **64**(18), p. 184102.
- [10] Tersoff, J., 1988, "New Empirical Approach for the Structure and Energy of Covalent Systems," *Phys. Rev. B*, **37**(12), p. 6991.
- [11] Van Duin, A. C. T., Dasgupta, S., Lorant, F., and Goddard, W. A., 2001, "ReaxFF: A Reactive Force Field for Hydrocarbons," *J. Phys. Chem. A*, **105**(41), pp. 9396–9409.
- [12] Plimpton, S. J., 2018, "Large-Scale Atomistic/Molecular Massively Parallel Simulation (LAMMPS)."
- [13] Plimpton, S. J., 1995, "Fast Parallel Algorithms for Short-Range Molecular Dynamics," *J. Comput. Phys.*, **117**(1), pp. 1–19.

- [14] van Duin, A., 2002, "ReaxFF User Manual," Calif. Inst. Technol. Mater. Process Simul. Cent.
- [15] Jensen, B. D., Wise, K. E., and Odegard, G. M., 2015, "The Effect of Time Step, Thermostat, and Strain Rate on ReaxFF Simulations of Mechanical Failure in Diamond, Graphene, and Carbon Nanotube," *J. Comput. Chem.*, **36**(21), pp. 1587–1596.
- [16] Becker, C. A., Tavazza, F., Trautt, Z. T., and de Macedo, R. A. B., 2013, "Considerations for Choosing and Using Force Fields and Interatomic Potentials in Materials Science and Engineering," *Curr. Opin. Solid State Mater. Sci.*, **17**(6), pp. 277–283.
- [17] Simmons, G., 1965, *Single Crystal Elastic Constants and Calculated Aggregate Properties*, Southern Methodist Univ Dallas Tex.
- [18] Proville, L., Rodney, D., and Marinica, M.-C., 2012, "Quantum Effect on Thermally Activated Glide of Dislocations," *Nat. Mater.*, **11**(10), pp. 845–849.
- [19] Asadi, E., Zaeem, M. A., Nouranian, S., and Baskes, M. I., 2015, "Quantitative Modeling of the Equilibration of Two-Phase Solid-Liquid Fe by Atomistic Simulations on Diffusive Time Scales," *Phys. Rev. B*, **91**(2), p. 24105.
- [20] Etesami, S. A., and Asadi, E., 2018, "Molecular Dynamics for near Melting Temperatures Simulations of Metals Using Modified Embedded-Atom Method," *J. Phys. Chem. Solids*, **112**, pp. 61–72.
- [21] Henriksson, K. O. E., Björkas, C., and Nordlund, K., 2013, "Atomistic Simulations of Stainless Steels: A Many-Body Potential for the Fe–Cr–C System," *J. Phys. Condens. Matter*, **25**(44), p. 445401.
- [22] Rahaman, O., van Duin, A. C. T., Goddard III, W. A., and Doren, D. J., 2011, "Development of a ReaxFF Reactive Force Field for Glycine and Application to Solvent Effect and Tautomerization," *J. Phys. Chem. B*, **115**(2), pp. 249–261.
- [23] Shin, Y. K., Kwak, H., Zou, C., Vasenkov, A. V., and van Duin, A. C. T., 2012, "Development and Validation of a ReaxFF Reactive Force Field for Fe/Al/Ni Alloys: Molecular Dynamics Study of Elastic Constants, Diffusion, and Segregation," *J. Phys. Chem. A*, **116**(49), pp. 12163–12174.
- [24] Aryanpour, M., van Duin, A. C. T., and Kubicki, J. D., 2010, "Development of a Reactive Force Field for Iron–Oxyhydroxide Systems," *J. Phys. Chem. A*, **114**(21), pp. 6298–6307.
- [25] Rahaman, O., Van Duin, A. C. T., Bryantsev, V. S., Mueller, J. E., Solares, S. D., Goddard III, W. A., and Doren, D. J., 2010, "Development of a ReaxFF Reactive Force Field for Aqueous Chloride and Copper Chloride," *J. Phys. Chem. A*, **114**(10), pp. 3556–3568.

## Chapter 5: Considerations when assessing the applicability of interatomic force fields for predicting mechanical properties of single crystals and bulk polycrystals

### **Authors:**

**Liam S. Morrissey\***, **Sam Nakhla**

### **CRediT author statement:**

**Liam S. Morrissey:** conceptualization, methodology, software, formal analysis, investigation, writing – original draft, **Sam Nakhla:** validation, resources, writing – review and editing, supervision

## Abstract

The choice of a proper interatomic potential is critical to obtaining accurate and realistic molecular dynamics results. However, previous studies that have tested the suitability of a potential to predict mechanical properties often do so using elastic constants from a triaxial stress state that ignores Poisson's effect. While this method is suitable it is not consistent with macroscale experimental methods and cannot provide the complete loading behavior. Further, there is a lack of knowledge as to whether accuracy in predicting elastic constants from a fixed volume condition indicates accuracy for elastic moduli from uniaxial tensile simulations. Moreover, those studies that did account for Poisson's effect studied only one crystal orientation and thus assumed potential accuracy is independent of crystal orientation. Results from the current study demonstrated that accuracy of a potential is dependent on the crystal direction. Further, the most accurate potentials for elastic constants calculated using a fixed volume condition were not necessarily the most accurate at predicting elastic moduli from a physically realizable tension test. Finally, the Voigt Reuss Hill (VRH) method was shown to accurately predict polycrystalline mechanical properties from single crystal data as a function of temperature.

## Introduction

Obtaining an accurate elastic modulus is a critical first step to any material characterization procedure. On the macroscale the elastic modulus is typically determined using a standardized uniaxial laboratory tension test. The specimen is strained within the elastic region and the modulus is determined from the slope of the resulting stress-strain curve. While these macroscale tests are relatively simple to conduct, they are unable to directly provide information on the microstructure during straining. Therefore, it is difficult to track the atomistic processes that often precipitate macroscale events such as yielding, necking, and failure. As an alternative, molecular dynamics (MD) is now being used to model materials on the atomistic scale and obtain mechanical properties. In contrast to macroscale testing, MD simulations allow for the observations of the microstructure during straining. These atomistic tests can be used to better understand mechanical properties, dislocation interactions, and the effect of defects/impurities during loading in both the elastic and plastic regions. However, there are multiple simulation methods that can be used to obtain mechanical properties.

### Obtaining Mechanical Properties in MD Simulations

The first, and most commonly used, method of obtaining mechanical properties in MD simulations is a fixed lateral strain method. In this method, periodic structures are deformed using a constant number, volume and temperature (*NVT*) thermostat that fixes lateral strains to zero. The stresses are then calculated at each step using the virial atomic stress tensor, which has been shown to be equivalent to the continuum Cauchy stress [1] as per equation 1:

$$S_{ab} = - \sum_i m_i v_i^a v_i^b + \frac{1}{2} \sum_i \sum_{j \neq i} F_{ij}^a r_{ij}^b \quad (1)$$

Where  $m_i$  and  $v_i$  are the mass and velocity of the atom  $i$ ,  $F_{ij}$  is the force between atoms  $i$  and  $j$ ,  $r_{ij}$  is the distance between atoms  $i$  and  $j$ , and the indices  $a$  and  $b$  denote the Cartesian components.

However, by fixing the lateral strains to zero Poisson's effect is ignored and lateral stresses develop as a result of the *NVT* thermostat, creating a triaxial stress state. As a result, the slope of the stress strain curve is no longer equivalent to the elastic modulus and instead represents the elastic stiffness constant  $C_{11}$ . Therefore, as opposed to the elastic moduli in various orientations, elastic stiffness constants are calculated from the triaxial stress state. These elastic constants can then be used in combination to obtain the elastic moduli in various orientations. While this test is certainly a viable option to calculate elastic constants, its comparability to physical tension tests is questionable. By ignoring Poisson's effect the test is no longer a uniaxial tension test. This becomes particularly troubling when findings are then compared to physically realizable macroscale experimental results where a uniaxial stress state is preserved and lateral axes are sure to contract. Comparison to experimental data is a critical, and sometimes overlooked, aspect of MD studies. However, for this comparison to be legitimate and accurate it is important to maintain a consistent method across the dimensional scales. In addition, while the method can predict elastic constants, it cannot extend these findings beyond the elastic region where dislocation interactions, yielding and plasticity are all found. One of the most exciting aspects of MD studies is their ability to simulate the effects of various defects on subsequent loading and failure behavior. Therefore limiting simulations to only the elastic region does not allow for a complete investigation of the loading behavior.

As an alternative, the elastic moduli can also be calculated directly using a constant number, pressure and temperature (*NPT*) barostat. Atomistic scale tension tests, originally proposed by Brown

and Clarke [2], deform a small cube of the material and produce a stress strain curve. Through controlling the lateral dimensions to zero pressure the uniaxial stress state is preserved and the simulation is able to capture the natural Poisson contractions that are required for any physically realizable study. Further, the slope of the stress strain curve now represents the orientation specific elastic modulus that would be obtained from macroscale experimental testing. This method is therefore both physically realizable and allows for the simulation of identical methods across multiple scales. Further, as opposed to simply calculating elastic constants, being able to accurately simulate an atomistic uniaxial tension test allows for a complete description of the materials behaviour during loading. This method has been used by several previous studies to predict the elastic modulus of both metals [3-5] and polymers [2]. In addition, the method can be used to predict the influence of various impurities on the yielding and failure behavior. For example, Yu et al. investigated the effect of atomic hydrogen on the dislocation generation and subsequent yielding of Tungsten samples under uniaxial tension [6]. Similarly, Morrissey et al. [7] used a uniaxial tension test to investigate failure and microstructure changes of gold nanowires during elastic/plastic loading.

### The Importance of Potential Type

During an MD simulation the interatomic potential is used to define forces between interacting particles, thus allowing for the calculation of the atomic acceleration and subsequent positions and velocities of atoms in the system [8]. Therefore, this potential is critical to obtaining accurate simulation results in a uniaxial tension test. There are several types of many-body potentials including the embedded atom method (EAM) and modified embedded atom method (MEAM). Further, within each potential there are several subsets that have been parameterized for different purposes against different parameter sets. Parameterization involves fitting the potential against a database that can include both density functional theory (DFT) data and experimental results. Therefore, potentials must

be assessed prior to application for purposes outside of their intended use. In response to this need significant previous research has compared several available potentials for their accuracy in predicting mechanical properties [3, 5, 9, 10]. These papers demonstrate which potentials can confidently be used for mechanical properties and are intended to assist future researchers in selecting potentials. However, upon closer inspection there are several critical assumptions being made that may be limiting the applicability of the findings.

The most common method used to assess a potentials ability to predict mechanical properties is a fixed volume tension test to obtain elastic constants. These constants can then be compared to literature data to determine suitability. For example, Rassoulinejad-Mousavi et al. compared predicted elastic constants for several different EAM type potentials for FCC metals [9, 10]. In this study, periodic cubes were deformed using a constant number, volume and temperature (*NVT*) thermostat that fixed lateral strains to zero. As discussed above, by fixing the lateral strains to zero Poisson's effect is ignored and the simulations are therefore no longer uniaxial or physically realizable. Despite this, findings were still compared against experimental elastic constants obtained from uniaxial tension tests, where, regardless of the scale, Poisson's effect is sure to be observed. Therefore these results are not keeping the testing method consistent as compared to experimental methods and assume that the method used to obtain the elastic constants does not affect the accuracy of the potential. In other words, *will the most accurate potentials for elastic constants from a zero lateral strain condition also be the most accurate in obtaining mechanical properties from a uniaxial tension simulation?* Previous simulations on silica has suggested that the temperature ensemble may influence results. For example, Yuan et al. [11] compared the complete stress strain curve of amorphous silica under uniaxial deformation with an *NVT* and *NPT* ensemble. Findings indicated the triaxial stress state caused by the *NVT* thermostat resulted in a less accurate behaviour in both the elastic and plastic regions.

Limited research has been conducted on the accuracy of various potentials for simulating uniaxial tension tests using the *NPT* ensemble. For example, Morrissey et al. [5] and Komanduri et al. [3] tested the accuracy of various potentials for BCC and FCC metals. These studies concluded that the potential type used could significantly affect the relative accuracy and that care must be used to ensure the potential was parameterized for the intended purpose of the study. However, no study has tested whether accuracy from one method of straining is suitable to conclude suitability for others.

### Single Crystals and Polycrystals

Given the atomistic scale at which straining is taking place, it is important to also consider the single crystal nature of these uniaxial tension tests. On the macroscale metals are polycrystalline with several single crystals oriented in various random directions to form a polycrystal. The elastic modulus of these polycrystalline metals are essentially isotropic [12]. Therefore, the modulus obtained from a macroscale tension test is actually the polycrystalline elastic modulus. This becomes an important distinction when moving the discussion to atomistic scale tension tests. Due to size limitations imposed by computational requirements, atomistic scale tension tests are typically conducted on single crystals with prescribed orientations and strain directions. Individual crystals for most metals are no longer isotropic and their elastic modulus therefore depends on the orientation of the crystal. Moreover, because many properties are dependent on crystal orientation, multiple orientations should be considered when simulating single crystals. For example, in single crystal iron the elastic modulus in the [111] orientation is almost two times higher than the [100] orientation [13].

While elastic constants from fixed volume *NVT* simulations can be used to predict a modulus in any orientation, uniaxial *NPT* tension tests predict an orientation specific single crystal modulus. However, previous studies that have tested the relative accuracy of potentials using an *NPT* barostat are

often limited to only one orientation in their assessment [3, 5]. These studies are making the assumption that modulus accuracy in one crystal orientation indicates accuracy in other orientations. However, as has been shown both on the macroscale and using MD, many processes and properties are highly dependent on crystal orientation. As such, there is a gap in knowledge on the accuracy of various potential types when multiple orientations beyond the commonly reported [100] are considered. Simply put, *does a potential being accurate in the [100] orientation indicate accuracy for the elastic modulus in other crystal orientations?*

When commenting on the accuracy of a single crystal simulation it is imperative to compare to relevant anisotropic experimental data. However, depending on the specific orientation, material and temperature being simulated single crystal data may not be readily available. As opposed to single crystal simulations, MD polycrystals can be generated using a Voronoi tessellation to produce several randomly oriented grains separated by grain boundaries. Due to the scale of these simulations, results are extremely dependent on both the average grain size and number of grains in the periodic simulation cell [14, 15]. Moreover, because the simulation box must be large enough to obtain a reasonable representative sample these simulations can become computationally intensive. As an alternative, the Voigt-Reuss-Hill (VRH) approximation can be used to determine the elastic modulus of an untextured polycrystalline bulk from single crystal properties [16, 17]. In this method two critical assumptions are made. First, the local strain is assumed to be equivalent to the mean strain, thus all grains undergo the same strain. This assumption, known as the Voigt average, calculates the Young's modulus via equation 2 using the elastic stiffness constants  $C_{ij}$ :

$$E_v = \frac{(A - B + 3C)(A + 2B)}{(2A + 3B + C)} \quad (2)$$

where:

$$A = \frac{C_{11} + C_{22} + C_{33}}{3}$$

$$B = \frac{C_{23} + C_{13} + C_{12}}{3}$$

$$C = \frac{C_{44} + C_{55} + C_{66}}{3}$$

Second, the local stress is assumed to be equivalent to the mean stress, thus all grains undergo the same stress. This assumption, known as the Reuss average, calculates a lower bound of the Young's modulus via equation 3 using the elastic compliance constants  $S_{ij}$ :

$$E_r = \frac{5}{(3A' + 2B' + C')} \quad (3)$$

where:

$$A' = \frac{S_{11} + S_{22} + S_{33}}{3}$$

$$B' = \frac{S_{23} + S_{13} + S_{12}}{3}$$

$$C' = \frac{S_{44} + S_{55} + S_{66}}{3}$$

Finally, an estimated polycrystalline elastic modulus can then be determined by taking as average of the Voigt and Reuss moduli. However, no study has tested the accuracy of using multiple atomistic uniaxial single crystal simulations combined with the VRH theory to predict the elastic modulus of a polycrystal. Recently, Rassoulinejad-Mousavi et al. [9] used the VRH approximation to estimate the bulk elastic modulus of FCC metals using MD. As discussed above, elastic constants were calculated by forcing lateral strains to zero. Therefore, the VRH approximation was not tested with values obtained from physically realizable uniaxial simulations.

### Purpose

There are several important gaps in knowledge when assessing the accuracy of potentials at predicting mechanical properties. First, previous studies that have compared the accuracy of potentials focused on elastic constants and did not actually simulate physically realizable uniaxial tension tests seen on the macroscale. While this method is viable it is not consistent with macroscale testing methods and cannot be used to obtain the full stress strain curve. Moreover, these studies are assuming that the accuracy of a potential to predict elastic modulus does not depend on the simulation method used to obtain the mechanical properties. However, if this assumption were incorrect than significant error may be being introduced to simulations simply due to poor potential evaluation. Second, those studies that did account for Poisson's effect studied only one crystal orientation and thus assumed potential accuracy is independent of crystal orientation. However there is a lack of research on whether the potential accuracy is dependant on crystal orientation. Finally, the accuracy of using the VRH approximation to calculate the MD bulk elastic modulus has been tested for FCC metals only and was conducted using only one temperature and an *NVT* ensemble. Therefore, the purpose of this study was to test methods used to assess potentials to determine whether crystal orientation and tensile testing method can affect the relative accuracy for single crystal and bulk polycrystal mechanical properties.

## Methodology

Prior to testing for elastic modulus cubes of BCC iron and FCC aluminum were developed. Aluminum and iron were chosen as they are two of the most commonly used metals, have different crystal structures, and possess significantly different elastic moduli. A 10 x 10 x 10 Å lattice unit cube of metal was generated with periodic boundary conditions in the x, y and, z directions (Figure 5.1). Simulation geometry and size were chosen to represent the gage section typically found in a laboratory tension test as per Komanduri [3]. Next, the cube was then equilibrated to the prescribed temperature using a constant number, pressure, and temperature (*NPT*) Nose-Hoover barostat that allowed the volume to expand to the given temperature. Temperatures of 100K, 300K, and 600K (representing low temperature, room temperature, and high temperature) were tested. For each simulation two EAM potentials and one MEAM potential were tested as per Table 5.1. For all simulations a timestep of 1 femtosecond was used. After preparing the cube and equilibrating to the given temperature it was then ready for tensile testing.

Table 5.1 - Summary of potentials tested for BCC Iron and FCC Aluminum

<b>Material</b>	<b>Potential Type</b>	<b>Name</b>	<b>Reference</b>
BCC Iron	EAM	Fe_Mishin2006.eam.alloy	Chamati 2006 [18]
	EAM	Fe_mm.eam.fs	Mendelev 2003 [19]
	MEAM	Fe.meam	Etesami 2018 [20]
FCC Aluminum	EAM	Al99.eam.alloy	Mishin 1999 [21]
	EAM	Al1.eam.fs	Mendelev 2008 [22]
	MEAM	Al.meam	Pascuet 2015 [23]

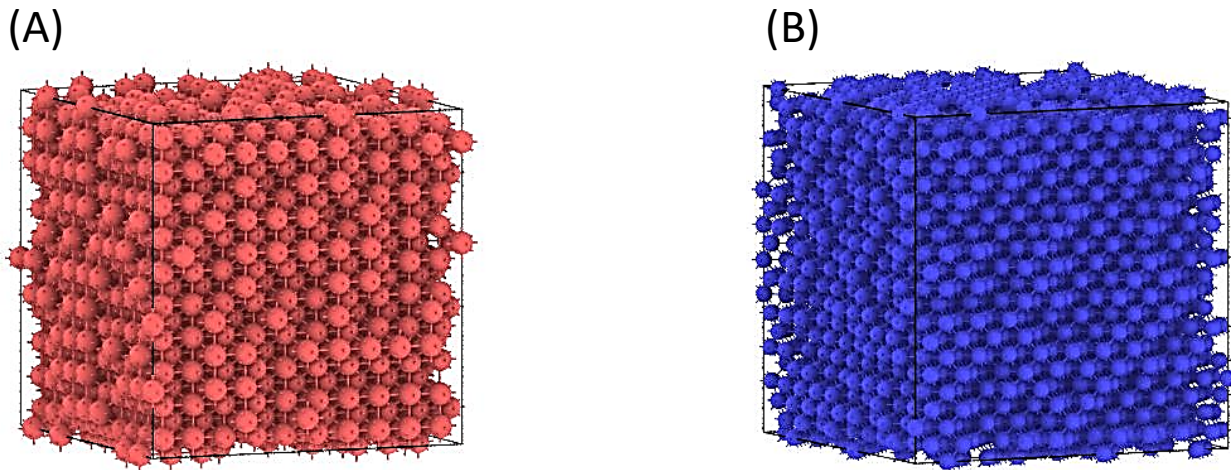


Figure 5.1 - Initial structure of BCC iron (A) and FCC aluminum (B) prior to straining\*.

\*Artificial bonds are added in post-processing to increase clarity of figure

#### Atomistic Uniaxial Tension Test

As introduced above, the atomistic tension test involves deforming a cube at a prescribed strain rate to a total final strain. Each structure was deformed in the x-direction at the prescribed temperature with lateral boundaries controlled to zero pressure via an *NPT* barostat to allow for natural Poisson contractions. A strain rate of 0.01 per picosecond was used. It is important to note that this value is many orders of magnitude above experimental strain rate. However, the value is well within the range tested by Jensen et al. who demonstrated that the mechanical response was independent of MD strain rate in the elastic region [24]. To ensure comparable studies, strain rates were kept consistent for all potentials tested. In total, each sample was strained to 2%, within the linear range where Hooke's law is applicable. The resulting slope of the stress-strain curve in the linear region was then used to produce an elastic modulus for the given metal tested. Due to the anisotropic nature of single crystal metals, each test was conducted three times with strain applied along the [100], [110] and [111] directions of

the crystal lattice. The elastic modulus for each orientation was then compared to their single crystal macroscale counterparts obtained from laboratory tension tests at specific temperatures [25].

### Polycrystalline Elastic Modulus

After obtaining the single crystal moduli at each orientation these values were then converted to a polycrystalline elastic modulus using the VRH approximation. First, the elastic modulus in the [100], [110] and [111] directions were used to calculate the elastic compliance constants ( $S_{11}, S_{12}, S_{44}$ ) as per equations 4-6:

$$S_{11} = \frac{1}{E_{100}} \quad (4)$$

$$S_{12} = \frac{2}{E_{110}} - \frac{1}{E_{100}} - \frac{1}{2 * G_{100}} \quad (5)$$

$$S_{44} = \frac{1}{G_{100}} \quad (6)$$

Where  $E_{100}$ ,  $E_{110}$ , and  $E_{111}$  are elastic moduli in the [100], [110] and [111] directions and  $G_{100}$  is the shear modulus in the [100] direction

Therefore, as opposed to Rassoulinejad-Mousavi et al. [9, 10], compliance constants were calculated using contributions from the elastic moduli of multiple different crystal orientations. Moreover, lateral axes were allowed to contract to maintain zero pressure, allowing for an accurate comparison to experimental results.

As can be seen in the above equations, a shear modulus is needed to determine the  $S_{44}$  value. Therefore, similar to the uniaxial tension test a simple shear test was conducted using MD at each temperature. As before, a 10 x 10 x10 lattice unit cube was first equilibrated to the prescribed temperature. The box was then deformed in the x-y direction and the slope of the resulting shear stress versus shear strain curve was used to determine a shear modulus (G) in the [100] direction.

Next, the elastic stiffness constants ( $C_{11}, C_{12}, C_{44}$ ) were calculated from the compliance constants as per equations 7-9:

$$C_{11} = \frac{S_{11} + S_{12}}{(S_{11} - S_{12})(S_{11} + 2S_{12})} \quad (7)$$

$$C_{12} = \frac{-S_{12}}{(S_{11} - S_{12})(S_{11} + 2S_{12})} \quad (8)$$

$$C_{44} = \frac{1}{S_{44}} \quad (9)$$

After obtaining the compliance and stiffness constants the polycrystalline elastic modulus was approximated by taking an average of equations 2 and 3. Similarly, the VRH approximation can also be used to determine a polycrystalline shear modulus as per equations 10-12:

$$G_V = \frac{5C_{44}(C_{11} - C_{12})}{4C_{44} + 3(C_{11} - C_{12})} \quad (10)$$

$$G_R = \frac{C_{11} - C_{12} + 3C_{44}}{5} \quad (11)$$

$$G_{VRH} = \frac{G_V + G_R}{2} \quad (12)$$

## Fixed Lateral Axis Tension Test

In addition to a uniaxial tension test with an *NPT* barostat, cubes were also deformed using a fixed volume test that uses an *NVT* Nose-Hoover thermostat. As before, a strain rate of 0.01 per picosecond was used and values were sampled up to 2% strain. Following previous similar studies [9, 10, 26], the constants  $C_{11}$  and  $C_{12}$  were calculated via equations 13:

$$\sigma_{xx} = C_{11} e_{xx} + C_{12}(e_{yy} + e_{zz}) \quad (13)$$

Where is  $\sigma_{xx}$  the stress in the xx direction, and  $e_{xx}$ ,  $e_{yy}$ ,  $e_{zz}$  are the strains in the x, y, and z directions respectively. Because lateral strains are zero this simply reduces to equation 14:

$$\sigma_{xx} = C_{11} e_{xx} \quad (14)$$

The resulting triaxial stress state then allows for calculation of the  $C_{12}$  elastic constant as per equation 15:

$$\sigma_{yy} + \sigma_{zz} = 2C_{12} e_{xx} \quad (15)$$

Next, to obtain the  $C_{44}$  elastic constant a prism region was created to define a triclinic simulation box with zero initial tilt. Then, using the same strain rate the system was deformed in the [100] direction and  $C_{44}$  was calculated as per equation 16:

$$\sigma_{xy} = C_{44} \gamma_{xy} \quad (17)$$

Where  $\sigma_{xy}$  is the stress in the xy direction and  $\gamma_{xy}$  is the engineering shear strain.

Finally, to allow for comparison with the *NPT* uniaxial tension test the stiffness constants were converted to elastic moduli ( $E_{ijk}$ ) in the [100], [110] and [111] directions as per equation 18 [16]:

$$\frac{1}{E_{ijk}} = S_{11} - 2 \left( S_{11} - S_{12} - \frac{S_{44}}{2} \right) (l_{i1}^2 l_{j2}^2 + l_{j2}^2 l_{k3}^2 + l_{i1}^2 l_{k3}^2) \quad (18)$$

Where ( $l_{ij}$ ) are the directional cosines for each orientation considered

## Results

### Effect of Crystal Orientation

The first consideration in this study was the effect of crystal orientation in the direction of straining on the accuracy of predicted elastic modulus. As previously discussed, on the macroscale metals are considered isotropic due to their polycrystalline nature. However, when using molecular dynamics to simulate on the atomistic scale it becomes difficult to accurately capture the significant grain boundaries and random orientations found in metals. As such, MD simulations typically model metals as single crystals, which are no longer isotropic and hence have mechanical properties that are dependent on lattice orientation in the strain direction. Referring to the experimental data for single crystals in Table 5.2, it can be seen that both single crystal BCC iron and FCC aluminum are anisotropic. In both cases the highest elastic modulus is found in the [111] direction. Due to this anisotropy, molecular dynamics studies on metals often first orient the crystal along a specific strain direction and then compare against experimental data for this direction. However, these studies typically consider only one direction and thus make the assumption that accuracy for potential in a specific direction ensures accuracy for others [3-5]. To verify this assumption tests were conducted at three directions and compared to single crystal experimental results. Accuracy was determined based on the error as

compared to previously determined experimental values for single crystal iron and aluminum as provided in the handbook by Simmons and Wang [13].

Table 5.2 - Experimental elastic moduli for single crystal BCC iron and FCC aluminum as a function of temperature and crystal orientation [13]

Temperature	Experimental Elastic Modulus (GPa)					
	BCC Iron			FCC Aluminum		
	[100]	[110]	[111]	[100]	[110]	[111]
100K	141.4	231.6	294.4	69.9	79	82.5
300K	133.7	222.8	286.5	63.7	72.1	75.4
600K	110.6	197.6	267.7	50.9	60.1	63.9

Referring to Table 5.3, accuracy with experimental results is not consistent amongst the different directions during a molecular dynamics tension test. Total average error was calculated using the absolute value of errors at each direction. For example, while the Chamati 2006 EAM potential had an average error under 10% for all three temperatures of [100] iron, the error is much higher in the [111] direction (Table 5.3A). At 100K the [100] direction had an error of- 6%, however in the [111] direction was three times higher. Similarly, for the Mendeleev 2003 EAM potential the error was only 4% in the [100] direction at 300K and increased to 14% and 29% in the [110] and [111] directions respectively. Overall, the Chamati 2006 EAM potential had the lowest average error for all temperatures considered while the Mendeleev 2003 EAM potential had the highest average error. The discrepancy in error amongst crystal directions is also observed for FCC aluminum at the various temperatures (Table 5.3B). For example, at 300K the Mendeleev 2008 EAM potential had an average total error of 14%. However, in the [110] direction this error was only 3% as compared to -20% at [100]. For FCC aluminum the 1999 Mishin EAM potential had the lowest average error for all orientations and temperatures considered while the Mendeleev 2008 EAM potential had the highest average error.

Overall, it is clear that when assessing a potential's accuracy in predicting mechanical properties it is imperative to consider the effect of crystal orientation in the strain direction. Therefore, those studies that have previously attempted to evaluate a potential by testing only one orientation may not be providing the complete picture. Moreover, accuracy in a specific direction does not guarantee accuracy in another. Further, if these potentials were used in a polycrystalline simulation large errors are possible due to poor modulus prediction in a certain orientation.

Table 5.3 - Predicted elastic modulus for single crystal BCC iron (A) and FCC aluminum (B) from a uniaxial tension test with an *NPT* ensemble. Error is calculated relative to single crystal experimental values.

\* Total average error is the mean of the magnitudes of errors in the [100], [110] and [111] orientations

A) BCC Iron			Elastic Modulus (GPa) for Various Orientations						Total Average Error
Temperature	Potential Type	Reference	[100]	Error	[110]	Error	[111]	Error	Error
100K	EAM	Chamati et al. 2006	132.5	-6%	225.7	-3%	241.4	-18%	9%
	EAM	Mendelev et al. 2003	144.7	2%	209.3	-10%	233.0	-21%	11%
	MEAM	Etesami et al. 2018	145.2	3%	244.5	6%	273.3	-7%	5%
300K	EAM	Chamati et al. 2006	131.3	-2%	222.9	0%	239.7	-16%	6%
	EAM	Mendelev et al. 2003	139.5	4%	191.5	-14%	203.7	-29%	16%
	MEAM	Etesami et al. 2018	116.7	-13%	222.7	0%	253.7	-11%	8%
600K	EAM	Chamati et al. 2006	124.1	12%	215.3	9%	234.8	-12%	11%
	EAM	Mendelev et al. 2003	124.7	13%	178.2	-10%	185.9	-31%	18%
	MEAM	Etesami et al. 2018	81.7	-26%	178.4	-10%	231.7	-13%	16%

B) FCC Aluminum			Elastic Modulus (GPa) for Various Orientations						Total Average Error*
Temperature	Potential Type	Reference	[100]	Error	[110]	Error	[111]	Error	Error*
100K	EAM	Mishin et al. 1999	67.4	-4%	80.9	2%	76.2	-8%	5%
	EAM	Mendelev et al. 2008	51.9	-26%	76.1	-4%	83.1	1%	10%
	MEAM	Pascuet et al. 2015	65.0	-7%	73.4	-7%	84.4	2%	5%
300K	EAM	Mishin et al. 1999	64.5	1%	75.5	5%	72.9	-3%	3%
	EAM	Mendelev et al. 2008	50.9	-20%	74.4	3%	88.8	18%	14%
	MEAM	Pascuet et al. 2015	56.7	-11%	62.1	-14%	76.3	1%	9%
600K	EAM	Mishin et al. 1999	55.5	9%	61.3	2%	67.1	5%	5%
	EAM	Mendelev et al. 2008	41.2	-19%	61.4	2%	77.7	22%	14%
	MEAM	Pascuet et al. 2015	42.4	-17%	46.6	-22%	54.0	-15%	18%

## Importance of Potential Parameterization

As discussed in previous studies on the effect of potential type, the answer as to why one potential is more accurate than another likely lies in the parameterization of the potential.

Parameterization involves fitting the potential against a set of data that often includes experimental results. The resulting potential may then be tested against certain material properties such as surface energies, point defects, and elastic constants. Allowable errors to target values are then determined based on a weighting procedure that specifies the most important parameters for the potential.

Therefore, while some potentials have not been trained or tested against bulk elastic properties, others have specifically been trained and tested against data sets for mechanical properties at room temperature.

First, for BCC iron the Chamati 2006 EAM potential was developed by fitting to both experimental and first principles results [18]. The potential was shown to accurately reproduce lattice constants, surface energies and vacancy/defect energies. While no mention was made of uniaxial tension tests, the potential was also shown to be able to accurately reproduce thermal expansion coefficients at room temperatures. Therefore, this potential was most accurate at modelling the realizable uniaxial tension tests considered in the present study. In contrast, the Mendeleev 2003 EAM potential was tested at 0K and was not parameterized or tested with realizable temperatures [19]. As such, this potential was less accurate than the Chamati 2006 potential at reproducing elastic properties at the various temperatures considered. Finally, the Etesami 2018 MEAM potential was developed by considering both low temperature (0K) and high temperature (>1600K) elastic constants for iron [20]. Again, no mention was made of uniaxial tension tests and elastic constants were obtained using an

indirect atom fluctuation based methods. Therefore, the potential was not tested developed for the temperature range or tension method considered and was hence less accurate.

Next, for FCC aluminum the Mishin 1999 EAM potential was shown to accurately reproduce elastic constants, surface energies, stacking fault energies and vacancy/defect energies [21]. While constants were not tested at realizable temperatures, a high weight was given to elastic constants during the fitting/testing procedures. In contrast, while the Pascuet 2015 MEAM potential was also tested against elastic constants it was shown to be less accurate at predicting the  $C_{44}$  elastic constant [23]. However, no effort was made to reduce this error as the author's did not place a high weight on elastic constants. Therefore, this potential was also less accurate when obtaining mechanical properties from uniaxial tension tests. Similarly, the Mendeleev 2008 EAM potential was parameterized and tested against an exhaustive list of material properties [22]. While accuracy was high for the  $C_{12}$  and  $C_{44}$  constants, the potential was less accurate at predicting the  $C_{11}$  constant. Moreover, elastic constants were not tested at realizable temperatures or using a uniaxial tension method. Therefore this potential was also less accurate than the Mishin 1999 EAM potential.

#### Effect of Ensemble during Straining: fixed volume *NVT* and uniaxial *NPT*

As opposed to the *NPT* barostat, many MD studies on elastic properties utilize an *NVT* thermostat when straining the simulation cell. This fixed volume ensemble results in zero lateral contractions and allows for elastic constants to be obtained. However this method is not directly comparable to uniaxial methods used on the macroscale and cannot obtain the complete stress strain curve. Moreover, no study has tested whether accuracy calculating mechanical properties from a triaxial *NVT* method also indicates accuracy for a uniaxial *NPT* method. Therefore, the predicted elastic moduli from a fixed volume *NVT* condition were compared to the *NPT* equilibration uniaxial tension

results. Referring to Table 5.4, elastic moduli calculated from the *NVT* and *NPT* methods do not agree. For BCC iron the elastic moduli for the two methods were relatively similar in the [100] and [110] orientations. However, in the [111] direction the fixed volume *NVT* method predicts a more accurate elastic modulus for all potentials. In contrast, for FCC aluminum the uniaxial *NPT* method predicted a better elastic modulus in all orientations for all potentials. For example, while the Mishin 1999 EAM potential had at average error of only 3% when using the *NPT* method, this error five times when using the fixed volume *NVT* method. Because the two methods are simulating drastically different scenarios it is not surprising that they predict different results. The findings clearly demonstrate that studies that evaluate the accuracy of potentials using a triaxial fixed volume ensemble during straining cannot be used to comment on the accuracy of potentials to simulate mechanical properties from physically realizable uniaxial tension tests. For example, the Chamati 2006 potential has an error of only 1% for BCC iron in the [111] orientation when using the *NVT* ensemble. However, when this single crystal is strained using a physically realizable uniaxial tension test the error is -16%. Therefore, to comment on the accuracy of potential for simulating a uniaxial tension test an *NPT* ensemble must be used.

Table 5.4 - Predicted elastic modulus for single crystal BCC iron (A) and FCC aluminum (B) from a uniaxial tension test with an *NVT* ensemble. Error is calculated relative to single crystal experimental values

Material	Potential Type	Reference	Elastic Modulus (GPa) for Various Orientations					
			(100)	Error	(110)	Error	(111)	Error
BCC Iron	EAM	Chamati et al. 2006	134.0	0%	224.0	1%	288.8	1%
	EAM	Mendelev et al. 2003	140.9	5%	202.2	-9%	236.4	-17%
	MEAM	Etesami et al. 2018	112.6	-16%	205.7	-8%	283.9	-1%
FCC Aluminum	EAM	Mishin et al. 1999	62.1	-3%	83.8	16%	94.8	26%
	EAM	Mendelev et al. 2008	44.1	-31%	73.5	2%	94.5	25%
	MEAM	Pascuet et al. 2015	54.0	-15%	74.1	3%	84.5	12%

## Estimating Polycrystalline Mechanical Properties: The VRH Method

The final step in this study was to investigate the accuracy of using the elastic moduli from single crystal simulations to predict polycrystalline mechanical properties as a function of temperature. Equations 4-14 were used to convert the single crystal anisotropic elastic moduli into the elastic compliance constants ( $S_{11}, S_{12}, S_{44}$ ), elastic stiffness constants ( $C_{11}, C_{12}, C_{44}$ ), and then the polycrystalline elastic modulus and shear modulus. Referring to table 5.5 and Figure 5.2, for all potentials tested the polycrystalline elastic and shear moduli decreased with temperature, agreeing with experimental trends. For BCC iron the Chamati 2006 EAM potential best predicted bulk polycrystalline values with errors below 10% at all temperatures tested. This potential was also the most accurate for single crystal mechanical properties. In contrast, for FCC aluminum the Mendeleev 2008 EAM potential was the only potential with errors below 10% for bulk polycrystalline values at all temperatures tested. Therefore, while accuracy with single crystal mechanical properties is a strong indicator of accuracy with the VRH method, it does not guarantee which potential is most accurate. Instead, the method described in this paper should be used to definitively determine the most accurate potentials for predicting bulk polycrystalline mechanical properties. Overall, the VRH method was able to accurately predict polycrystalline elastic modulus and shear modulus.

Table 5.5 - Predicted polycrystalline elastic modulus and shear modulus for BCC iron (A) and FCC aluminum (B) from a uniaxial tension test with an *NPT* ensemble using the VRH method. Error is calculated relative to bulk polycrystalline experimental values.

A) BCC Iron			Polycrystalline Mechanical Properties			
Temperature	Potential Type	Reference	Elastic Modulus	Error	Shear Modulus	Error
100K	EAM	Chamati et al. 2006	215.8	-3%	81.3	-6%
	EAM	Mendelev et al. 2003	200.2	-10%	82.8	-4%
	MEAM	Etesami et al. 2018	233.4	5%	87.3	1%
300K	EAM	Chamati et al. 2006	213.2	0%	81.2	2%
	EAM	Mendelev et al. 2003	183.8	-14%	77.2	-7%
	MEAM	Etesami et al. 2018	214.6	1%	77.3	-7%
600K	EAM	Chamati et al. 2006	206.3	8%	78.5	7%
	EAM	Mendelev et al. 2003	170.3	-10%	67.5	-8%
	MEAM	Etesami et al. 2018	178.9	-6%	63.8	-13%

B) FCC Aluminum			Polycrystalline Mechanical Properties			
Temperature	Potential Type	Reference	Elastic Modulus	Error	Shear Modulus	Error
100K	EAM	Mishin et al. 1999	78.5	2%	29.9	4%
	EAM	Mendelev et al. 2008	72.6	-6%	27.7	-4%
	MEAM	Pascuet et al. 2015	71.9	-7%	37.2	29%
300K	EAM	Mishin et al. 1999	73.5	4%	30.0	15%
	EAM	Mendelev et al. 2008	71.1	1%	28.4	9%
	MEAM	Pascuet et al. 2015	61.1	-13%	31.2	20%
600K	EAM	Mishin et al. 1999	60.2	3%	26.5	23%
	EAM	Mendelev et al. 2008	58.7	0%	23.7	10%
	MEAM	Pascuet et al. 2015	45.8	-22%	22.4	4%

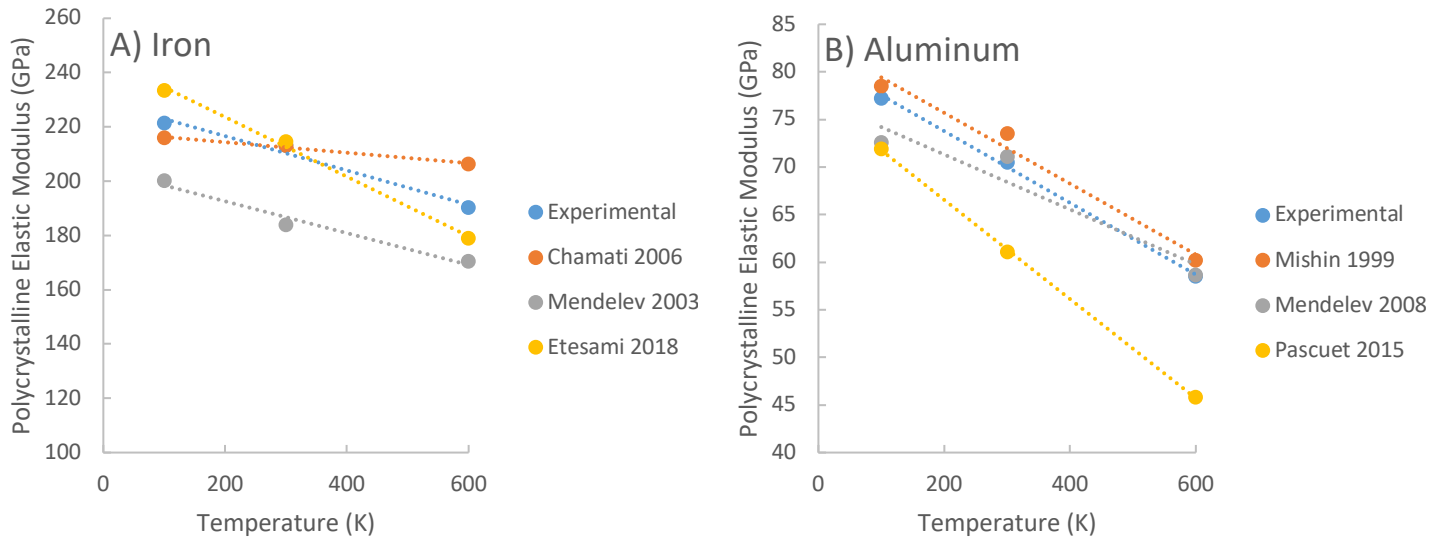


Figure 5.2 - Polycrystalline elastic modulus from using the VRH method as a function of temperature for iron and aluminum using various interatomic potentials

## Conclusion

Overall, MD offers an exciting opportunity to study the role defects and impurities can have on the mechanical properties of materials during loading. Using a suitable interatomic potential is critical to obtaining reasonable and accurate simulation results. While elastic constants can be easily calculated using a fixed volume *NVT* simulation, these tests are not directly comparable to the macroscale uniaxial tension tests and cannot provide a complete stress strain curve. Instead, an *NPT* ensemble can be also used to simulate a physically realizable tension test in which the slope of the stress strain represents the elastic modulus and the complete loading behavior can be simulated. However, previous studies that have tested potential types often do so using triaxial stress states that are non physically realizable and ignore Poisson's effect. These studies therefore assume that potential accuracy is independent of the simulation method used to obtain mechanical properties. This study investigated atomistic uniaxial

tension tests for their ability to predict the elastic modulus of various single crystal orientations and of bulk polycrystals using the VRH approximation. In Results from this study indicated several important conclusions:

- When evaluating a potential it is important to consider more than just the [100] direction. Accuracy from *NPT* uniaxial tension tests was shown to be dependent on the direction considered.
- The potential specific parameterizations were then investigated to explain the relative accuracy of each potential. Those potentials parameterized with elastic constants at the temperature range considered were shown to be most accurate.
- The most accurate potentials from an *NVT* triaxial test were not necessarily the most accurate for an *NPT* uniaxial test with Poisson's effect. Therefore, previous studies that have assessed potentials using elastic constants obtained from fixed volume scenarios are not applicable for realizable uniaxial tests. These potentials should instead be assessed using the exact method they will be compared to.
- The VRH method was shown to accurately predict polycrystalline bulk mechanical properties as a function of temperature. Therefore this study demonstrates the accuracy of the VRH method for metals from multiple single crystal uniaxial MD simulations

## References

- [1] Subramaniyan, A. K., and Sun, C. T., 2008, "Continuum Interpretation of Virial Stress in Molecular Simulations," *International Journal of Solids and Structures*, **45**(14) pp. 4340-4346.
- [2] Brown, D., and Clarke, J. H., 1991, "Molecular Dynamics Simulation of an Amorphous Polymer Under Tension. 1. Phenomenology," *Macromolecules*, **24**(8) pp. 2075-2082.
- [3] Komanduri, R., Chandrasekaran, N., and Raff, L. M., 2001, "Molecular Dynamics (MD) Simulation of Uniaxial Tension of some Single-Crystal Cubic Metals at Nanolevel," *International Journal of Mechanical Sciences*, **43**(10) pp. 2237-2260.
- [4] Byggmästar, J., Granberg, F., Kuronen, A., 2015, "Tensile Testing of Fe and FeCr Nanowires using Molecular Dynamics Simulations," *Journal of Applied Physics*, **117**(1) pp. 014313.
- [5] Morrissey, L. S., Handrigan, S. M., Subedi, S., 2019, "Atomistic Uniaxial Tension Tests: Investigating various Many-Body Potentials for their Ability to Produce Accurate Stress Strain Curves using Molecular Dynamics Simulations," *Molecular Simulation*, **45**(6) pp. 501-508.
- [6] Yu, X., Gou, F., and Tian, X., 2013, "Molecular Dynamics Study of the Effect of Hydrogen on the Mechanical Properties of Tungsten," *Journal of Nuclear Materials*, **441**(1-3) pp. 324-330.
- [7] Morrissey, L. S., Handrigan, S. M., and Nakhla, S., 2020, "Discrepancies in the Mechanical Properties of Gold Nanowires: The Importance of Potential Type and Equilibration Method," *Computational Materials Science*, **171**pp. 109234.
- [8] Plimpton, S. J., and Thompson, A. P., 2012, "Computational Aspects of Many-Body Potentials," *MRS Bulletin*, **37**(5) pp. 513-521.
- [9] Rassoulinejad-Mousavi, S. M., Mao, Y., and Zhang, Y., 2016, "Evaluation of Copper, Aluminum, and Nickel Interatomic Potentials on Predicting the Elastic Properties," *Journal of Applied Physics*, **119**(24) pp. 244304.
- [10] Rassoulinejad-Mousavi, S. M., and Zhang, Y., 2018, "Interatomic Potentials Transferability for Molecular Simulations: A Comparative Study for Platinum, Gold and Silver," *Scientific Reports*, **8**(1) pp. 1-10.
- [11] Yuan, F., and Huang, L., 2012, "Molecular Dynamics Simulation of Amorphous Silica Under Uniaxial Tension: From Bulk to Nanowire," *Journal of Non-Crystalline Solids*, **358**(24) pp. 3481-3487.
- [12] Chawla, N., and Deng, X., 2005, "Microstructure and Mechanical Behavior of Porous Sintered Steels," *Materials Science and Engineering: A*, **390**(1-2) pp. 98-112.
- [13] Simmons, G., 1965, "*Single crystal elastic constants and calculated aggregate properties*," Southern Methodist Univ Dallas Tex, .

- [14] Schiøtz, J., Vegge, T., Di Tolla, F., 1999, "Atomic-Scale Simulations of the Mechanical Deformation of Nanocrystalline Metals," *Physical Review B*, **60**(17) pp. 11971.
- [15] Xu, W., and Dávila, L. P., 2018, "Tensile Nanomechanics and the Hall-Petch Effect in Nanocrystalline Aluminium," *Materials Science and Engineering: A*, **710**pp. 413-418.
- [16] Meyers, M.A., and Chawla, K.K., 2008, "Mechanical behavior of materials," Cambridge university press, .
- [17] Den Toonder, J., Van Dommelen, J., and Baaijens, F., 1999, "The Relation between Single Crystal Elasticity and the Effective Elastic Behaviour of Polycrystalline Materials: Theory, Measurement and Computation," *Modelling and Simulation in Materials Science and Engineering*, **7**(6) pp. 909.
- [18] Chamati, H., Papanicolaou, N., Mishin, Y., 2006, "Embedded-Atom Potential for Fe and its Application to Self-Diffusion on Fe (1 0 0)," *Surface Science*, **600**(9) pp. 1793-1803.
- [19] Mendeleev, M., Han, S., Srolovitz, D., 2003, "Development of New Interatomic Potentials Appropriate for Crystalline and Liquid Iron," *Philosophical Magazine*, **83**(35) pp. 3977-3994.
- [20] Etesami, S. A., and Asadi, E., 2018, "Molecular Dynamics for Near Melting Temperatures Simulations of Metals using Modified Embedded-Atom Method," *Journal of Physics and Chemistry of Solids*, **112**pp. 61-72.
- [21] Mishin, Y., Farkas, D., Mehl, M., 1999, "Interatomic Potentials for Monoatomic Metals from Experimental Data and Ab Initio Calculations," *Physical Review B*, **59**(5) pp. 3393.
- [22] Mendeleev, M., Kramer, M., Becker, C. A., 2008, "Analysis of Semi-Empirical Interatomic Potentials Appropriate for Simulation of Crystalline and Liquid Al and Cu," *Philosophical Magazine*, **88**(12) pp. 1723-1750.
- [23] Pascuet, M., and Fernández, J. R., 2015, "Atomic Interaction of the MEAM Type for the Study of Intermetallics in the Al-U Alloy," *Journal of Nuclear Materials*, **467**pp. 229-239.
- [24] Jensen, B. D., Wise, K. E., and Odegard, G. M., 2015, "The Effect of Time Step, Thermostat, and Strain Rate on ReaxFF Simulations of Mechanical Failure in Diamond, Graphene, and Carbon Nanotube," *Journal of Computational Chemistry*, **36**(21) pp. 1587-1596.
- [25] Rayne, J., and Chandrasekhar, B., 1961, "Elastic Constants of Iron from 4.2 to 300 K," *Physical Review*, **122**(6) pp. 1714.
- [26] Theodorou, D. N., and Suter, U. W., 1986, "Atomistic Modeling of Mechanical Properties of Polymeric Glasses," *Macromolecules*, **19**(1) pp. 139-154.

## Case Study 1: Hydrogen Embrittlement of Metals

Chapter 6: Hydrogen Embrittlement of Iron: A Molecular Dynamics simulation study on the effect of hydrogen on mechanical properties

### **Authors:**

**Liam S. Morrissey\***, **Sam Nakhla**

### **CRedit author statement:**

**Liam S. Morrissey**: conceptualization, methodology, software, formal analysis, investigation, writing – original draft, **Sam Nakhla**: validation, resources, writing – review and editing, supervision

## Abstract

While significant research has been conducted on the various mechanisms of hydrogen embrittlement, there remains a lack of quantitative understanding on the effect of atomic hydrogen concentration on mechanical properties. Previous experimental work suggests that an increased hydrogen concentration will degrade both the elastic modulus and yield stress. However, experimental samples often contain other atomistic defects that make it difficult to determine the role hydrogen alone plays on material behaviour. Further, experimental studies are often unable to directly quantify the effect of hydrogen concentration on modulus. Therefore, the purpose of this study was to use molecular dynamics simulations to quantify the effect of interstitial hydrogen on the mechanical properties of perfect single crystal alpha iron during loading. Results demonstrated the potential type used significantly affected predicted results. The EAM potential for Fe-H systems was selected as it accurately predicted both the hydrogen free modulus and diffusion coefficient of hydrogen in iron. Atomic hydrogen between 0.5 - 5% was shown to linearly degrade the elastic modulus and stress to initiate dislocations at all temperatures considered. Increasing hydrogen concentration was shown to promote the formation of dislocations at a lower stress, resulting in a higher density of dislocation and shorter slip distances. Through demonstrating the effect of atomic hydrogen alone, without other atomistic defects, this study provides a foundation for better understanding the role of hydrogen on the degradation of mechanical properties during loading.

## Introduction

Hydrogen embrittlement (HE) is one of the most discussed and debated concepts in asset integrity studies of metals. As atomic hydrogen penetrates the surface and diffuses throughout the microstructure it can reduce ductility and lead to brittle failure with little warning. Previous research has documented the detrimental effects of HE on fracture toughness [1], fatigue strength [2], and on the promotion of environmentally assisted cracking [3]. Overall, HE represents both a significant safety and economic threat. However, what makes HE unique is its distinct multiscale nature; the macroscale failure events are precipitated by atomistic scale embrittlement processes. While the macroscale effects of hydrogen are generally agreed upon, the atomistic mechanisms causing the 'embrittlement' remain a contentious topic. As has been exhausted in several previous summary studies, three prominent models exist as the most referenced [4]. First, the hydrogen induced decohesion (HEDE) mechanism postulates that as atomic hydrogen accumulates in lattice sites it reduces the cohesive energy which leads to subcritical crack growth and a cleavage like failure [5]. Second, the hydrogen-enhanced localized plasticity (HELP) theory posits that embrittlement is a result of increased dislocation mobility which pile up at grain boundaries and crack tips [6]. More recently a third model has been proposed that suggests that the density and coalescence of vacancies is enhanced in the presence of atomic hydrogen [7,8]. In this study Nagumo et al. [8] demonstrated that hydrogen charged samples had a noticeably higher void density than uncharged samples after the same number of fatigue cycles.

Due to the atomistic nature of these mechanisms molecular dynamics (MD) simulations can be used to better understand the role hydrogen plays during loading. These simulations consider the system on an atomic scale and can model the interactions, bond breaking and bond formation between atoms during loading. For example, Song and Curtin [9] used MD to demonstrate the hydrogen

accumulation at crack tips, leading to the blocking of dislocation emissions and cleavage like crack growth. Similarly, Xie et al. [10] investigated the effect of hydrogen in heavily deformed alpha-iron. Yield strength was shown to be dependent on hydrogen concentration at edge defects. Building on these findings, Lv et al. [11] used MD to demonstrate a vacancy trapping effect in which hydrogen was shown to be strongly bound to vacancies. Finally, Islam et al. [12] used the ReaxFF potential to investigate the interaction of hydrogen with iron and iron carbide interfaces. Findings demonstrated that diffuse hydrogen lead to a decrease in the work of separation in the ferrite-cementite interface, endorsing a hydrogen decohesion behavior.

While particular attention has been paid to simulating the embrittlement mechanisms, there is considerably less research on the effect of hydrogen on mechanical properties. Previous experimental work has suggested that hydrogen will decrease both the elastic modulus and yield strength [13–15]. For example, Ortiz et al. [13] tested the effect of hydrogen on the modulus of various steels. Specimens were charged over 24 hours using a cathodic method and modulus was calculated using a resonance frequency method. All samples showed a reduction in modulus after charging that was linearly correlated to the hardness of the sample. Similarly, Zhang et al. [15] also observed a reduction in modulus after charging. However, due to the difficulty in measuring the exact concentration of hydrogen in the microstructure these experiments did not correlate the reduction in modulus to an exact concentration of hydrogen. These studies are therefore unable to directly quantify the relationship between hydrogen concentration and mechanical properties. Moreover, samples often contain voids, dislocations, impurities, and free surfaces, all of which can both effect elastic modulus and interact with hydrogen. It is therefore difficult to use experimental methods to delineate whether changes in modulus are due to hydrogen alone or a combination with other defects in the microstructure. Does atomic hydrogen need to interact with other defects in order to degrade mechanical properties? Inspired by

these difficulties, Yu et al. [16] used MD to simulate the effect of hydrogen on the mechanical properties of tungsten. Results demonstrated that hydrogen alone lead to a reduction in both modulus and yield strength with increasing lattice concentration. However, there is there is a lack of research on the effect diffuse atomic hydrogen alone has the mechanical properties of iron.

### Importance of Interatomic Potential

During an MD simulation the interatomic potential is used to describe forces between atoms, and thus reiterate the positions and velocities of atoms in the system [16]. Previous research has demonstrated that predicted mechanical properties are extremely dependent on the use of a suitable potential [17,18]. Therefore, selecting an accurate potential is critical to obtaining realistic simulation results. Overall there are several types of potentials, each with numerous subsets that have parameterized for different purposes. In addition, some potentials have been developed specifically for iron-hydrogen interactions. For example, a Finnis-Sinclair type embedded atom method (EAM) potential was developed to describe iron-hydrogen interactions [8,19]. This potential has been previously used to describe hydrogen clustering near crack tips [8] and hydrogen hardening in heavily deformed iron [9]. However, this potential has not been tested specifically for its ability to predict mechanical properties of pure or hydrogen embrittled iron. Therefore further research is needed to determine whether this potential is suitable to describe the effect of hydrogen on various mechanical properties.

While EAM type potentials are able to describe atomistic interactions, they are unable to account for the bond breaking and reformation that typically occurs during chemical reactions. In contrast, ReaxFF potentials are designed to allow for the dynamic simulation of bond breaking and reformation during a simulation. Unlike other potentials, ReaxFF models both connected and non-

bonded interactions. First, connectivity dependant reactions (valence and torsion energy) are design to eliminate their energy when bonds are broken. Non bonded interactions, van der Waals and Coulomb, are calculated regardless of connectivity between every atom pair in the set up. As a result, ReaxFF is able to describe both covalent and metallic systems. More detail on the ReaxFF method can be found in van Duin et al. [20]. ReaxFF potentials have been previously used to describe the diffusion and hydrogen-vacancy interactions in iron and stainless steel [11]. However, as with many hydrogen-iron simulations, no effort was made to determine the effect of diffuse hydrogen on the mechanical properties and behavior upon loading. Therefore the question remains as to whether ReaxFF potentials are able to capture the effect of hydrogen on mechanical properties.

## Purpose

As can be seen from the above review, while many experimental studies predict a detrimental effect due to hydrogen, there are often other atomistic flaws in the sample that make it difficult to determine the role hydrogen alone plays on material behaviour. As such, the motivation of the present study is to eliminate these complicating factors and attain an understanding of the base case: atomic hydrogen in a defect free single crystal. Only after the role of hydrogen alone is understood should other defects such cracks, voids, impurities, and grain boundaries be considered. Essentially, this study seeks to understand whether hydrogen alone can affect mechanical properties or if its interaction with voids and defects is critical to the embrittlement process. Unlike experimental methods, MD simulations can simulate perfect crystals while controlling the exact concentration of lattice hydrogen. Further, the case of single crystal embrittlement has extreme relevance to the ever-growing field of nanomaterials where these experiments are both difficult and expensive to conduct. The purpose of the current study was to use MD to simulate the effect of interstitial hydrogen on the mechanical properties of pure single crystal

alpha iron during loading. Further, the effect of temperature and dislocation interaction with hydrogen was also investigated to better understand the mechanisms of degradation.

## Methodology

### Simulation Set-up

Prior to adding in the diffuse hydrogen a  $15a \times 15a \times 15a$  (where  $a$  is the lattice constant of iron = 2.856 Å) slab of BCC alpha iron was created with periodic boundary conditions in the  $x$ ,  $y$  and  $z$  directions. The single crystal was oriented with the  $[100]$ ,  $[110]$ , and  $[110]$  directions along the  $x$ ,  $y$  and  $z$  axes respectively. Periodic boundary conditions were used to simulate an essentially infinite bulk and thus eliminate edge effects. Next, various concentrations of atomic hydrogen were added randomly to the lattice of the iron slab. Figure 6.1 provides a sample of a cube of pure iron before and after the addition of hydrogen.

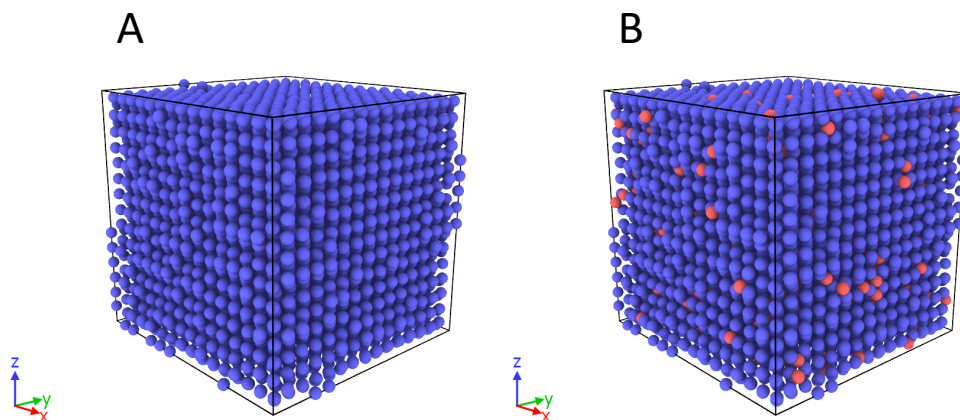


Figure 6.1 - Iron cube before (A) and after (B) addition of atomic hydrogen. Blue atoms are iron and red atoms are atomic hydrogen

Because hydrogen atoms were added randomly at interstitial sites, as opposed to a specific interstitial site (tetrahedral or octahedral), the next step was to equilibrate the slab and ensure that

hydrogen atoms were able to settle into the preferred low energy interstitial sites without any overlap. Following the procedures of similar MD atomistic hydrogen studies [16,22], a constant number, volume and energy (NVE) ensemble was first run for 10 ps to update the position and velocity for all atoms. A limit was imposed to ensure that the maximum distance an atom could move in each timestep was 0.001 Å [16]. During this phase the total atom number was tracked to ensure no hydrogen atoms were expelled from the system due to overlap or excessive energies. After the NVE was run and hydrogen atoms were in preferred sites the system was then equilibrated to the prescribed temperature using a constant number pressure and temperature (NPT) barostat over 10 ps. Tests were conducted using two different potentials that have been previously used in Fe-H systems; an EAM type developed by Song and Curtin [9] and a ReaxFF type developed by Islam et al. [12].

Hydrogen concentrations of 0%, 0.5%, 1%, 2.5%, and 5% were tested at 100K, 300K and 500K. It is important to note that these hydrogen concentrations are significantly higher than what would typically be observed in an experimental study. However, given the time constraints of MD simulations, many similar previous studies use these high concentrations to allow for the effect of hydrogen to be observed. For example, in a study on the combined effect of hydrogen and vacancies, Lv et al. [11] added 1% atomic hydrogen to the lattice. Similarly, in a study on the effect of hydrogen on crack propagation in iron, Song et al. [22] considered hydrogen concentrations between 0-6.1%. A summary of various similar studies is provided in table 6.1 to help justify the hydrogen concentrations chosen. Further, while perfect crystals were chosen to allow for an understanding of the base case, results also have relevance to nanomaterials where perfect single crystals are often used. Given that the purpose was to first understand the role hydrogen alone plays on mechanical properties during deformation, these higher values were deemed suitable.

Table 6.1. Summary of previous studies on hydrogen embrittlement simulations with relevant concentration

<b>Author</b>	<b>Purpose</b>	<b>Hydrogen Concentration</b>
Song et al. 2016 [22]	H in iron with crack	0-6.1%
Lv et al. 2018[11]	H in iron with vacancies	1%
Xie et al. 2011[10]	H in iron with dislocations	2%
Yu et al. 2012[16].	H in pure tungsten	0-12.5%

### Atomistic Tension Test

Following equilibration the slabs were then strained at a prescribed strain rate using an atomistic tension test [23]. Each slab was deformed in the x direction with a strain rate of 0.01 per picosecond and lateral boundaries controlled to zero pressure using a Nose-Hoover style NPT barostat to allow for natural Poisson contractions. While this strain rate is certainly higher than would be experienced during macroscale testing, it is below recommended values of Jensen et al. [24] who observed no difference in the elastic region and yielding below a critical strain rate value. This selection was verified by testing lower strain rates and observing no significant differences. Next, the corresponding stresses and strains were plotted to produce a stress strain curve for each case considered. The virial atomic stress tensor was used as it has been shown to be equivalent to the macroscale continuum stress [25]. Elastic modulus was calculated as the slope of the of the stress strain curve well within the elastic linear region (up to 2% strain) and peak stress was determined as the maximum stress in the linear region. All simulations were run in triplicate to attain various hydrogen distributions throughout the lattice.

## Results

### Effect of Hydrogen on Elastic Modulus

First, Figure 6.2 and Table 6.2 provide the predicted elastic modulus as a function of hydrogen content between 100K-500K for the EAM and ReaxFF potentials. For all temperatures and potentials considered the modulus decreased with increasing hydrogen content, as predicted by several experimental studies [13–15]. Therefore, hydrogen alone, without interaction with other material defects, was shown to reduce the elastic modulus. In addition, for both the EAM and ReaxFF potentials there was a linear relationship between percent reduction of elastic modulus and percent hydrogen. While both potentials agree on these trends, the extent of this reduction depends on the potential used to simulate the tensile test. For example, at 300K and 0% hydrogen both potentials predicted a similar elastic modulus of 140 and 136.4 GPa for EAM and ReaxFF, respectively. These values also agree well with experimental data for single crystal iron at room temperature (134 GPa) as reported by Simmons et al. [26]. Therefore, upon first inspection it would appear that both potentials can reasonably simulate the mechanical properties of iron. However, as the percentage of hydrogen in the lattice increases the EAM potential predicted a significantly larger drop in modulus at all temperatures considered. For example, at 5% hydrogen the EAM potential predicted an average drop in elastic modulus of 26.07%. At this same hydrogen content the ReaxFF potential predicted an average drop of only 7.99%. Therefore, while both potentials agree on the hydrogen free elastic modulus, there are significant discrepancies in the values of predicted elastic modulus once hydrogen is added. This is particularly interesting considering that both potentials have been used extensively to describe Fe-H systems.

Table 6.2 - Average percent reduction in elastic modulus for various concentrations and temperatures using EAM and ReaxFF potentials

Hydrogen (%)	Reduction in Elastic Modulus (%)					
	100K		300K		500K	
	EAM	ReaxFF	EAM	ReaxFF	EAM	ReaxFF
0.5	2.74%	0.68%	2.50%	0.95%	1.87%	0.77%
1	5.75%	1.64%	6.29%	1.69%	4.05%	1.85%
2.5	14.38%	3.34%	14.21%	3.67%	11.30%	3.47%
5	23.77%	7.37%	26.07%	7.99%	25.49%	7.63%
<b>R-squared</b>	98.69%	99.50%	99.59%	99.60%	99.78%	99.25%

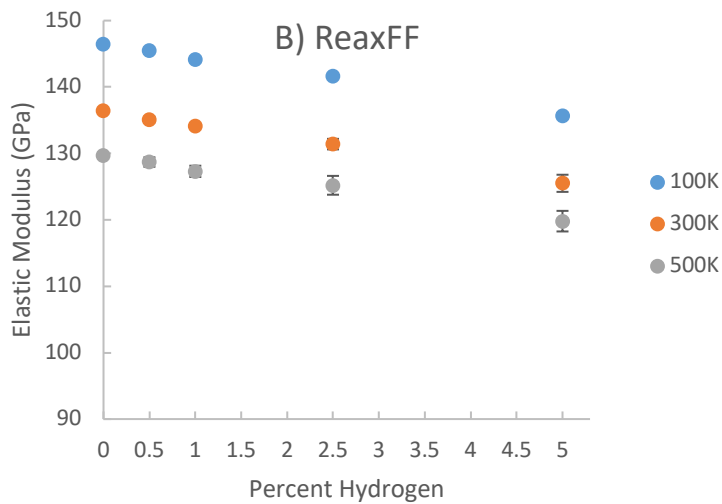
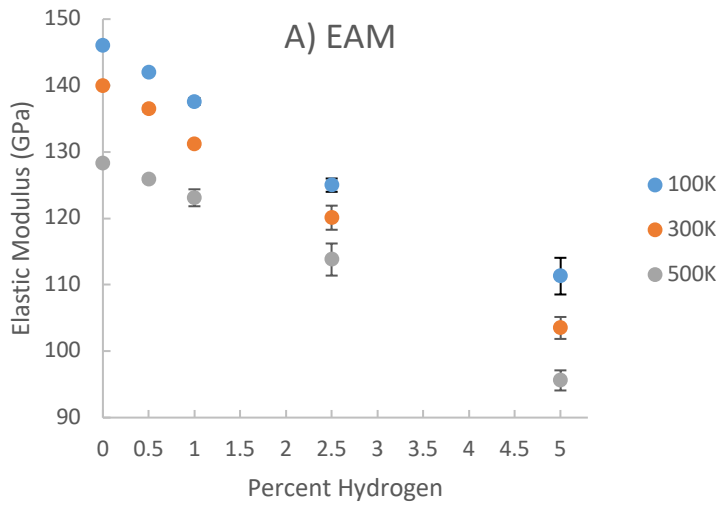


Figure 6.2 - Reduction in elastic modulus as a function of hydrogen concentration for EAM (A) and ReaxFF (B) potentials

### Comparison with Experimental data and Assessment of Potential

While the usefulness of MD simulations to better understand HE is unquestioned, one particular challenge is the lack of experimental data that correlates the percentage of atomic hydrogen with reduction in elastic modulus. As shown above, both potentials predicted a linear decrease in modulus with increasing concentration. This trend agrees with the limited experimental results that have shown a reduction in modulus after charging with hydrogen [12–14]. However, it is important to note that comparison with experimental studies is qualitative at best. Experimental studies contain samples with a multitude of other defects including voids, microcracks, impurities, grain boundaries and free surfaces. Further, these studies are often unable to accurately determine or control the exact concentration of hydrogen in the lattice and therefore cannot quantitatively describe the effect of increasing hydrogen concentration on mechanical properties. As discussed above, the motivation of the present study is to eliminate these complicating factors to understand the role hydrogen alone plays on mechanical properties.

While the reduction in elastic modulus may not have exact experimental data available for comparison, there are other important parameters that can be used to provide insight into which potential is likely more accurate. Hydrogen diffusion in the lattice is an important process both for the reduction in elastic modulus and for the subsequent embrittlement during flaw development and crack growth. For example, hydrogen has been shown to diffuse to crack tip sites and suppress dislocation emissions, thus encouraging brittle cleavage like failure as opposed to crack blunting and plastic failure [8]. Similarly, Yu et al. [15] demonstrated that diffuse hydrogen in tungsten encouraged slipping of

dislocations earlier than in hydrogen free samples. Therefore, an accurate hydrogen diffusion coefficient is critical to simulating realizable HE events. As such, each potential was also evaluated based on its ability to predict the diffusion coefficient of atomic hydrogen in pure iron.

Following the work of Lv et al. [10] for calculating a diffusion coefficient, hydrogen at 1% was added to a 15x15x15 lattice unit periodic cube of pure iron. Similar to the above method, after adding the hydrogen the system was first relaxed and then equilibrated to 300K using a Nose-Hoover style NPT ensemble over 10ps. Following equilibration the mean square displacement (MSD) of hydrogen atoms was sampled over 2ns to allow ample time for reliable diffusivity data extraction. The diffusion coefficient of hydrogen over the simulation time ( $t$ ) in iron was then calculated based on the Einstein equation:

$$D = \frac{\langle R^2 \rangle}{6t} \quad (1)$$

Where  $\langle R^2 \rangle$  is the MSD of all H atoms in the iron cube.

Based on this equation the diffusion coefficient can therefore be calculated as 1/6 of the slope of a plot of MSD vs. time. At 300K this curve was highly linear for both potentials tested, suggesting adequate sampling time and the accuracy of the approximation in Equation 1 (Figure 6.3). Results were compared to experimental diffusion coefficients for hydrogen in pure iron at 300K using an electrochemical method [25].

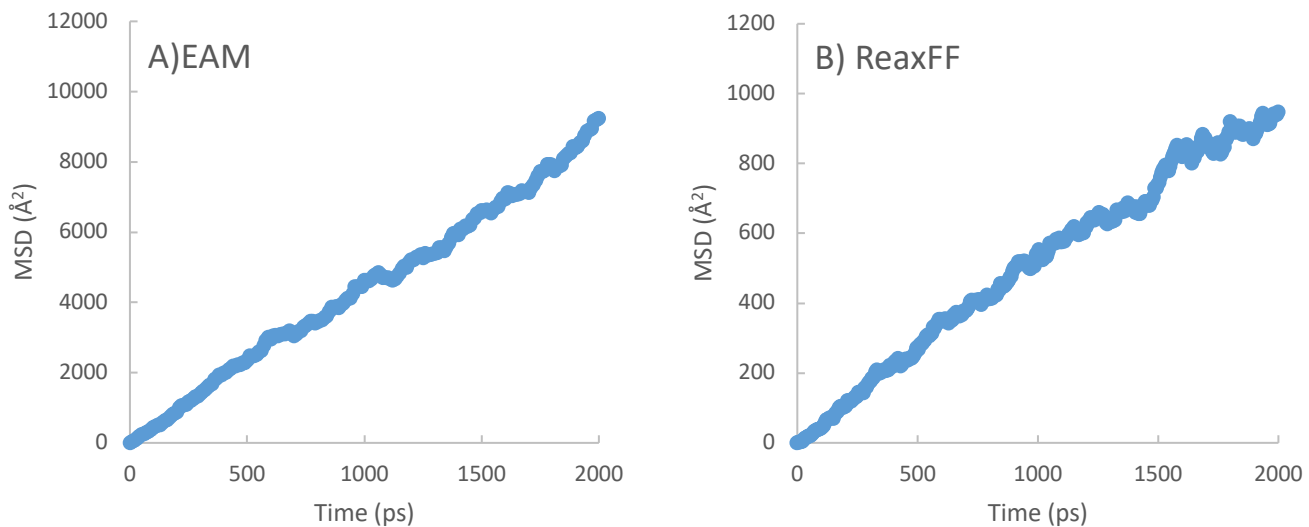


Figure 6.3 - Mean Square Displacement (MSD) vs time for EAM (A) and ReaxFF (B) potentials used to calculate diffusion coefficient

There was a large discrepancy in the accuracy of predicted diffusion coefficients. As compared to experimental values (Table 6.3), The EAM potential predicted the diffusion coefficient within 3% accuracy. In contrast, the ReaxFF potential under predicted the diffusion by almost 90%. This finding agrees closely with the work of Islam et al. [12] who also observed a significant under prediction of the diffusion coefficient of hydrogen when developing the CHFe ReaxFF potential. Error was attributed to the higher lattice concentrations considered and the time scales of MD simulations. However, given the same time scale restrictions the EAM type potential was significantly more accurate. Therefore, the EAM potential is able to accurately predict both the bulk hydrogen free elastic modulus and the diffusion coefficient of hydrogen within the iron lattice. As such, this potential was selected to further investigate the degradation of mechanical properties caused by diffuse hydrogen. This initial exercise also highlights the importance of extensively testing a potential prior to application. Many studies select a potential

based on the fact it has been used by previous researchers or on the results of simple tests. However, even though the ReaxFF potential has been used extensively in previous research and predicted an accurate modulus for pure iron, it still had significant limitations for hydrogen embrittlement simulations.

Table 6.3: Predicted diffusion coefficients and associated error as compared to experimental values [25]

<b>Potential</b>	<b>Diffusion Coefficient</b>		<b>Error</b>
	<b>Predicted</b>	<b>Experimental</b>	
EAM	7.23E-09	7.00E-09	3%
ReaxFF	7.70E-10	7.00E-09	-89%

### Effect of Hydrogen on Dislocation Formation

After studying the effect on elastic modulus and selecting a suitable potential the next step was to consider the effect of hydrogen on the properties and microstructure beyond the elastic region. Referring to Figures 4 and 5, at all concentrations considered there was a linear elastic region, followed by a peak in the stress strain curve. Given the periodic boundary conditions it is impossible to see necking in the cube during straining [16]. Therefore, the peak in the stress strain curves represents the critical stress to nucleate dislocations and activate slip as opposed to the tensile strength. Because the materials do not possess free surfaces, pre-existing dislocations, or grain boundaries this peak value is an order of magnitude higher than what is typically observed for macroscale samples and agrees better with the inherent tensile strength of the material. This value represents the maximum theoretical strength of a material based on the stability of the lattice and is an upper bound of potential strength of a 'perfect' material [16].

Figures 6.4 and 6.5 show the microstructure of the periodic iron cube at 300K at various strains for the case of 0.5% hydrogen and 5% hydrogen using the EAM potential. First, in both cases at 2.5% strain the iron cube is within the elastic region and thus has a well ordered BCC structure with no dislocations. However, at 5% hydrogen dislocations begin to nucleate at 5.75% strain and 5.84 GPa. In contrast, at 0.5% hydrogen dislocations nucleate at both a higher strain and higher stress. Therefore, with increasing hydrogen concentration there was a decrease in the amount of stresses needed to nucleate dislocations. In all cases dislocations have Burgers vectors of the type  $a/2 \langle 111 \rangle$ . Further, in both cases as strain increased beyond the peak a network of edge dislocations and stacking faults began to form in the cube. At 5% hydrogen this network formed at both a lower stress and strain. Referring to table 4, for all temperatures considered an increased hydrogen concentration was shown to decrease the critical stress to activate dislocations as compared to the hydrogen free sample. This stress decreased linearly with hydrogen concentration at all temperatures. Therefore, hydrogen alone in a perfect crystal was shown to linearly reduce the stress necessary to initiate dislocations in a perfect single crystal.

Table 6.4. Percent reduction in stress at dislocation initiation as compared to hydrogen free samples for various concentrations and temperatures using EAM potential

<b>Reduction in Stress at Dislocation Initiation (%)</b>			
<b>Hydrogen (%)</b>	<b>100K</b>	<b>300K</b>	<b>500K</b>
0.5	4.84%	5.26%	5.33%
1	8.87%	6.32%	8.00%
2.5	20.97%	17.89%	18.67%
5	36.29%	34.74%	33.33%
<b>R-squared</b>	99.48%	99.51%	99.82%

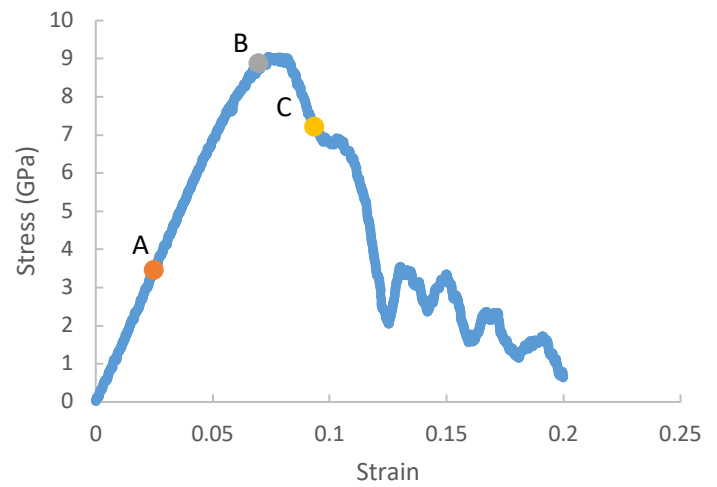
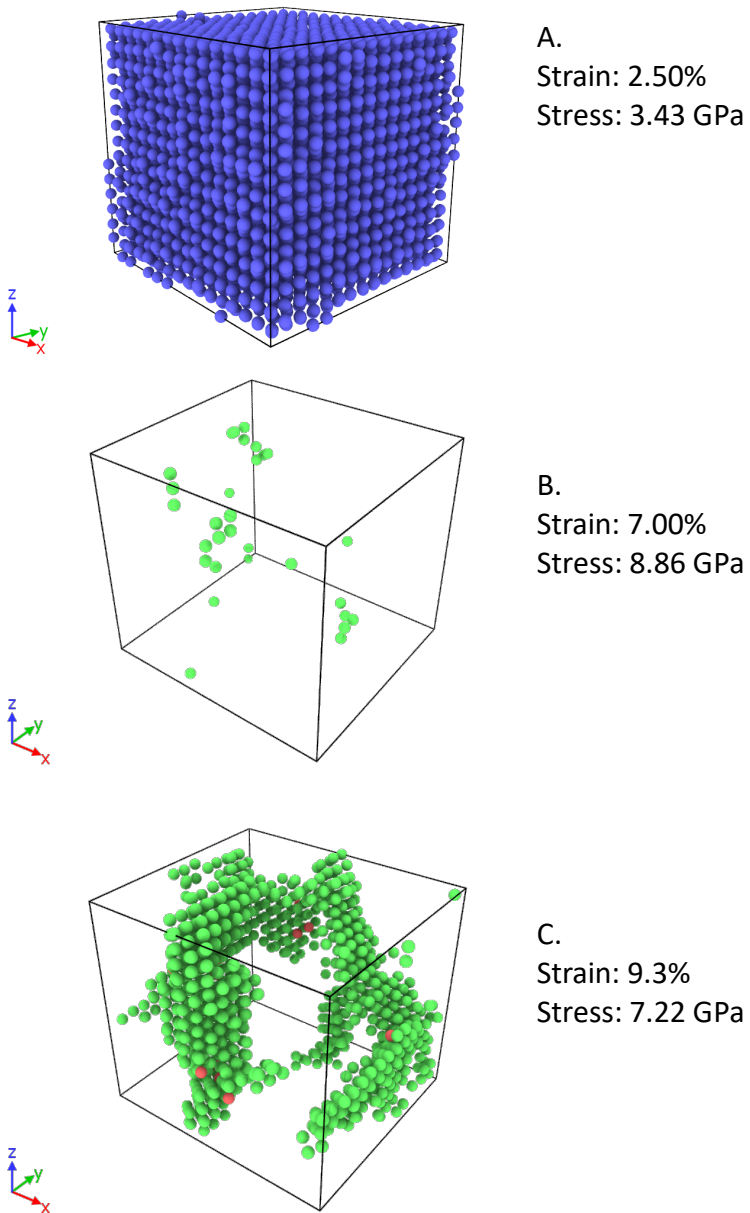


Figure 6.4 - Microstructure of iron cube with 0.5% hydrogen at various strains (A, B, C) with corresponding stress strain curve (D) Blue atoms are BCC and green atoms are dislocation atoms.

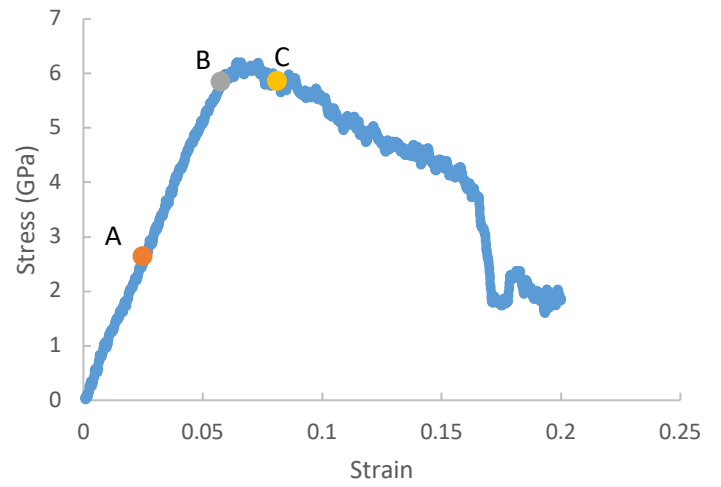
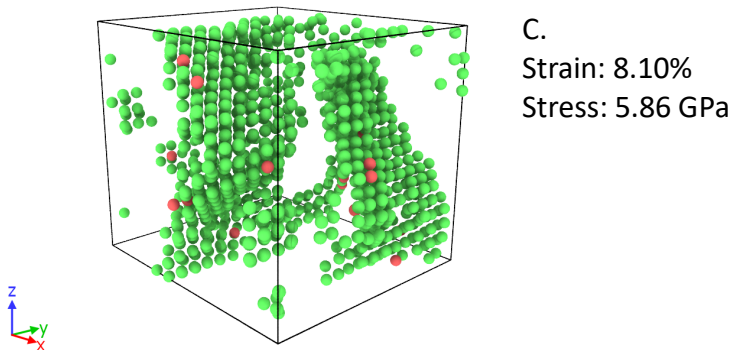
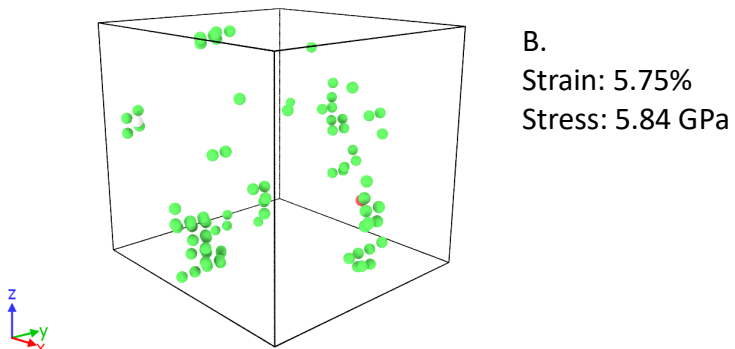
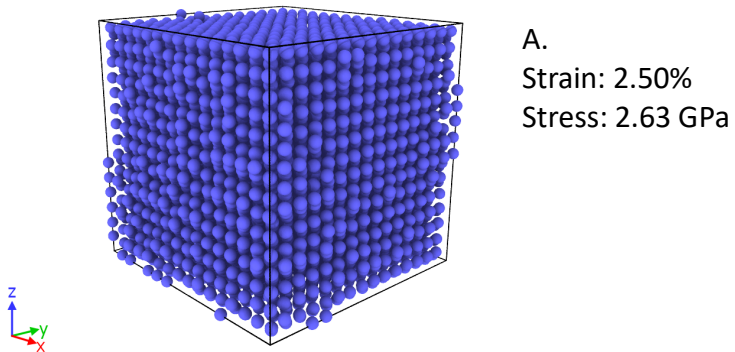


Figure 6.5 - Microstructure of iron cube with 5% hydrogen at various strains (A, B, C) with corresponding stress strain curve (D). Blue atoms are BCC and green atoms are dislocation atoms.

In an effort to source the reason for this reduction in stress, bond distances in a BCC unit cell were tracked with and without the presence of atomic hydrogen in the energetically favorable tetrahedral interstitial sites [27]. Based on the size of atomic hydrogen, it can be tempting to assume that hydrogen alone will not be able to disrupt the well ordered lattice of a crystalline material. However, when tracking distances between neighboring atoms it can be seen that the presence of an interstitial hydrogen atom lead to distortion of the lattice (Figure 6.6 and Table 6.5). Further, the H atom interrupts bonding between atoms 5-6 and 2-3. Bond strength in these distorted lattices are therefore reduced [16], and leads to a reduction in the stress needed to form dislocations.

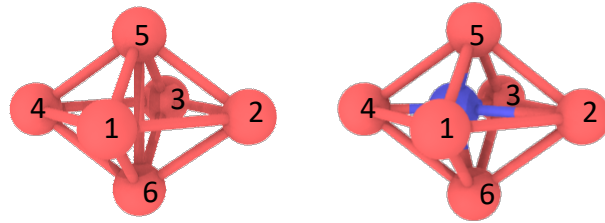


Figure 6.6: BCC Iron lattice arrangement with and without hydrogen in the tetrahedral interstitial site

Bond Atoms	H Free Bond Distance (Å)	H in Tetrahedral Interstitial Site Bond Distance (Å)
2-3	2.87	2.91
3-4	2.87	2.91
1-5	2.49	2.52
2-5	2.49	2.52
3-5	2.49	2.63
4-5	2.49	2.63

Table 6.5: Bond Distance changes between BCC atoms with and without interstitial hydrogen

## Effect of Hydrogen on Lattice and Deformation Mechanism

As hydrogen in the lattice increases the modulus and peak stress decline. However, the steepness in the drop is highest in the case of hydrogen free specimens and significantly decreases as hydrogen content increases (Figure 6.7). This suggests that as hydrogen content increases there is a change in the slipping mechanism with hydrogen. For BCC metals plastic deformation typically occurs via slipping of dislocations along 48 different slip systems. At zero to low concentrations the integrity of the lattice is less disturbed and once  $a/2 \langle 111 \rangle$  dislocations are nucleated they can quickly slip in the  $\{110\}$  planes (Figure 6.8A). This can be seen in the sharp decline in stress seen in the stress strain curves for 0.5% lattice hydrogen (Figure 6.7). However, at higher concentrations ( $>2.5\%$ ) there are far more interstitial hydrogen atoms and thus more lattice disruptions. This leads to both a lower stress and strain needed to form dislocations throughout the lattice and results in a higher density of dislocations. Referring to Figure 6.8B, perpendicular dislocations impeded long distance slips and instead, only short distance slipping was observed. This is reflected in the stress strain curve where at 5% hydrogen the short distance slipping leads to a lower and smoother drop in stress after reaching the peak. Therefore, with increasing hydrogen concentration there are more lattice disruptions resulting in more dislocations and shorter slip distances. Due to the simulation size these slip distances likely do not correspond directly to macroscale values. Nonetheless, the MD simulations demonstrate that hydrogen alone can effect the lattice disruptions, dislocation density, and, ultimately, the slipping mechanisms during deformation.

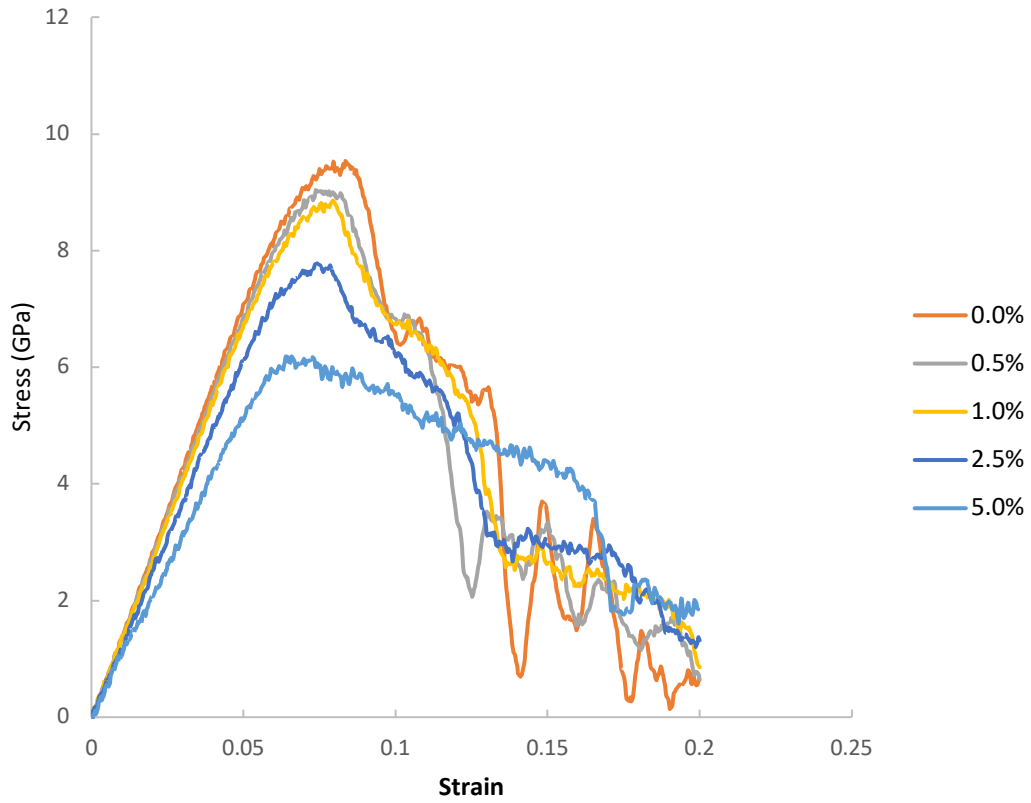


Figure 6.7: Stress strain curves for iron slab at 300K with various hydrogen concentrations in the lattice

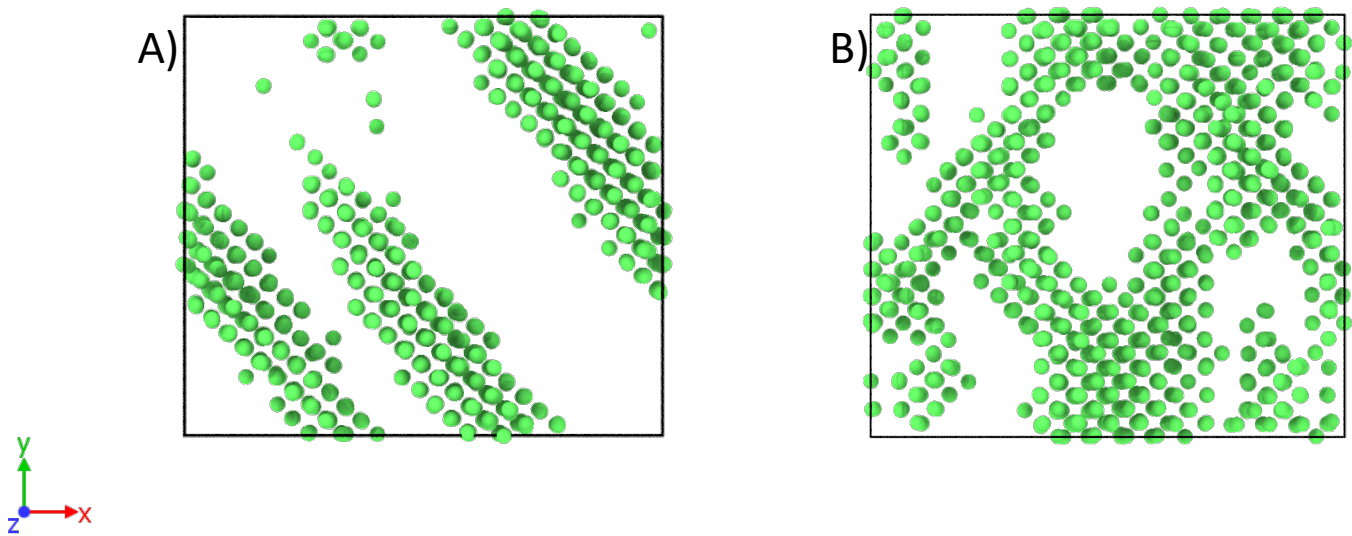


Figure 6.8:  $a/2 \langle 111 \rangle$  Dislocations in iron sample after reaching peak stress for case of 0.5% hydrogen (A) and 5% hydrogen (B)

## Conclusions

Understanding the hydrogen embrittlement process is critical for predicting the behavior and remaining life of materials subjected to high concentrations of hydrogen. While previous experimental studies agree that there is a degradation in mechanical properties associated with hydrogen embrittlement, they are unable to directly quantify and control the hydrogen concentration in the lattice. Further, these studies are almost always complicated by the presence of other microstructural defects in addition to lattice hydrogen. As such, it is unknown whether hydrogen alone can affect mechanical properties or if its interaction with voids and defects is critical to the degradation process. An understanding of the base case of atomic hydrogen in a perfect sample is needed before interactions with these defects should be added. This study used MD to model the mechanical behavior of perfect iron samples under loading with various concentrations of lattice hydrogen. Findings demonstrated that increasing diffuse hydrogen resulted in a linear decrease in the elastic modulus and stress at dislocation initiation. Moreover, as the concentration of hydrogen increased there was a higher density of dislocations after reaching peak stress. This leads to increased dislocation interaction and shorter slip distances, corresponding to less steep declines in the stress strain curve after reaching the peak stress. Overall, hydrogen was shown to promote the nucleation and propagation of dislocations in the lattice, resulting in a lower elastic modulus and peak stress. In summary, this study demonstrates that hydrogen alone in a single crystal, without interactions with other defects, can still have a significant effect on mechanical properties and behavior during loading. Future work will then build on this base case by systematically add in these defects to better understand their interplay with hydrogen and the embrittlement process.

## References

- [1] Robinson, S. L., and Moody, N. R., 1986, "The Effect of Hydrogen, Tritium and Decay Helium on the Fracture Toughness of a Stainless Steel Superalloy," *J. Nucl. Mater.*, **140**(3), pp. 245–251.
- [2] Toplosky, J., and Ritchie, R. O., 1981, "On the Influence of Gaseous Hydrogen in Decelerating Fatigue Crack Growth Rates in Ultrahigh Strength Steels," *Scr. Metall.*, **15**(8), pp. 905–908.
- [3] Chen, W., Kania, R., Worthingham, R., and Boven, G. V., 2009, "Transgranular Crack Growth in the Pipeline Steels Exposed to Near-Neutral PH Soil Aqueous Solutions: The Role of Hydrogen," *Acta Mater.*, **57**(20), pp. 6200–6214.
- [4] Robertson, I. M., Sofronis, P., Nagao, A., Martin, M. L., Wang, S., Gross, D. W., and Nygren, K. E., 2015, "Hydrogen Embrittlement Understood," *Metall. Mater. Trans. A*, **46**(6), pp. 2323–2341.
- [5] Oriani, R. A., and Josephic, P. H., 1974, "Equilibrium Aspects of Hydrogen-Induced Cracking of Steels," *Acta Metall.*, **22**(9), pp. 1065–1074.
- [6] Birnbaum, H. K., and Sofronis, P., 1994, "Hydrogen-Enhanced Localized Plasticity—a Mechanism for Hydrogen-Related Fracture," *Mater. Sci. Eng. A*, **176**(1–2), pp. 191–202.
- [7] Morrissey, L. S., Handrigan, S. M., and Nakhla, S., 2019, "Quantifying Void Formation and Changes to Microstructure during Hydrogen Charging: A Precursor to Embrittlement and Blistering," *Metall. Mater. Trans. A*, **50**(3), pp. 1460–1467.
- [8] Nagumo, M., 2004, "Hydrogen Related Failure of Steels—a New Aspect," *Mater. Sci. Technol.*, **20**(8), pp. 940–950.
- [9] Song, J., and Curtin, W. A., 2013, "Atomic Mechanism and Prediction of Hydrogen Embrittlement in Iron," *Nat. Mater.*, **12**(2), pp. 145–151.
- [10] Xie, W., Liu, X., Chen, W., and Zhang, H., 2011, "Hydrogen Hardening Effect in Heavily Deformed Single Crystal  $\alpha$ -Fe," *Comput. Mater. Sci.*, **50**(12), pp. 3397–3402.
- [11] Lv, G., Zhang, M., Zhang, H., and Su, Y., 2018, "Hydrogen Diffusion and Vacancy Clusterization in Iron," *Int. J. Hydrogen Energy*, **43**(32), pp. 15378–15385.
- [12] Islam, M. M., Zou, C., van Duin, A. C. T., and Raman, S., 2016, "Interactions of Hydrogen with the Iron and Iron Carbide Interfaces: A ReaxFF Molecular Dynamics Study," *Phys. Chem. Chem. Phys.*, **18**(2), pp. 761–771.
- [13] Ortiz, M., and Ovejero-Garcia, J., 1992, "Effect of Hydrogen on Young's Modulus of AISI 1005 and 1070 Steels," *J. Mater. Sci.*, **27**(24), pp. 6777–6781.
- [14] Kuopanportti, P., Hayward, E., Fu, C.-C., Kuronen, A., and Nordlund, K., 2016, "Interatomic Fe-H Potential for Irradiation and Embrittlement Simulations," *Comput. Mater. Sci.*, **111**, pp. 525–531.
- [15] Zhang, T.-Y., Jiang, F.-X., Chu, W.-Y., and Hsiao, C.-M., 1985, "Effect of Hydrogen on the Young's Modulus of Iron," *Metall. Trans. A*, **16**(9), pp. 1655–1662.
- [16] Yu, X., Gou, F., and Tian, X., 2013, "Molecular Dynamics Study of the Effect of Hydrogen on the Mechanical Properties of Tungsten," *J. Nucl. Mater.*, **441**(1–3), pp. 324–330.

- [17] Plimpton, S. J., and Thompson, A. P., 2012, "Computational Aspects of Many-Body Potentials," *MRS Bull.*, **37**(5), pp. 513–521.
- [18] Subedi, S., Morrissey, L. S., Handrigan, S. M., and Nakhla, S., 2020, "The Effect of Many-Body Potential Type and Parameterisation on the Accuracy of Predicting Mechanical Properties of Aluminium Using Molecular Dynamics," *Mol. Simul.*, **46**(4), pp. 271–278.
- [19] Morrissey, L. S., Handrigan, S. M., Subedi, S., and Nakhla, S., 2019, "Atomistic Uniaxial Tension Tests: Investigating Various Many-Body Potentials for Their Ability to Produce Accurate Stress Strain Curves Using Molecular Dynamics Simulations," *Mol. Simul.*, **45**(6), pp. 501–508.
- [20] Ackland, G. J., Bacon, D. J., Calder, A. F., and Harry, T., 1997, "Computer Simulation of Point Defect Properties in Dilute Fe—Cu Alloy Using a Many-Body Interatomic Potential," *Philos. Mag. A*, **75**(3), pp. 713–732.
- [21] Van Duin, A. C. T., Dasgupta, S., Lorant, F., and Goddard, W. A., 2001, "ReaxFF: A Reactive Force Field for Hydrocarbons," *J. Phys. Chem. A*, **105**(41), pp. 9396–9409.
- [22] Song, H. Y., Zhang, L., and Xiao, M. X., 2016, "Molecular Dynamics Simulation of Effect of Hydrogen Atoms on Crack Propagation Behavior of  $\alpha$ -Fe," *Phys. Lett. A*, **380**(48), pp. 4049–4056.
- [23] Brown, D., and Clarke, J. H. R., 1991, "Molecular Dynamics Simulation of an Amorphous Polymer under Tension. 1. Phenomenology," *Macromolecules*, **24**(8), pp. 2075–2082.
- [24] Jensen, B. D., Wise, K. E., and Odegard, G. M., 2015, "The Effect of Time Step, Thermostat, and Strain Rate on ReaxFF Simulations of Mechanical Failure in Diamond, Graphene, and Carbon Nanotube," *J. Comput. Chem.*, **36**(21), pp. 1587–1596.
- [25] Subramaniyan, A. K., and Sun, C. T., 2008, "Continuum Interpretation of Virial Stress in Molecular Simulations," *Int. J. Solids Struct.*, **45**(14–15), pp. 4340–4346.
- [26] Simmons, G., 1965, *Single Crystal Elastic Constants and Calculated Aggregate Properties*, Southern Methodist Univ Dallas Tex.
- [27] Jiang, D. E., and Carter, E. A., 2004, "Diffusion of Interstitial Hydrogen into and through Bcc Fe from First Principles," *Phys. Rev. B*, **70**(6), p. 64102.

## Case Study 2: Atomic Impacts in Space

### Chapter 7: Erosion of Spacecraft Metals due to Atomic Oxygen: A Molecular Dynamics Simulation

**Authors:**

**Liam S. Morrissey, Stephen M. Handrigan, Sam Nakhla, Ali Rahnamoun**

**CRedit author statement:**

**Liam S. Morrissey:** conceptualization, methodology, software, formal analysis, investigation, writing – original draft, **Stephen M. Handrigan:** software, writing – review and editing, **Sam Nakhla:** validation, resources, writing – review and editing, supervision, **Ali Rahnamoun:** conceptualization, formal analysis, writing – review and editing

**Published:** **Morrissey, L. S.,** Handrigan, S. M., Nakhla, S., & Rahnamoun, A. (2019). Erosion of Spacecraft Metals due to Atomic Oxygen: A Molecular Dynamics Simulation. *Journal of Spacecraft and Rockets*, 1-6.

## Abstract

Atomic oxygen (AO) impacts on spacecraft materials represent one of the biggest threats to material performance in low Earth orbit (LEO). However, testing material performance in LEO is difficult and can be cost prohibitive. As a result, research has shown the potential to use the ReaxFF force field in molecular dynamics to describe the degradation process of several commonly used polymers. However, no research has been conducted on using ReaxFF to model AO impacts on spacecraft metals such as silver and gold. Therefore, the purpose of this study was to investigate whether ReaxFF can accurately model the impact of high energy AO on silver and gold. These simulations studied both the erosion and temperature evolution of the slab as a function of the number of impacting oxygen atoms. Overall, after impact with 100 oxygen atoms the erosion coefficient of silver closely matched previously reported test flight results for erosion in LEO. To verify the process, the simulations were also run with gold, a metal known to resist degradation. Unlike the silver slab, gold showed very little erosion after 100 impacts; again matching flight results in LEO. These results clearly demonstrate the potential of ReaxFF as a cost effective method to simulate test conditions in the LEO.

## Introduction

One of the biggest threats to materials exposed to the low Earth orbit (LEO) environment is high-energy collisions with atomic oxygen. Due to the high relative speeds between orbiting space crafts and atmospheric oxygen, these collisions can reach energies as high as 4.5 eV [1-2]. Depending on the material, collisions with this energy can lead to material loss, thus reducing instrumentation performance over longer durations. Overall, significant in-situ measurements have been performed on the effect of atomic oxygen on a wide range of materials [3-4]. Results show that while atomic oxygen is highly reactive with many polymers, its effect on metals varies significantly. Two of the most common metals found on spacecrafts are gold and silver. Silver is a critical component for electrical applications while gold is commonly used as a coating its low erosion rates and ability to absorb visible light [3]. Moreover, while gold shows very little erosion due to atomic oxygen, silver is highly reactive with significant material degradation over prolonged exposure [3]. Therefore, due to the large differences in performance than can exist amongst various materials, they must each be tested in LEO for their performance prior to application. However, due to the high cost of space launches and constant uncertainty in budgets, these tests are not always feasible. Therefore, a way to accurately model the effect of atomic oxygen on surfaces could both enhance the accuracy of remaining life predictions and eliminate the need to test new materials in LEO. While atomic oxygen testing facilities certainly offer a viable option, they too are costly, require advanced equipment, and cannot always replicate the harsh space environment.

As an alternative, molecular dynamics (MD) simulations have been used to accurately model and analyze surface reactions on the atom scale since the 1960s [5]. MD allows for the simulation of processes on the atomistic scale, and, depending on the force field being used, can actually model the

bond breaking and formation as chemical reactions occur. Therefore, MD provides an exciting potential to actually model the atomic interactions during AO impact, as opposed to simply viewing the macroscale surface after the collisions have occurred. Recently, studies by Rahnamoun and van Duin [6], and Zeng et al. [7] have used MD to model the effect of AO on several commonly used polymers in the space environment. First, Rahnamoun and van Duin used the ReaxFF force field to study the effect of atomic oxygen impacts on Kapton, POSS polyamide, and amorphous silica. In this study atomic oxygen was propelled towards a small substrate of each material. As atoms were sputtered due to the high energy collisions, the mass loss, temperature growth, and erosion coefficients were calculated and compared to experimental values. Results showed good agreement with experimental data and concluded that the temperature evolution on the surface was critical to predicting whether erosion and material loss would occur [6]. Building on this study, Zeng et al. used the ReaxFF force field to study the impact of atomic oxygen on the disintegration of Polyvinylidene fluoride or polyvinylidene difluoride (PVDF) and fluoropropyl polyhedral oligomeric silsesquioxanes (FP-POSS), two commonly used spacecraft polymers. Again, small simulated substrates were impacted with atomic oxygen until material loss occurred. Results showed that PVDF continuously eroded due to atomic oxygen while FP-POSS did not erode until after a specific number of AO impacts [7]. Therefore, these two studies clearly demonstrate the exciting potential for MD simulations to predict the effect of atomic oxygen on spacecraft polymers.

Overall, while research exists for the atomic oxygen erosion of polymers, the potential for molecular dynamics to model the effect of atomic oxygen on metals has yet to be studied. Moreover, because bonding for amorphous polymers and crystalline metals is quite different, accuracy for polymers cannot be used to conclude that molecular dynamics will be accurate for metals as well. In addition, because molecular dynamics is dependent on the force field chosen by the user, the force

fields chosen for metals will be unique from polymer force fields that consist mainly of C/H/O. Force fields are also sensitive to the partial charges of the atoms in the simulation model. However, this charge is not constant and is affected by factors like environmental condition and oxidation state of the metal. In addition, the outermost orbital for metals (d- or f-) can cause more complicated chemical bonding characteristics. Furthermore, there can be multiple oxidation states and coordination numbers for a metal. All of these factors increase the challenge of simulating systems that include metals.

### Purpose of Study: MD Simulations of Metals

While many spacecraft metals are assumed to be non-reactive with atomic oxygen, there may exist an energy barrier, that with a harsh enough environment or significant exposure, could be overcome. For example, as space missions move further into the solar system there becomes an increased risk of significantly higher speed collisions with both interstellar dust and heavy atoms [8]. Therefore, metals that were once considered 'immune' to erosion will need to be modelled again for these higher energy collisions. However, before this can be done, the accuracy of using molecular dynamics for high-speed collisions with metals must be verified by comparing with readily available experimental data from LEO.

As a result, the purpose of this paper is to investigate whether molecular dynamics can be used to model the effect of atomic oxygen on several commonly used metals for the space environment. This paper will model the LEO atomic oxygen interactions with silver and gold and will compare findings with available experimental data.

## Methodology

### ReaxFF reactive molecular simulation force field

One of the most important choices a user makes in any molecular dynamics simulation is the force field that is used to model the atomistic interactions. However, what makes the atomic oxygen simulation unique is that it requires a force field that can describe the bond breaking and formation during repeated impacts. As a result, several traditional force fields are not applicable as they do not consider the breakage of bonds or reactions. In contrast, the reactive force field (ReaxFF) is a bond order based force field method that allows for the dynamic simulation of bond breaking and reformation in a body. Therefore, this force field is uniquely positioned to model the breakage of materials due to atomic oxygen erosion. In the ReaxFF force field, the energy of the system is calculated as a combination of the partial energy contributions from the bond, over- and under-coordination, lone pair, valence, torsion, van der Waals, and Coulomb energy [9] (Equation 1):

(1)

$$E_{system} = E_{bond} + E_{over} + E_{under} + E_{lp} + E_{val} + E_{tor} + E_{vdWaals} + E_{Coulomb}$$

Bond order is then used to determine the interactions between all atoms in the system. The bond order accounts for contributions from sigma, pi, and double pi-bonds as a continuous function of the distance between atoms via equation 2:

(2)

$$BO_{ij}^i = BO_{ij}^\sigma + BO_{ij}^\pi + BO_{ij}^{\pi\pi}$$

ReaxFF models both connectivity dependent and non-bonded interactions. Connectivity dependent reactions, valence and torsion energy, are contingent on bond order such that when bonds are broken their energy is eliminated. Non-bonded interactions, van der Waals and Coulomb interactions, are calculated regardless of connectivity between every atom pair in the set up. Therefore, this combination of bonded and non-bonded interactions allows ReaxFF to describe both covalent and metallic systems. More detail on the ReaxFF method can be found in van Duin et al. [9]. Therefore, following the work of Rahnamoun and van Duin and Zeng et al., the ReaxFF force field was used in this study.

For the silver and oxygen model, the force field developed by Lloyd et al. [10] was used. This force field was initially developed to describe interaction of silver on zinc oxide surfaces. Results accurately reproduced equations of state for silver, silver zinc alloy, and silver oxide crystals [10]. Therefore, given that it is accurate for both pure silver and silver oxides, the force field was deemed suitable.

For the gold and oxygen model the force field developed by Joshi et al. [11] was used. This force field was initially developed to model the gold-oxygen binary system, and later developed to include the other elements [11]. The gold-oxygen system was parameterized based on data sets that included equations of state, heat of formation, and binding energies. Moreover, the force field was shown to accurately predict the diffusion properties of oxygen on a gold surface and oxidation rates [11].

#### Simulation Model for Atomic Oxygen Impact

Prior to impacting with atomic oxygen, 32x32x40 Angstrom slabs of pure gold and silver were developed. Referring to Figure 7.1, after preparation, each slab was placed in a 100Å high box with

periodic boundary conditions in the x and y directions and fixed in the z direction. Next, an *NVT* (constant number of atoms; N, volume; V, and Temperature; T) thermostat was used to equilibrate the slab with the open surface in the z direction inside the periodic box at 200K.

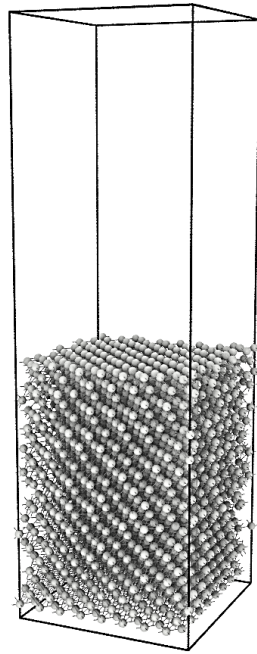


Figure 7.1 - Initial silver substrate set up in well prior to atomic oxygen impact

After the system was stabilized to 200K it was then ready for impact with atomic oxygen. Following previous work, at every 200 fs (400 simulation steps), one atomic oxygen was deposited into the system with a speed of -7.4 km/s (4.5 eV) in the z-direction at a randomly generated x- and y-position [6-7]. During deposition and subsequent impact, the thermostat was removed and an NVE (constant number of atoms; N, Volume; V, and Energy; E) simulation was run to fix the number and volume of the system while allowing the temperature to increase. In total, 100 oxygen atoms were

emitted during the first 40000 time steps for a total simulation time of 20 ps. Table 7.1 summarizes the parameters used for the molecular dynamics model.

	<b>Silver</b>	<b>Gold</b>
Lattice spacing	4.08	4.07
Timestep (fs)	0.5	0.5
Density (g/cm <sup>3</sup> )	10.5	19.3
Atomic Mass	107.9	197
Force Field	Lloyd 2016	Joshi 2010
Number of AO	100	100
AO Speed (km/s)	7.4	7.4
Time between impact (fs)	200	200
Substrate Dimension (lattice units)	8 x 8 x 10	8 x 8 x 10

Table 7.1 - Input parameters for molecular dynamics models.

To track the erosion rate of the substrate, a cut-off distance from the original surface was used. The cut-off was determined based on a multiple of the maximum bond distance as per the work of Yuan et al. [12]. However, while the maximum bond distance of Ag-Ag bonding is approximately 3Å, it is important to also consider the potential for atomic oxygen adsorption and bonding onto the surface of the substrate due to high temperatures [13]. In this case, typical Ag-O bond length is approximately 2Å [13]. Therefore, the maximum distance from the substrate was calculated as twice the sum of the Ag-Ag and Ag-O bond length (i.e., 10Å). Similarly, for gold, the Au-Au and Au-O bond distances are approximately 3Å and 2Å, respectively [14-15]. Therefore, for both the silver and gold substrates, any

atoms separated by more than 10Å from the original surface could safely be considered as eroded from the surface. This value is similar to the 9Å cut-off used by Rahmani et al. to define erosion during atomic oxygen impact [16].

## Results and Discussion

### Erosion Yields

First, Figure 7.2 shows a snapshot of the silver substrate surface prior to any impacts and then during atomic oxygen impact. Prior to impacts, the lattice is arranged in an FCC structure. However, with continued impact, the damage can be observed throughout the depth of the slab (Figure 7.2). Moreover, as impact progresses, several silver atoms are separated from this lattice arrangement and are now beyond the predefined cut-off distance and are hence no longer bonded to the substrate. While many oxygen atoms have bounced off the surface, some are now bonded and are beginning to form an oxide layer (Figure 7.2C). Next, this cut-off was used to determine the number of eroded silver atoms as a function of atomic oxygen impacts (Figure 7.3). After the first 57 atomic oxygen impacts, the silver substrate had only one atom eroded from the substrate beyond the cut-off distance. However, after reaching this point, the last 43 atomic oxygen impacts caused a loss of a further 64 silver atoms from the substrate. Silver atoms were eroded as both metallic species and oxides. Therefore, there appears to be a critical energy value that, when reached, leads to a significant increase in erosion rate. In total, the impact of 100 oxygen atom lead to the loss of 66 silver atoms from the substrate and a sputtering rate of 0.65 Ag atoms/Oxygen atom or  $11.6 \times 10^{-23}$  grams of Ag/Oxygen atom.

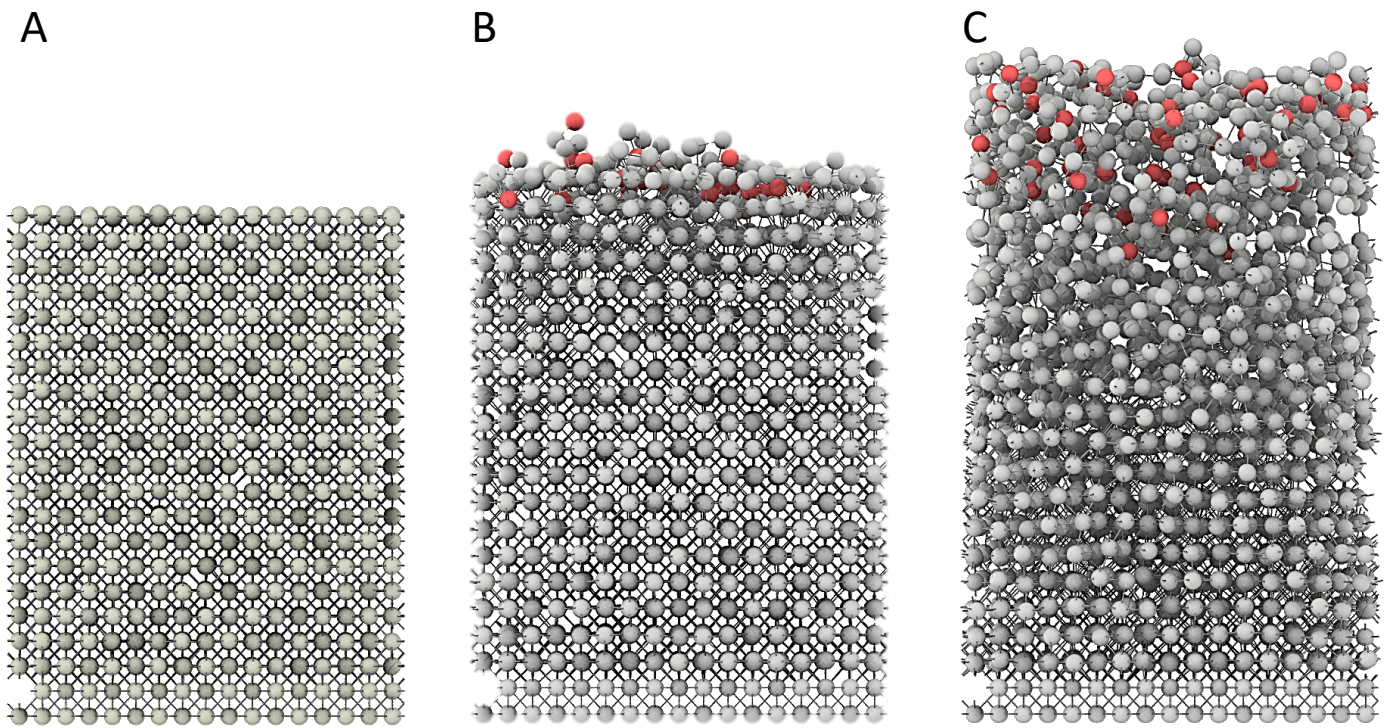


Figure 7.2 - Side view of silver lattice before impact (A), after 50 impacts (B) and after 100 oxygen impacts (C) where grey spheres are silver and red are oxygen. Eroded atoms have been removed.

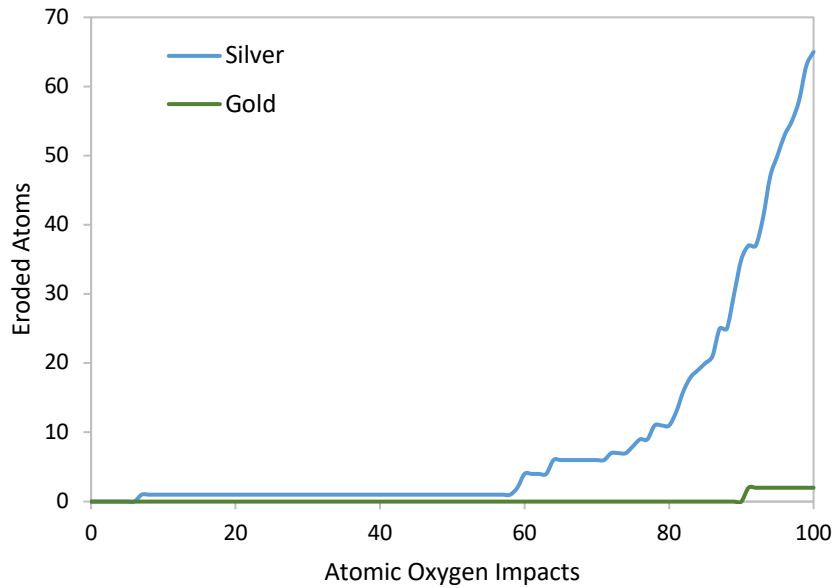


Figure 7.3 - Number of atoms eroded from surface as a function of atomic oxygen impact for Silver and Gold

Overall, research agrees that the reaction of atomic oxygen with silver is quite high, especially compared with other metals. The main reason for the discrepancies amongst metals lies in the properties of the metal oxides being formed [17]. For example, the free energy of oxide formation can be used to predict the energy required to break the bonds of the oxide. Those metals with low free energy of oxide formation are more likely to sputter faster due to the cyclic process of oxide break-up and reformation. Silver has a free energy of formation of 0.32 eV, whereas metals like iron and nickel are 2.79 and 2.53, respectively [17]. Therefore, silver oxides are much more likely to break up and sputter. Compounding this low free energy of formation, silver oxides have a high tendency for spalling from the silver substrate, meaning the oxide is not stable or protective from further atomic oxygen erosion [17]. Moreover, at the end of the simulation, several of the silver atoms that have eroded from the surface appear to be bonded with oxygen atoms, likely demonstrating the initial spalling of the oxide

later. As a result, while silver is a crucial metal for several spacecraft mechanisms, constant monitoring, short flight durations, or coatings must be used.

To compare the simulation results with experimental results, erosion yield observations from flight tests of silver in LEO were considered. Referring to Banks et al. [3], the erosion yield for silver was measured to be  $10.5 \times 10^{-24} \text{ cm}^3/\text{oxygen atom}$ . For comparisons sake, this value was converted to a mass loss per oxygen atom by multiplying by the density of silver ( $11 \times 10^{-23} \text{ cm}^3/\text{atom}$ ). Overall, the silver erosion rate predicted by the molecular dynamics model agreed extremely well with experimental data ( $11.6 \times 10^{-23} \text{ g/oxygen atom}$  and  $11 \times 10^{-23} \text{ cm}^3/\text{oxygen atom}$ , respectively). However, while results were accurate with silver, it is important to test other common metals used in the LEO environment before any conclusions can be drawn about this method. Therefore, in addition to the silver substrate, a gold substrate was also simulated.

Gold is one of the most commonly used spacecraft materials due to its resistance to corrosion and atomic oxygen erosion. For example, many materials, including silver, are coated in thin gold coatings to shield them from the harsh space environment [17]. Similar to the silver test, a gold substrate was impacted with 1 atomic oxygen every 400 time steps with a  $10\text{\AA}$  cut-off as described above (Figure 7.4). In contrast to silver, there is significantly less damage to the lattice and only 1 gold atom is lost after the first 60 atomic oxygen impacts (Figure 7.4). Moreover, with continued impact the erosion rate does not increase and ultimately only 2 gold atoms are lost after 100 atomic oxygen impacts; corresponding to a sputtering rate of 0.05 gold atoms per oxygen atom (Figure 3). Therefore, gold is significantly less reactive when impacted with atomic oxygen and should make for a viable coating for exposed surfaces in LEO. In addition, this low value corresponds well with experimental

values that do not observe degradation and helps to verify the accuracy of the simulation method [3-4]. Therefore, based on models of silver and gold, two prominent spacecraft metals, molecular dynamics simulations of atomic oxygen impacts are able to accurately predict experimental erosion values for metals.

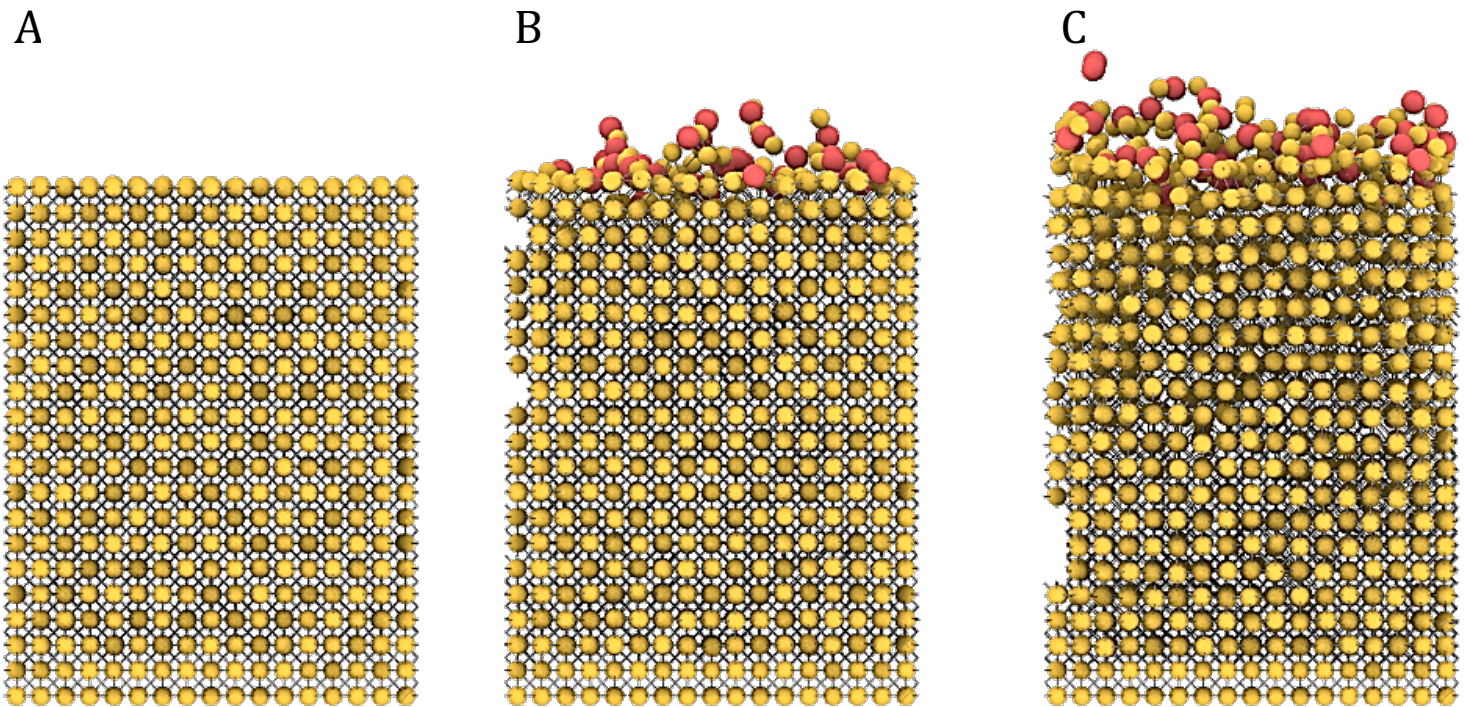


Figure 7.4 - Side view of gold lattice before impact (A), after 50 impacts (B) and after 100 oxygen impacts (C) where gold spheres are gold and red are oxygen. Eroded atoms have been removed.

## Temperature and Heat Transfer Effects during Impact

While the above section looked only at the rate of erosion of the substrate, the temperature growth of the substrate sheds potential light on the mechanisms at play during the erosion. Prior to atomic oxygen impact, both the silver and gold substrates were equilibrated to 200K to mimic space conditions. During impact, thermostats were removed and the substrate was allowed to heat up during impact. First, referring to Figure 7.5, it can be seen that with increasing atomic oxygen impact the remaining substrate temperature of both silver and gold increase dramatically. Moreover, silver, which had the significantly higher erosion coefficient, also reached a much higher final substrate temperature than gold (1700K and 1000K, respectively). While both metals followed a linear trend of increasing temperature with atomic oxygen impact, there was a large temperature spike for silver at approximately 60 atomic oxygen impacts. In addition, when plotting both temperature and erosion of the remaining substrate on the same figure, it can be seen that the temperature spike corresponds to the beginning of the erosion of the substrate (Figure 7.6). Therefore, this supports the conclusion that once an energy barrier is broken erosion becomes more prevalent.

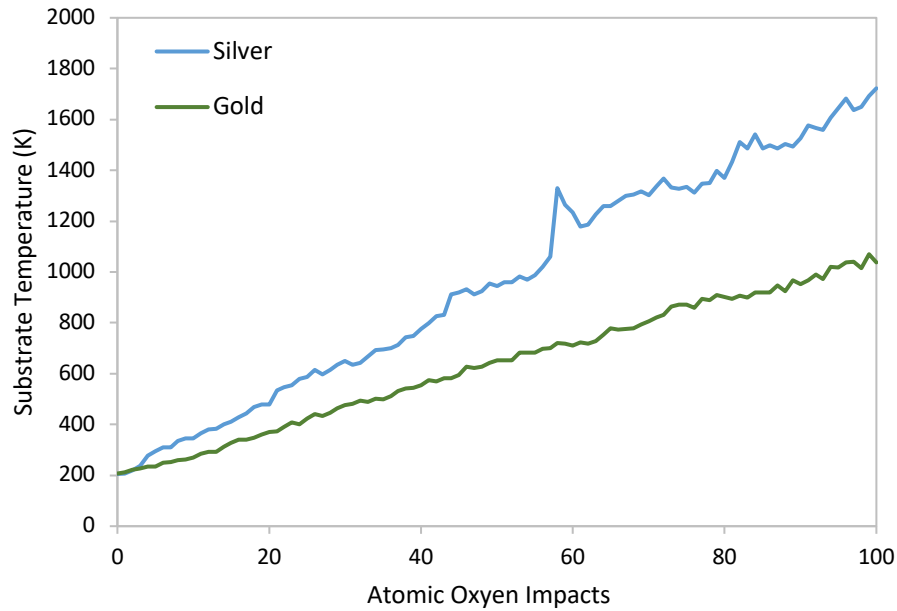


Figure 7.5 - Substrate temperature for gold and silver as a function of atomic oxygen impacts

In a similar study on the impact of atomic oxygen with spacecraft polymers, Zeng et al. concluded that the effect of the atomic oxygen was two-fold [7]. First, initial atomic oxygen simply impart energy into the system due to their high kinetic energy. Next, the study posited that once some substrate atoms have been freed, the remaining oxygen atoms are more reactive with the substrate and more likely to form oxides, thus causing a rapid increase in erosion rate [7]. The results of this study appear to agree with these findings. Initial erosion is low but substrate temperature is increasing, likely indicating the heat transfer due to kinetic energy. Once some erosion occurs, erosion rate then increases rapidly to the presence of freed and reactive substrate atoms.

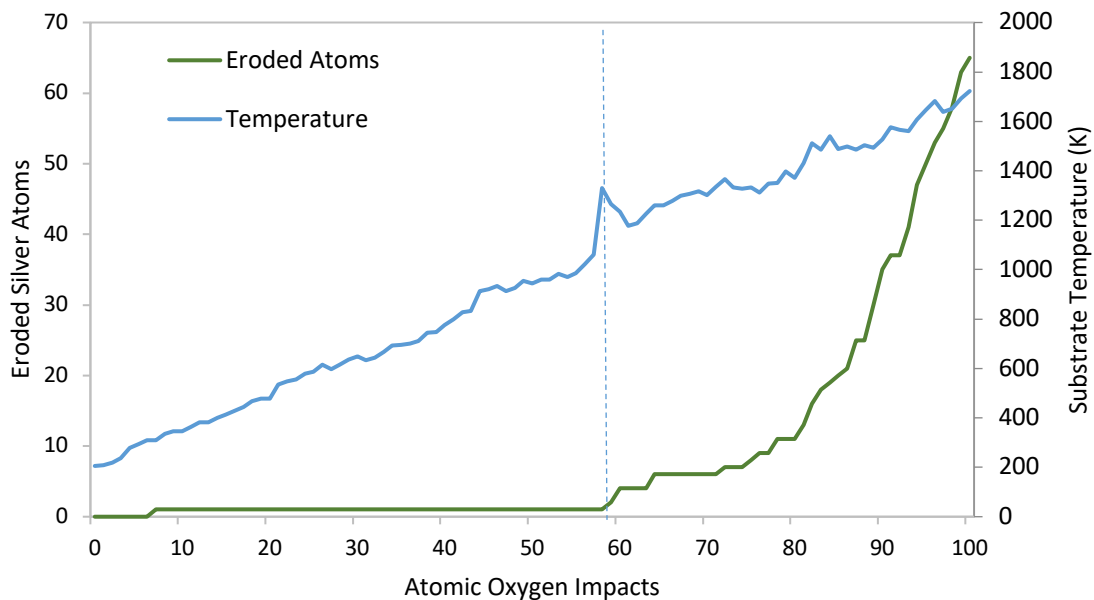


Figure 7.6 - Combined plot of number of eroded silver atoms and substrate temperature as a function of atomic oxygen impacts.

Similar to the findings of Zeng et al., Rahnamoun and van Duin also observed an important relationship between substrate temperature and erosion of the substrate. In this study, substrate erosion increased rapidly with temperature and it was concluded that an energy barrier should be reached before erosion would dominate [9]. Moreover, to clearly demonstrate the importance of substrate temperature on erosion yields, the study compared erosion yields when a thermostat was maintained on the substrate. In this study, no erosion was observed when the substrate was forced to at 200K [9]. Therefore, to compare results, a weakly coupled thermostat was placed on the silver substrate after equilibration to 200K and it was then impacted with atomic oxygen. Similar to the findings of Rahnamoun and van Duin, when the temperature of the substrate is fixed to 200K, no erosion is

observed (Figure 7.7). Therefore, following the trend previously observed for polymers, the temperature rise in the initial stages of atomic oxygen impact is critical to the subsequent erosion process of metals.

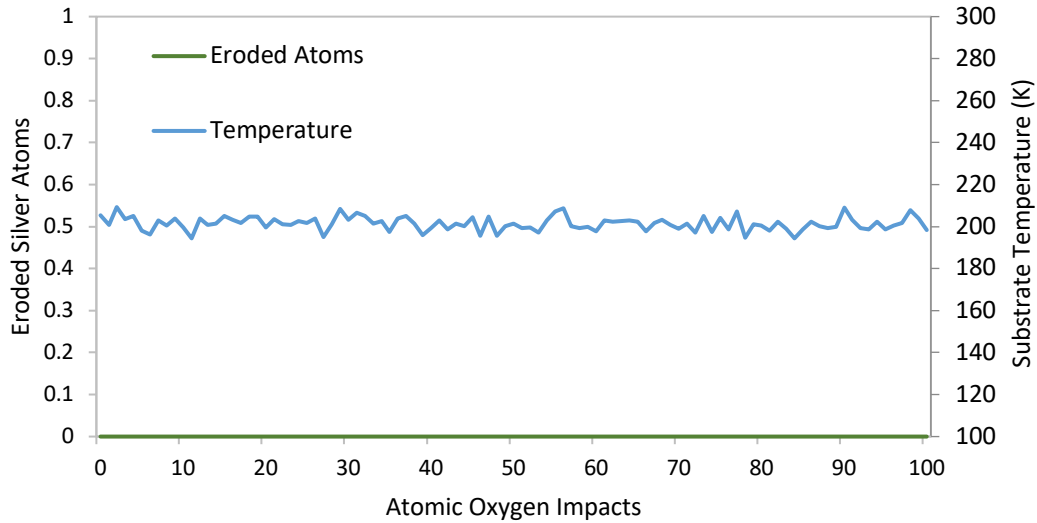


Figure 7.7 - Combined plot of number of eroded silver atoms and substrate temperature when NVE thermostat is applied to substrate

## Conclusion

In summary, this study utilized the ReaxFF force field to simulate atomic oxygen impact on spacecraft metals in the LEO environment. While research has shown that these methods are accurate for polymers, due to the different crystal structure of metals and the necessity for changing the potential, it is important to also test the accuracy with spacecraft metals. Results demonstrated that impacting a silver substrate with 100 atomic oxygen atoms resulted in a breakup of the metal and an erosion coefficient that matched data from LEO. Moreover, when the same method was tested for gold, a material significantly less reactive to atomic oxygen, very little erosion was observed, agreeing with previously reported data. Therefore, this paper successfully demonstrated the ability for molecular dynamics models to accurately predict atomic oxygen erosion of metals in the LEO environment. These findings demonstrate that the performance of metals in LEO can be simulated using molecular dynamics

as opposed to traditional high-cost space environment tests. Therefore, as new metals and materials are developed, performance in the LEO environment can easily be checked prior to further space testing. Moreover, as missions move to deeper space where in-situ testing is extremely difficult and where even higher energy impacts occur, the potential for molecular dynamics to simulate these complex environments cannot be ignored.

## References

- [1] Banks, B. A., Rutledge, S. K., Brady, J. A., and Merrow, J. E., 1989, "Atomic Oxygen Effects on Materials."
- [2] Zhang, J., and Minton, T. K., 2001, "Production of Volatile CO and CO<sub>2</sub> from Oxidized Polyethylene and Graphite Surfaces by Hyperthermal Atom-Surface Collisions," *High Perform. Polym.*, **13**(3), pp. S467–S482.
- [3] Banks, B. A., Rutledge, S. K., Paulsen, P. E., and Steuber, T. J., 1989, "Simulation of the Low Earth Orbital Atomic Oxygen Interaction with Materials by Means of an Oxygen Ion Beam."
- [4] Samwel, S. W., 2014, "Low Earth Orbital Atomic Oxygen Erosion Effect on Spacecraft Materials," *Sp. Res. J.*, **7**(1), pp. 1–13.
- [5] Harrison Jr, D. E., Levy, N. S., Johnson III, J. P., and Effron, H. M., 1968, "Computer Simulation of Sputtering," *J. Appl. Phys.*, **39**(8), pp. 3742–3761.
- [6] Rahnamoun, A., and Van Duin, A. C. T., 2014, "Reactive Molecular Dynamics Simulation on the Disintegration of Kapton, POSS Polyimide, Amorphous Silica, and Teflon during Atomic Oxygen Impact Using the Reaxff Reactive Force-Field Method," *J. Phys. Chem. A*, **118**(15), pp. 2780–2787.
- [7] Zeng, F., Peng, C., Liu, Y., and Qu, J., 2015, "Reactive Molecular Dynamics Simulations on the Disintegration of PVDF, FP-POSS, and Their Composite during Atomic Oxygen Impact," *J. Phys. Chem. A*, **119**(30), pp. 8359–8368.
- [8] Srama, R., Ahrens, T. J., Altobelli, N., Auer, S., Bradley, J. G., Burton, M., Dikarev, V. V., Economou, T., Fechtig, H., Gv̇drlich, M., Grande, M., Graps, A., Gṙvn, E., Havnes, O., Helfert, S., Horanyi, M., Igenbergs, E., Jessberger, E. K., Johnson, T. V, Kempf, S., Krivov, A. V, Kṙger, H., Mocker-Ahlreep, A., Moragas-Klostermeyer, G., Lamy, P., Landgraf, M., Linkert, D., Linkert, G., Lura, F., McDonnell, J. A. M., Ṁhlmann, D., Morfill, G. E., Ṁller, M., Roy, M., Scḣfer, G., Schlotzhauer, G., Schwehm, G. H., Spahn, F., Sṫbig, M., Svestka, J., Tschernjowski, V., Tuzzolino, A. J., Ẇsch, R., and Zook, H. A., 2004, "The Cassini Cosmic Dust Analyzer," *The Cassini-Huygens Mission: Orbiter In Situ Investigations Volume 2*, C.T. Russell, ed., Springer Netherlands, Dordrecht, pp. 465–518.
- [9] Van Duin, A. C. T., Dasgupta, S., Lorant, F., and Goddard, W. A., 2001, "ReaxFF: A Reactive Force Field for Hydrocarbons," *J. Phys. Chem. A*, **105**(41), pp. 9396–9409.
- [10] Lloyd, A., Cornil, D., Van Duin, A. C. T., van Duin, D., Smith, R., Kenny, S. D., Cornil, J., and Beljonne, D., 2016, "Development of a ReaxFF Potential for Ag/Zn/O and Application to Ag

- Deposition on ZnO,” *Surf. Sci.*, **645**, pp. 67–73.
- [11] Joshi, K., van Duin, A. C. T., and Jacob, T., 2010, “Development of a ReaxFF Description of Gold Oxides and Initial Application to Cold Welding of Partially Oxidized Gold Surfaces,” *J. Mater. Chem.*, **20**(46), pp. 10431–10437.
- [12] Yuan, B., Zeng, F., Peng, C., and Wang, Y., 2018, “A Reactive Molecular Dynamics Simulation Study to the Disintegration of PVDF and Its Composite under the Impact of a Single Silicon-Oxygen Cluster,” *Comput. Mater. Sci.*, **154**, pp. 14–24.
- [13] Trushin, E. V., and Zilberberg, I. L., 2013, “Anion-Radical Oxygen Centers in Small (AgO)<sub>n</sub> Clusters: Density Functional Theory Predictions,” *Chem. Phys. Lett.*, **560**, pp. 37–41.
- [14] Shi, H., Asahi, R., and Stampfl, C., 2007, “Properties of the Gold Oxides Au<sub>2</sub>O<sub>3</sub> and Au<sub>2</sub>O: First-Principles Investigation,” *Phys. Rev. B*, **75**(20), p. 205125.
- [15] Miller, J. T., Kropf, A. J., Zha, Y., Regalbuto, J. R., Delannoy, L., Louis, C., Bus, E., and van Bokhoven, J. A., 2006, “The Effect of Gold Particle Size on AuAu Bond Length and Reactivity toward Oxygen in Supported Catalysts,” *J. Catal.*, **240**(2), pp. 222–234.
- [16] Rahmani, F., Nouranian, S., Li, X., and Al-Ostaz, A., 2017, “Reactive Molecular Simulation of the Damage Mitigation Efficacy of POSS-, Graphene-, and Carbon Nanotube-Loaded Polyimide Coatings Exposed to Atomic Oxygen Bombardment,” *ACS Appl. Mater. Interfaces*, **9**(14), pp. 12802–12811.
- [17] De Rooy, A., 1985, “The Degradation of Metal Surfaces by Atomic Oxygen,” *Proceedings of the 3rd European Symposium on Spacecraft Materials in a Space Environment*, pp. 99–108.

## Chapter 8: The Effect of Atomic Oxygen Flux and Impact Energy on the Damage of Spacecraft Metals

### **Authors:**

**Liam S. Morrissey, Ali Rahnamoun, Sam Nakhla**

### **CRediT author statement:**

**Liam S. Morrissey:** conceptualization, methodology, software, formal analysis, investigation, writing – original draft, **Sam Nakhla:** validation, resources, writing – review and editing, supervision, **Ali Rahnamoun:** conceptualization, formal analysis, writing – review and editing

**Published: Morrissey, Liam S.,** Ali Rahnamoun, and Sam Nakhla. "The Effect of Atomic Oxygen Flux and Impact Energy on the Damage of Spacecraft Metals." *Advances in Space Research* (2020).

## Abstract

High energy atomic impacts represent one of the biggest threats to material performance in both the low earth orbit (LEO) and deep space environment. However, while significant test data exists for LEO atomic oxygen (AO) collisions, further research is needed on the effect of high energy collisions that can potentially occur in deeper space. As such, this study investigated using the ReaxFF force field in molecular dynamics to simulate the impact of atomic oxygen on two common spacecraft metals, silver and aluminum. This study used a Wigner-Seitz defect analysis to track the damage evolution of the remaining substrate during impact. Results indicated that for both silver and aluminum the number of defects and depth of damage increased linearly with impact energy. While silver was shown to have a higher erosion yield than aluminum, its substrate formed less defects at all impact energies considered. The source of this discrepancy was attributed to the lower energy needed to form vacancies in aluminum as compared to silver. Our results show that while erosion is certainly an important parameter in measuring the damage to a material by high energy impacts, it is not sufficient to describe the amount of damage and state of the remaining substrate. Overall, this study demonstrates the potential for molecular dynamics simulations to be used to compare material performance and degradation in harsh deep space environments where testing may not be possible.

## Introduction

As missions continue to move to deeper space there is a pressing need to better understand the performance of the materials that will take us there. One of the biggest threats to these spacecraft materials is high energy atomic impacts. For example, in the low Earth orbit (LEO) atomic oxygen (AO) impacts represent a significant source of erosion and performance degradation [1]. These impacts can reach energies of 4.5 eV and, depending on the material, can lead to material loss and reduced performance [2]. Significant in-situ testing and simulations have been performed to better understand the effect of AO oxygen collisions in the LEO [1]. The results of these studies have allowed scientists to better understand how a material performs and which materials are most suitable for LEO exposure. However, while the LEO has received fairly exhaustive research, as these materials move even deeper into space they can be subjected to significantly higher energy collisions with both cosmic dust and the atomic interstellar medium. For example, the Cassini-Huygens Cosmic Dust Analyzer has detected nanoscale dust particles at speeds higher than 200 km/s [3]. While impacts with these dust particles would likely be catastrophic and not relevant for atomistic simulations, in addition to nanoscale dust, impacts with high speed interplanetary/interstellar atomic gases may also hinder performance [4]. Hoang et al. [5] considered the interaction of relativistic spacecrafts with the interstellar medium. The study attempted to quantify the potential effects of collisions with both interstellar gas using theoretical predictions. Findings indicated that atomistic gas bombardment could result in macroscale surface damages for a quartz material traversing a gas column at 0.2 the speed of light. As a result, while many spacecraft materials may be assumed to be non reactive with AO and thus suitable for the LEO, there may exist an energy barrier that could be overcome with a harsh enough environment. In other words, suitability in the LEO does not guarantee performance with higher energy collisions. However, unlike the LEO environment, materials cannot be easily tested in-situ and simulating the conditions in a laboratory

environment is both costly and extremely complex. As such, there is a need for more feasible methods of simulating and comparing the performance of materials in these extremely harsh environments.

One alternative to traditional testing methods is the use of the molecular dynamics (MD) technique to simulate the atomistic impacts on various substrates. Depending on the force field used, these simulations are capable of effectively modelling the bond breaking, temperature evolution, and damage of the substrate as impacts and chemical reactions occur. Therefore, these simulations offer the unique ability to view the evolution of the substrate during impact, as opposed to simply tracking its surface erosion after the impacts have occurred. Recently, MD has been used to simulate the performance of both polymers and metals in the LEO orbit. Rahnamoun and van Duin [6] used the ReaxFF force field to study the effect of AO on Kapton, POSS polyamide, and amorphous silica. During impact the simulations tracked the mass loss and temperature growth. Further, the predicted erosion coefficient agreed closely with previously reported experimental values. Similar to this work, Zeng et al. [7] used MD to study the disintegration of Polyvinylidene fluoride or polyvinylidene difluoride (PVDF) and fluoropropyl polyhedral oligomeric silsesquioxanes (FP-POSS), two common spacecraft polymers. Results showed that the FP-POSS performed better under AO impact and was immune until a certain number of impacts. Building on this work, Morrissey et al. [8] used MD to simulate the erosion yield of silver and gold; two commonly used spacecraft metals. Predicted erosion yields closely matched test data and results indicated that substrate temperature evolution was critical to subsequent erosion. However, while these studies clearly show the promising potential of using MD to model the effect of high energy impacts, findings were limited to energies found in the LEO. Therefore, these studies did not attempt to understand the effect of impact energy on the substrate. Moreover, findings typically only report the erosion yield and often do not consider the effect collisions may have on the remaining substrate. With increased impact is the non-eroded substrate damaged? How does this damage evolve

with increasing impact energy? Unlike traditional testing which occurs on the macroscale, MD simulations occur on the atomistic scale and should be able to answer these important questions. Further, understanding the effects of impact energy on damage is crucial to material selection for future deep space missions.

## Purpose

As can be seen from the above review, future deep space missions are likely to encounter higher energy atomistic collisions. Therefore, there is a pressing need to understand the performance of materials subjected to these environments. Materials that are considered 'immune' to AO erosion in the LEO will need to be tested again with these higher impact collisions. Previous research on AO impact simulations has shown strong accuracy with field and laboratory erosion rates [6]-[8]. While the erosion rate is an important value to consider, it does not provide an insight into the state of the substrate. As a result, the purpose of this study was to use molecular dynamics to track the damage evolution of various metal substrates during AO impact as a function of impact energy and dosage. Unlike previous simulations which focused solely on erosion yields from LEO conditions, this study tracked the microstructure damage by computing the number of defect atoms using a Wigner-Seitz defect analysis. Substrate damage was then modelled as both a function of impact dose, slab temperature, and impact energy. This allows for a more detailed discussion on the effect of high energy impacts on the microstructure of space metals.

## Methodology

### Molecular Dynamics and Force Field Selection

MD simulates the movement of atoms and molecules within a body. Simulations begin with the initial positions and velocities of all atoms within the system. An interatomic potential is then used to

define forces between interacting particles and thus calculate the atomic accelerations. Finally, Newton's equations of motion are then used to predict the next set of positions and velocities incremented by a prescribed timestep. AO simulations require a force field that can describe the bond breaking and formation during repeated impacts. However, traditional force fields are not applicable as they do not consider the breakage of bonds or reactions. In contrast, the reactive force field (ReaxFF) is a bond order based force field method that allows for the dynamic simulation of bond breaking and reformation in a body [9].

A typical ReaxFF force field calculates the energy of the system as a combination of the partial energy contributions from the bond, over- and under-coordination, lone pair, valence, torsion, van der Waals, and Coulomb energy [9] (Equation 1):

$$E_{system} = E_{bond} + E_{over} + E_{under} + E_{lp} + E_{val} + E_{tor} + E_{vdWaals} + E_{Coulomb} \quad (1)$$

Bond order is then used to determine the interactions between all atoms in the system. The bond order accounts for contributions from sigma, pi, and double pi-bonds as a continuous function of the distance between atoms via equation 2:

$$BO_{ij}^i = BO_{ij}^\sigma + BO_{ij}^\pi + BO_{ij}^{\pi\pi} \quad (2)$$

What makes ReaxFF unique is its ability to model interactions that are both connected and non-bonded. First, connectivity dependant reactions (valence and torsion energy) are modelled such that when bonds are broken their energy is eliminated. Second, non-bonded interactions, van der Waals and

Coulomb, are calculated regardless of connectivity between every atom pair in the set up. As a result of this combination, ReaxFF is able to describe both covalent and metallic systems. More detail on the ReaxFF method can be found in van Duin et al. [9].

For the current study atomic oxygen impacts on silver were modeled using the force field developed by Lloyd et al. [10] to describe the interaction of silver on zinc oxide surfaced. The force field was shown to reproduce equations of state for silver and silver oxides. Further, this potential was previously used to simulate the impact of AO in the LEO and accurately predicted the erosion coefficient as compared to experimental data in the LEO. Atomic oxygen impacts on Aluminum were modeled using the force field developed by Hong and van Duin [11]. This force field was developed to describe the effect of carbon coating on the oxidation of aluminum nanoparticles. Al-O interactions in this force field were adopted from a previous study that used the ReaxFF method to simulate the effect of temperature on the oxidation of aluminum. The force field was shown to accurately simulate the oxidation process and limiting thickness of the oxide layer agreed with experimental results.

### Atomic Oxygen Simulation Model

First, a  $60 \text{ \AA} \times 60 \text{ \AA} \times 40 \text{ \AA}$  (x, y, z) slab of pure aluminum and silver was developed containing 8550 atoms each. After preparing the substrate each slab was placed in a simulation box that was  $100 \text{ \AA}$  high with fixed boundary conditions in the z direction and periodic in the x and y directions. These boundary conditions were used to create a slab with a free top surface (Fig 1). Next, the entire simulation box was equilibrated to 200K using a constant number of atoms, volume and temperature (NVT) thermostat for 2000 time steps (Fig 8.1).

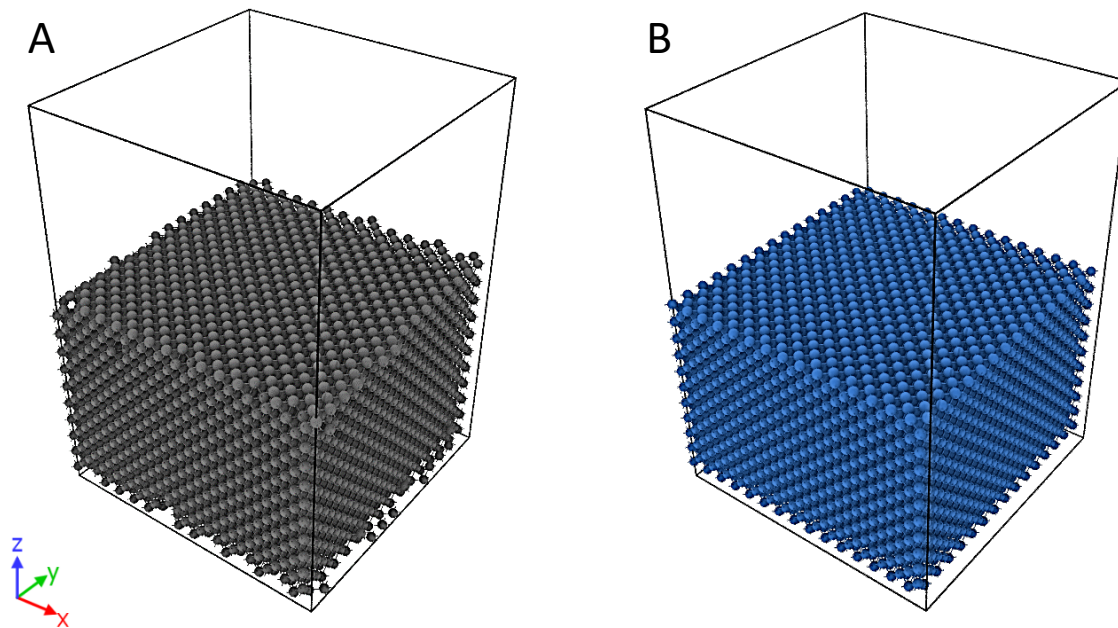


Figure 8.1 - Initial substrates of FCC silver (A) and FCC aluminum (B) in simulation box prior to impact

After the temperature settled to 200K it was then impacted with AOs. As per previous simulations [6], [8], 200 oxygen atoms were placed above the substrate (one every 100 fs) with a prescribed speed in the z direction and a randomly generated x and y position. Impacts were focused to occur in a  $30 \text{ \AA} \times 30 \text{ \AA}$  area centered on the top surface so as to avoid any edge effects or lost impact atoms. During impact the initial *NVT* thermostat was removed and two thermostat options were tested to determine their effect on the resulting substrate damage. First, similar to our previous MD simulations of the LEO, after equilibration the *NVT* thermostat was removed and an *NVE* (constant number, volume and energy) simulation was run that fixed the volume while allowing the temperature to increase during impacts. While this simulation method is commonly used, it ignores the fact that due to the scale of these simulations on the macroscale there would be a large region surrounding the

impact zone that would act as a bath and dissipate some of the increased energy. This concept has been employed in several irradiation simulations that attempt to track the temperature evolution and damage cascade due to the impact of one high energy primary knock-on (PKA) atom [12]-[15]. While AO impacts simulate more than one impact, the concept is quite similar: high energy particles impacting a substrate and potentially causing damage. As such, simulations were also run by fixing an outer 0.2 lattice unit thick layer of atoms around the edges of the substrate to 200K using an *NVT* thermostat. These layers acted as a bath to dissipate some of the temperature during impact. It is important to note that the top surface was not fixed to any temperature to ensure realistic heating of the free surface during impact. Overall, 200 atomic oxygen atoms were emitted over a total simulation time of 20 ps. As per table 8.1, to track the effect of impact energy various impact speeds were used corresponding to energies between 4.5 eV (as seen in the LEO) and 30 eV. These energies were chosen to capture both LEO AO (4.5 eV) along with the higher speeds that can be seen in deep space [4] where oxygen is a constituent of the interstellar medium [5] and interstellar dust [3], [16].

Table 8.1 - Atomic oxygen impact energies and corresponding impact speeds tested

Impact Energy (eV)	Impact Speed (km/s)
4.5	1.81
10	2.71
20	3.83
30	4.6

## Damage Tracking

As opposed to erosion yields, which focus only on those surface atoms lost during simulation, the goal of this study was to consider how the remaining substrate is affected by these impacts. Similar to the work of Chen et al. [15], a Wigner-Seitz (WS) defect analysis was used to track the damage evolution during impact. The WS method works by considering a defect free reference state relative to a displaced/damaged configuration. Each atomic site in the reference state is a WS cell. At each time step cells are checked relative to the reference site. When a site no longer has any atomic occupancy it is deemed a vacancy and when a displaced atom occupies a new position between atoms it is considered an interstitial site. The total number of vacancies and interstitials during impact were then used to determine the damage of the substrate as a function of impact flux, energy, and thermostat.

In addition to tracking the number of defective atoms, a custom Python-based modifier was employed in the visualization software OVITO [17] to track the depth of defective atoms. Those sites that were undamaged, and thus with an occupancy of unity, were filtered out such that only damaged sites (vacancies and interstitials) were tracked. Next, the maximum depth in the z direction of all remaining defects was used to determine the depth of damage in the substrate as a function of impact energy. Therefore, this method allows for a true tracking of both the amount of damage and the extent to which this damage penetrates the substrate.

## Results

### Verification of Forcefields

Due to the harsh environment and high energies being considered one of challenges is a lack of experimental data for comparison. Unlike LEO simulations where experimental and field data are readily available, there is limited data for high energy AO collisions on metals as would be potentially seen in deep space. Therefore, care must be taken to first validate the force fields prior to use. Previous studies have shown that the force fields used in the current study were able to accurately predict erosion coefficients as compared to LEO data. However, there was no mention of defect formations. To address this gap in knowledge each force field was first tested for its ability to predict the vacancy formation energy. Given that the present damage definition is related to the number of vacancies and interstitials formed, accuracy is highly dependent on the vacancy formation energy. For each force field a separate simulation was run on the relevant substrate. A periodic cell with [100] orientations in the x, y, and z was first created and the initial energy of the system was computed. An atom was then removed from the structure and the system was relaxed using a conjugate gradient energy minimization method. The energy of the relaxed system with the vacancy was then used to determine the vacancy formation energy  $E_v^f$  via equation 3:

$$E_v^f = E_f - \left[ \frac{N_0 - 1}{N_0} \right] E_i \quad (3)$$

Where  $E_f$  is the energy of system with a vacancy,  $E_i$  is the initial energy of the system and  $N_0$  is the number of atoms in the system.

Table 8.2 - Predicted and experimental vacancy formation for silver and aluminum [18]

Material	Predicted Vacancy Formation Energy (eV)	Error to Experimental	Experimental Vacancy Formation Energy (eV)
Silver	1.206	11.6%	1.08
Aluminum	0.893	13%	0.79

Referring to table 8.2, for both the silver and aluminum substrates the vacancy formation energy was predicted with reasonable accuracy as compared to experimental values reported by Ogorodnikov et al. [18]. Therefore, given that damage is defined based on the number of vacancies and interstitials, the force fields were deemed suitable and accurate for the present simulations.

#### Effect of Impact Energy

First for the silver substrate with a bath layer, the number of defects in the substrate increased with number of impacts for all impact energies tested. For example, at a 4.5 eV impact energy there were 0.018 defects per atom after 200 impacts (Fig 8.2A). However, at an impact energy of 30 eV this damage increased to 0.15 defects per atom. Further, there was a linear increase ( $R_2 = 0.986$ ) in the number of defects after impact as a function of impact energy (Fig 8.3).

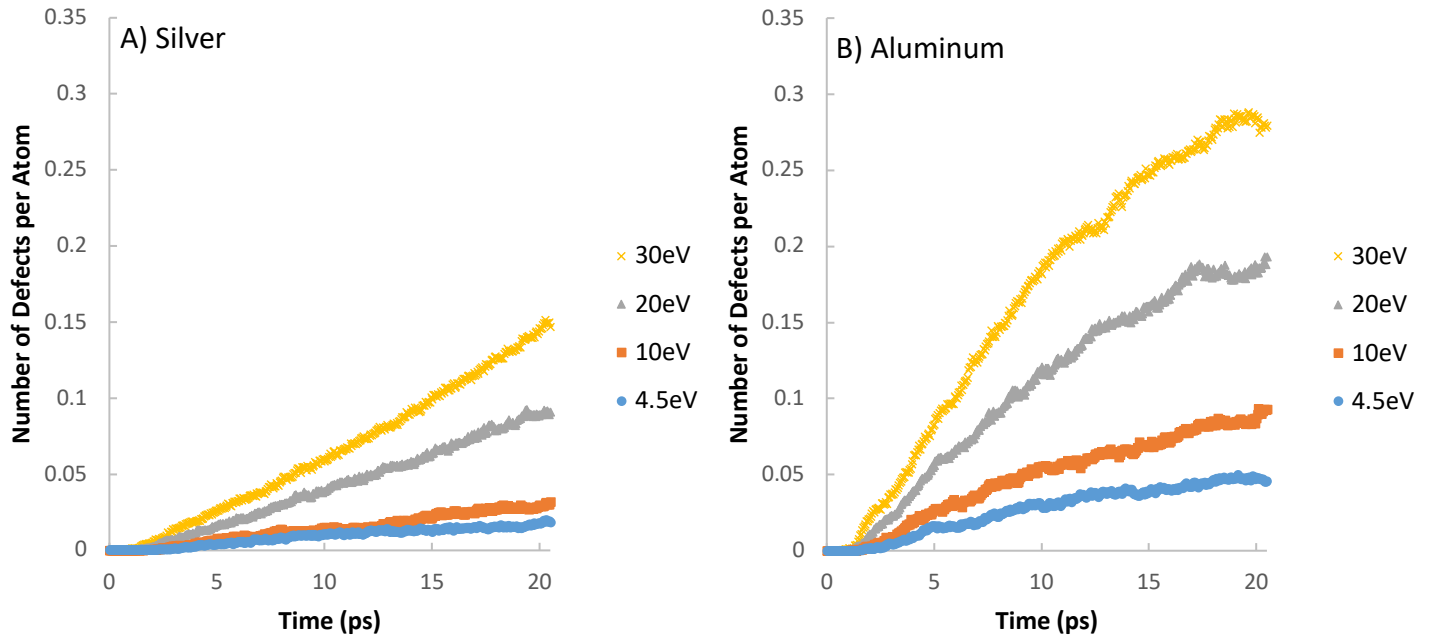


Figure 8.2 - Number of defects per atom in silver (A) and aluminum (B) as a function of time for various impact energies with a thin bath layer

Similarly, for the aluminum substrate with a thin bath layer the number of defects also increased with number of impacts and with increasing impact energy. At an impact energy of 30 eV there was 0.280 defects per atom, as compared to only 0.046 defects per atom at 4.5 eV (Fig 2B). Moreover, as with the silver substrate, there was a highly linear ( $R_2 = 0.999$ ) increase in the number of defects after impact as a function of impact energy (Fig 8.3).

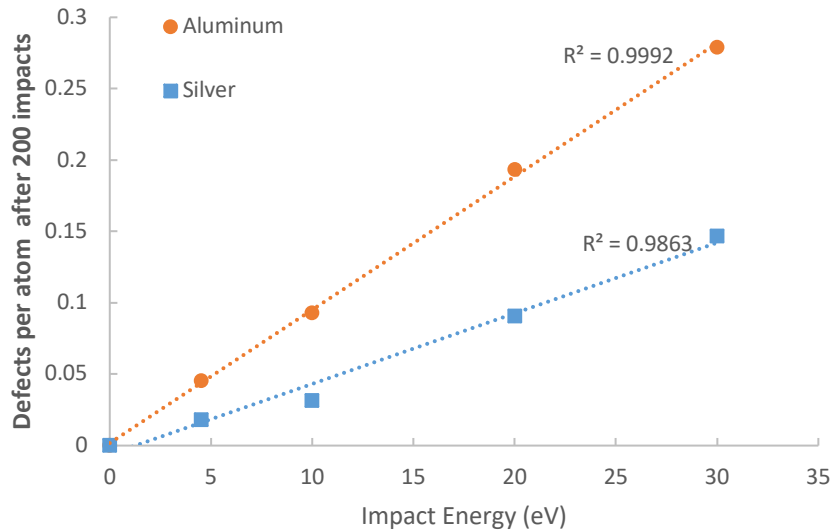


Figure 8.3 - Relationship between the number of defects per atom and impact energy for both silver and aluminum

#### Effect of Thermostat and Importance of Temperature

In addition to the case with a thin bath layer the simulations were also run with no temperature/pressure control on the substrate during impact. After equilibration the *NVT* thermostat was removed and the atoms were controlled use *NVE* time integration only, thus allowing temperature to increase with no outside control. In other words, temperatures are allowed to rise with no bath layer to dissipate. Fig 8.4 shows the evolution of defects as a function of time for the case of no thermostat on both the silver and aluminum. Similar to the bath case, for both silver and aluminum the number of defects increased with number of AO impacts. The increase remained linear but with more fluctuations in the number of defects per during impact. Fluctuations were more prevalent in lower energy collisions and are likely caused by rearrangements of the lattice and recombination of vacancy-interstitial pairs during impact as the temperature rises. Therefore, when a bath layer is employed the damage evolution is both more stable and linear.

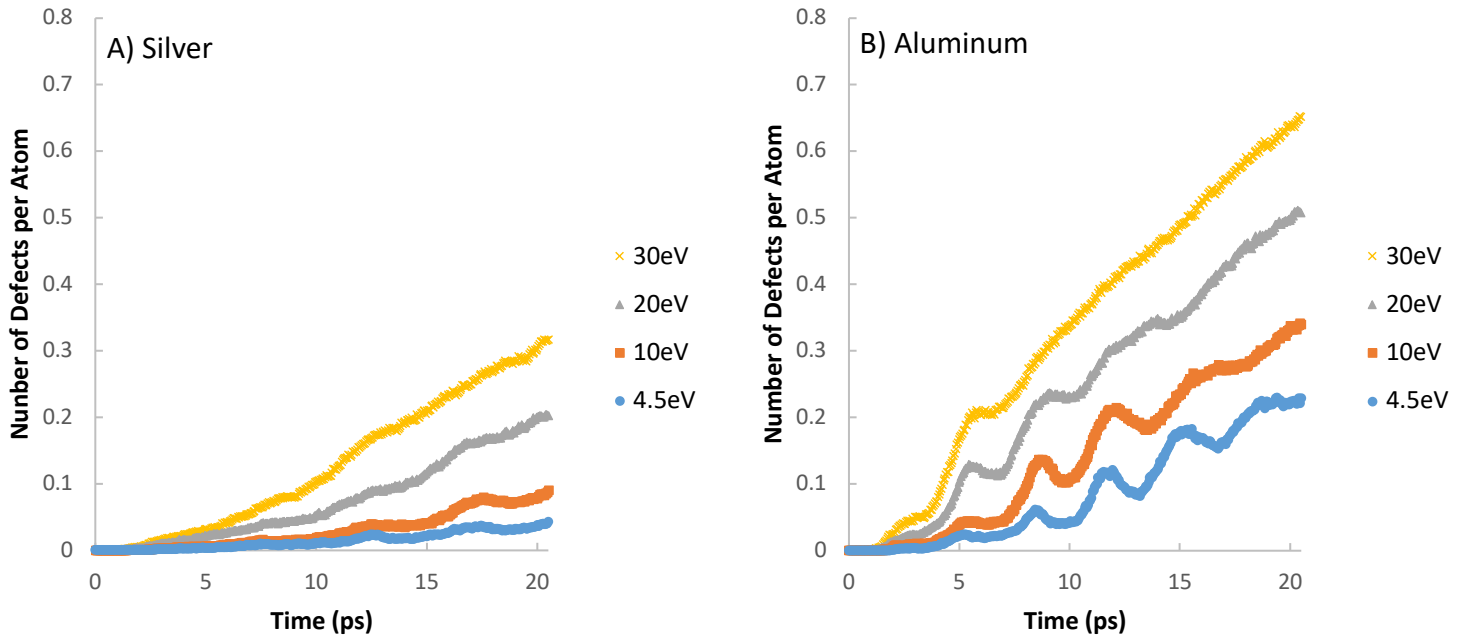


Figure 8.4 - Number of defects per atom for silver (A) and aluminum (B) as a function of time for various impact energies with no bath layer

Further, Fig 8.5 and Fig 8.6 shows the effect of the edge thermostat on the number of defects per atom for both substrates for each impact energy simulated (A-D). At each impact energy there is a time period where the two temperature methods are essentially overlapping. Eventually, with increasing time (and thus number of impacts), the simulations with no bath deviate away from the dominant linear bath case, demonstrating rapid increase. For example, after 200 impacts at 30eV energy the silver substrate with no bath had 0.316 defects per atom, which is over twice as many as when a thin bath layer is employed. Similarly, after 200 impacts at 30 eV energy the aluminum substrate had 0.652 defects per atom, again almost twice as many as when a thin bath layer is employed.

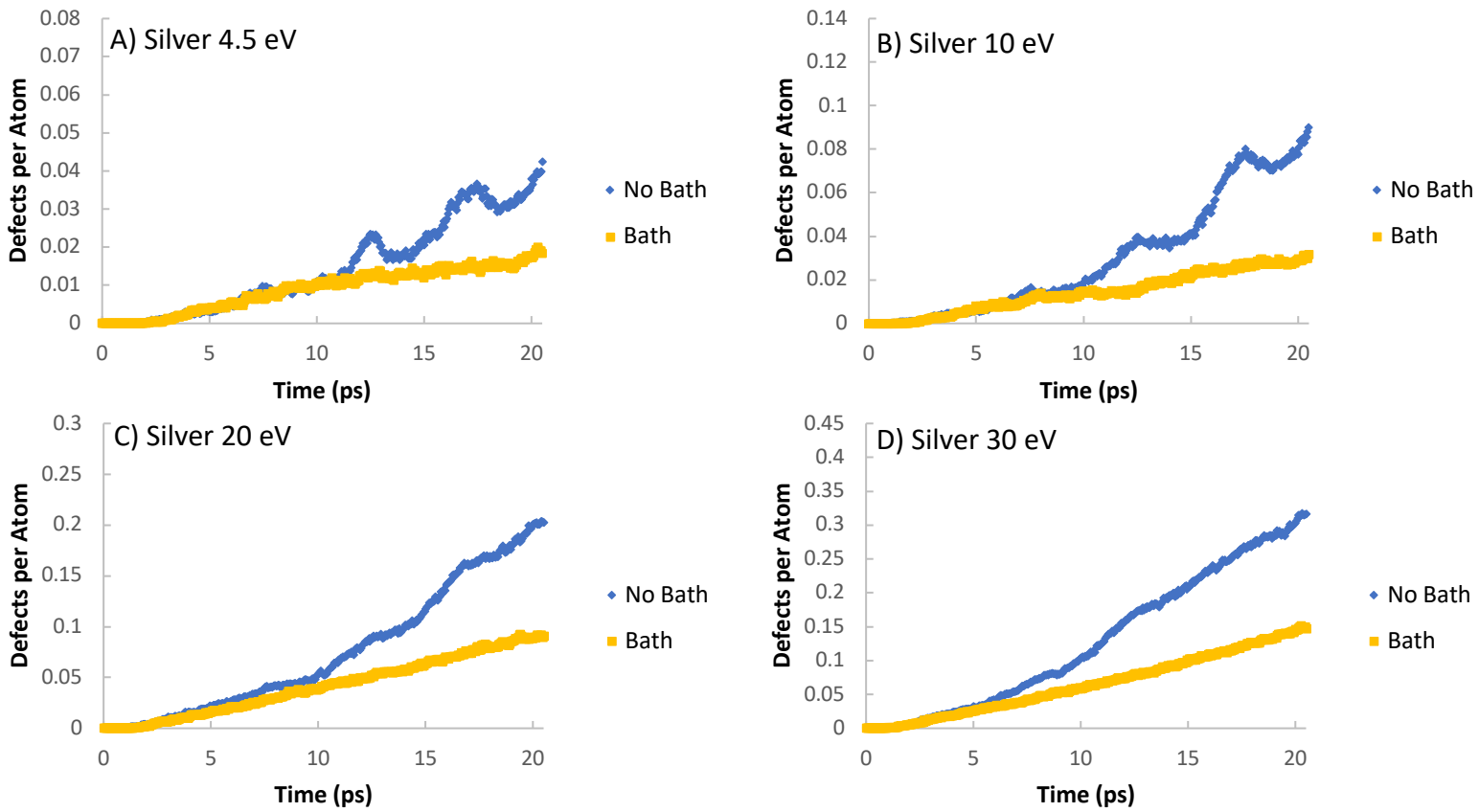


Figure 8.5 - Number of defects per atom in silver as a function of time for various impact energies (A-D)

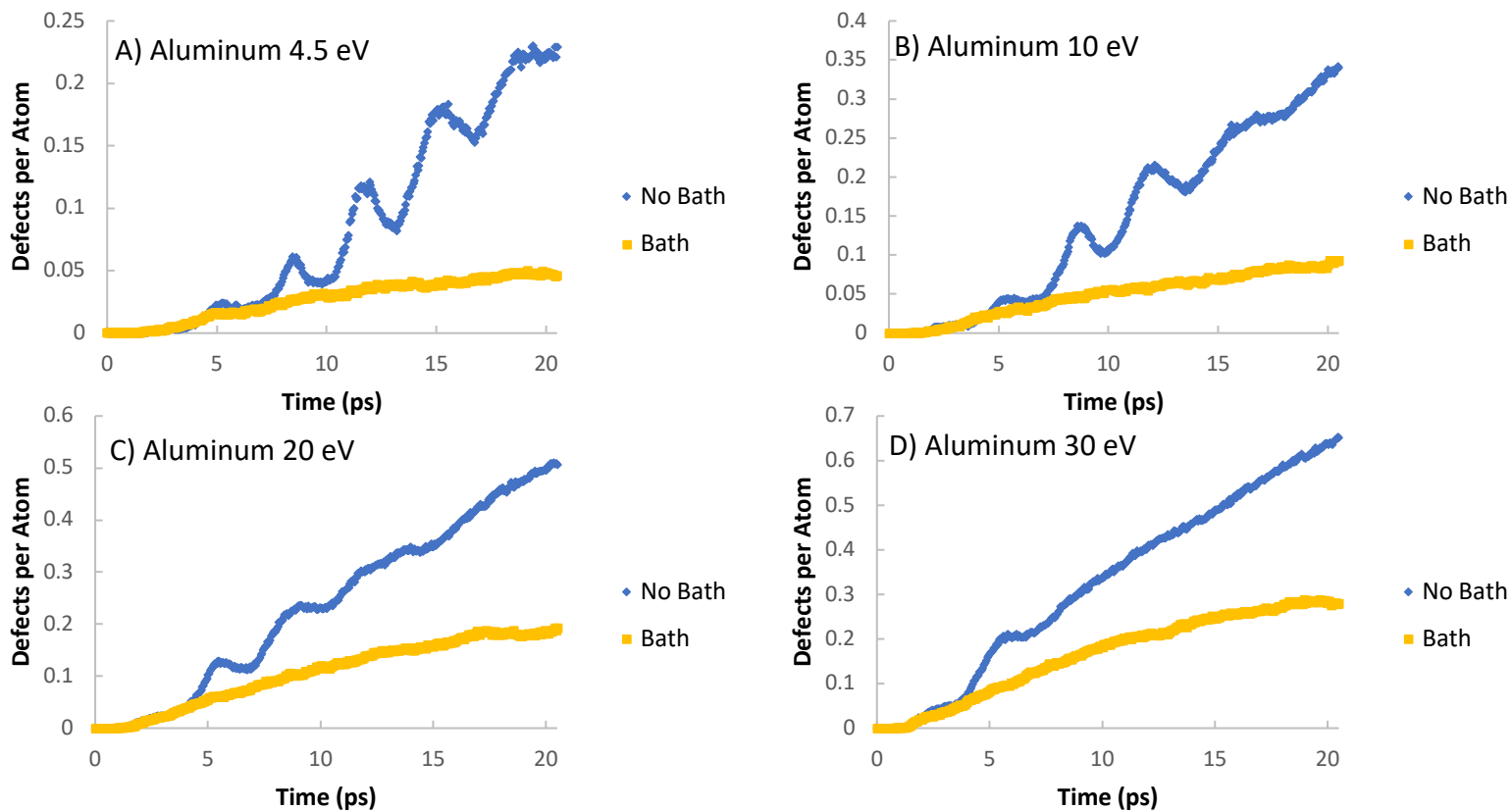


Figure 8.6 - Number of defects per atom in aluminum as a function of time for various impact energies (A-D)

The differences between the two substrates and thermostat methods are further highlighted by examining the temperature profiles during impact for all cases (Fig 8.7). First, when comparing the two substrates it can be seen that for both thermostat methods aluminum consistently had a higher temperature after impact as compared to silver. Therefore, aluminum had both a higher temperature and more damage at all cases as compared to silver. Similarly, when no bath control was used the aluminum and silver substrates reached a significantly higher temperature for all impact energies. For example, at 20 eV the temperature of the aluminum substrate with no bath was over twice as high as the case with a bath layer (1841K and 835K respectively). Therefore, the thermostat on the thin bath layer successfully simulated the expected temperature dissipation. Again, the case with no bath

reached a higher temperature and had more damage for both aluminum and silver at all impact energies tested. Therefore, these simulations demonstrate that the temperature of the substrate is an important indicator of potential damage. Overall, given the nanoscale nature of the periodic simulations a thin bath layer is likely a better representation of the temperature dissipation that would be found in an actual macroscale sample. Therefore, when using MD to study the erosion and damage caused by AO impacts thin bath layers should be employed to allow for realistic temperature evolution and dissipation.

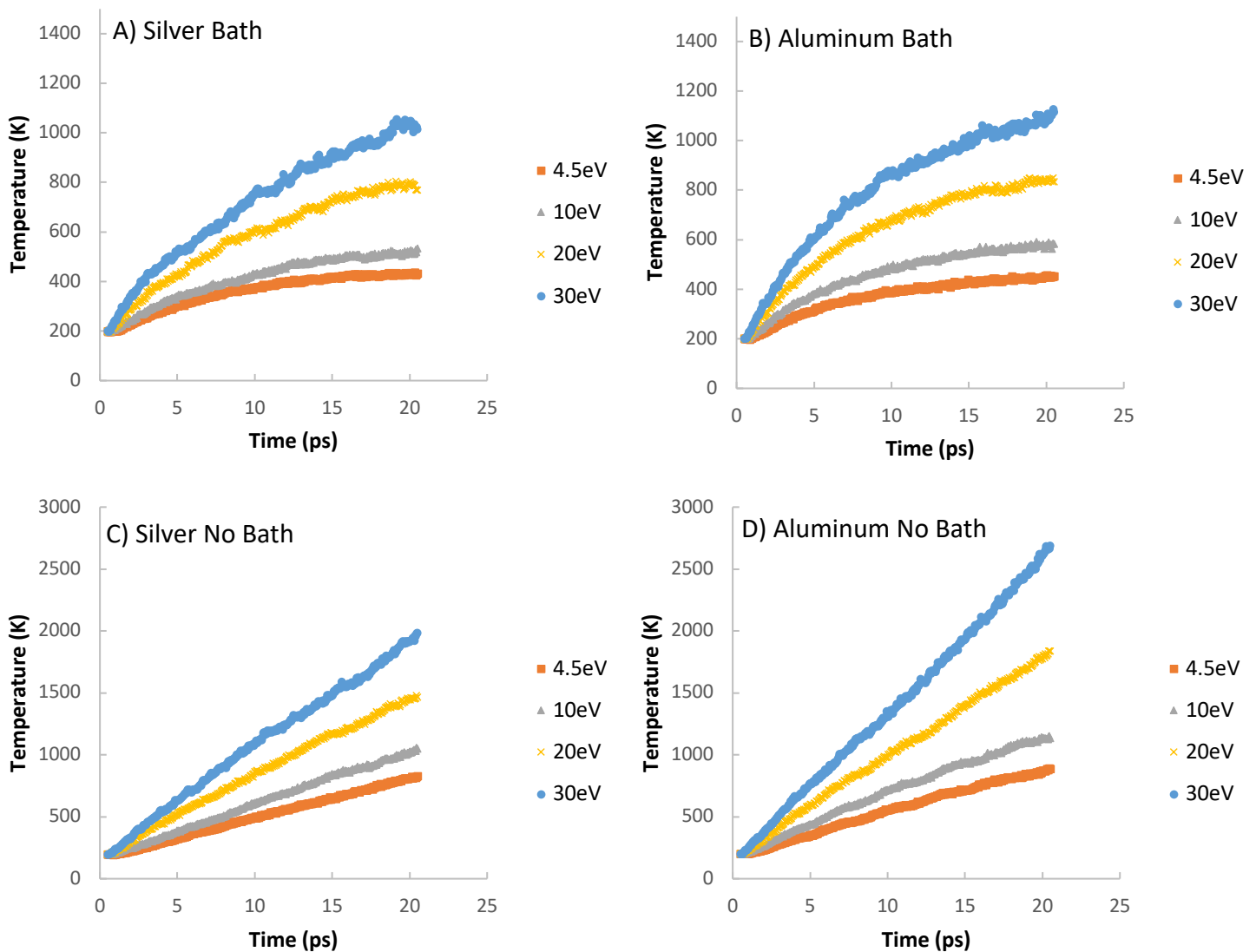


Figure 8.7 - Temperature profiles for aluminum and silver with (A,B) and without (C,D) a bath layer

## Comparison of Substrates: Damage and Erosion

After demonstrating the effect of impact energy and selecting the appropriate edge thermostat method the next question was to consider the reason behind the two metal substrates exhibiting different damage profiles. While experimental data is limited for the higher energy AO impacts considered in the present study, there is significant data for 4.5 eV collisions in the LEO. Results from these flight experiments have shown that aluminum is expected to have extremely limited erosion as compared to silver [1]. However, no consideration was given to the microstructure of the remaining substrate left after erosion had occurred. Similarly, results from 20 keV O<sub>2</sub> impact tests have again shown silver to have a much higher sputtering yield than aluminum (9.7 atoms per ion and 0.52 atoms per ion for silver and aluminum, respectively) [19]. Previous studies have postulated that the reason for different erosion rates lies in the cohesive energy (energy needed to separate two bonded atoms from each other) and the negative free energy of oxide formation (energy needed to break up the oxide layer) [20]. For example, aluminum has a cohesive energy of 3.41 eV and a negative free energy of oxide formation of 5.89 eV. Comparatively, silver has a cohesive energy of 2.94 eV and a negative free energy of oxide formation of 0.32 eV. In other words, less energy is needed to both separate silver atoms and break up potential oxide formation. Therefore, before considering the damage of the substrates, simulations were examined for their predicted erosion yields to ensure they captured the trends documented by previous studies. Referring to Table 8.3 and Fig 8.8, at all impact energies tested aluminum had less eroded atoms than the silver substrate, thus agreeing with the trend predicted by cohesive energy and free energy of oxide formation.

Table 8.3 - Number of eroded aluminum and silver atoms at various times as a function of impact energy using a thin bath layer

Time (ps)	4.5 eV		10 eV		20 eV		30 eV	
	Aluminum	Silver	Aluminum	Silver	Aluminum	Silver	Aluminum	Silver
5	0	0	0	0	0	1	1	5
10	0	0	0	1	0	3	2	9
15	0	1	0	1	0	6	4	21
20	0	1	0	2	0	11	6	31

However, while the force fields accurately predicted that silver would observe more erosion than aluminum, the results also clearly demonstrated a higher damage in the aluminum substrates. For example, for all energies after impact the aluminum substrate had almost twice as many defects. At first glance this may seem counterintuitive; aluminum observes less erosion than silver but undergoes more damage within the remaining substrate. However, similar to erosion yields which are correlated to cohesive energy, previous irradiation simulations have shown that the formation of defects is a function of the vacancy formation energy of the metal in question. For example, in an assessment of radiation performance of silicon (Si) and Germanium (Ge) Jiang et al. [21] concluded that the origin of different radiation responses was due to the different defect formation energies. Similarly, Lin et al. compared radiation damage in niobium (Nb), tungsten (W) and vanadium (V) at 10 keV. Results demonstrated that W had significantly less defect production as compared Nb and V. However, the vacancy formation energy in W was significantly higher than Nb and V; 9.5 eV as compared to 2.76 eV/2.51 eV. Lin et al. attributed the source of different damage behavior to the defect formation energies. Therefore, given that both potentials accurately predicted vacancy formation energies, and that the vacancy formation energy of aluminum is lower than silver, it follows that aluminum would have more defects than silver. These results highlight the importance of not confining the study to erosion yields when discussing the effect of high energy collisions. While erosion is certainly an important concept, it is not an indicator of

the damage present in the remaining substrate. As shown in the present results, the substrate that observed less erosion can in fact also have more damage.

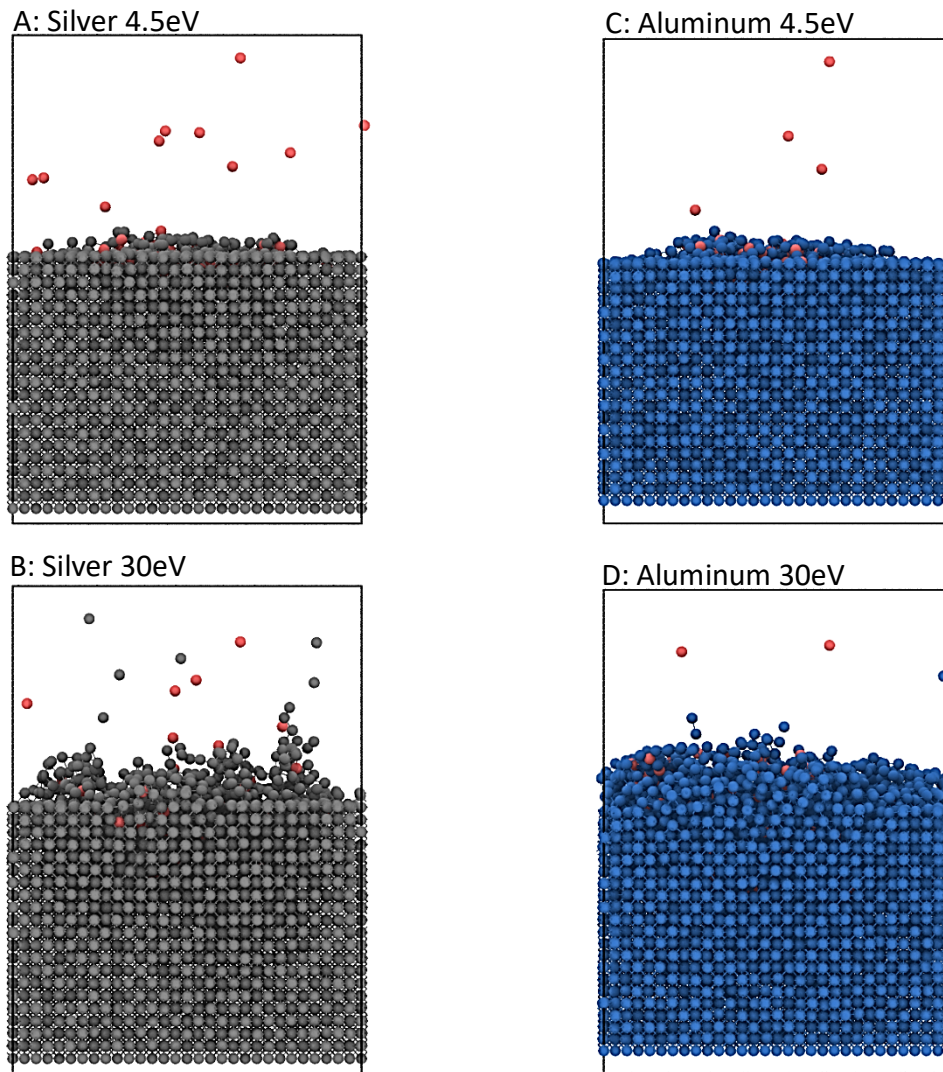


Figure 8.8 - Silver (A, B) and aluminum (C, D) substrates after 100 impacts at 4.5 eV and 30 eV, respectively. Red atoms are oxygen, grey are silver, and blue are aluminum

## Depth of Damage

Previous simulations on high energy impacts have focused on either erosion rates or defect formation. While the number of lost and defective atoms is important, it does not describe where this damage is focused and how much it permeates throughout the thickness. Therefore, in addition to tracking the number of defects, the depth of these defects into the substrate was also calculated using a custom Python-based modifier in the OVITO visualization software. The modifier selected vacancy and interstitial sites and tracked their depth as a function of simulation time. Referring to Fig 8.9, for both silver and aluminum the depth of damage increased with time and impact energy. It is important to note that there were fairly significant fluctuations as damage develops during impact. Many of the spikes in Fig 8.9 are caused by defects that are formed and then quickly recombine as damage and temperature increase. Similar to the number of defects, the maximum depth at the end of impact increased linearly with impact energy for both aluminum ( $R_2 = 0.98$ ) and silver ( $R_2 = 0.99$ ). Moreover, the maximum depth at the end of the simulation was on average 1.5 times higher for aluminum than for silver. For example, at 20 eV impact energy the maximum depth of damage for the silver substrate was 15.28 Å after 200 impacts. At the same impact energy damage in the aluminum substrate was found at a depth of 22.31 Å. Therefore, not only does aluminum have more damage than silver, the depth of this damage also extends deeper into the substrate.

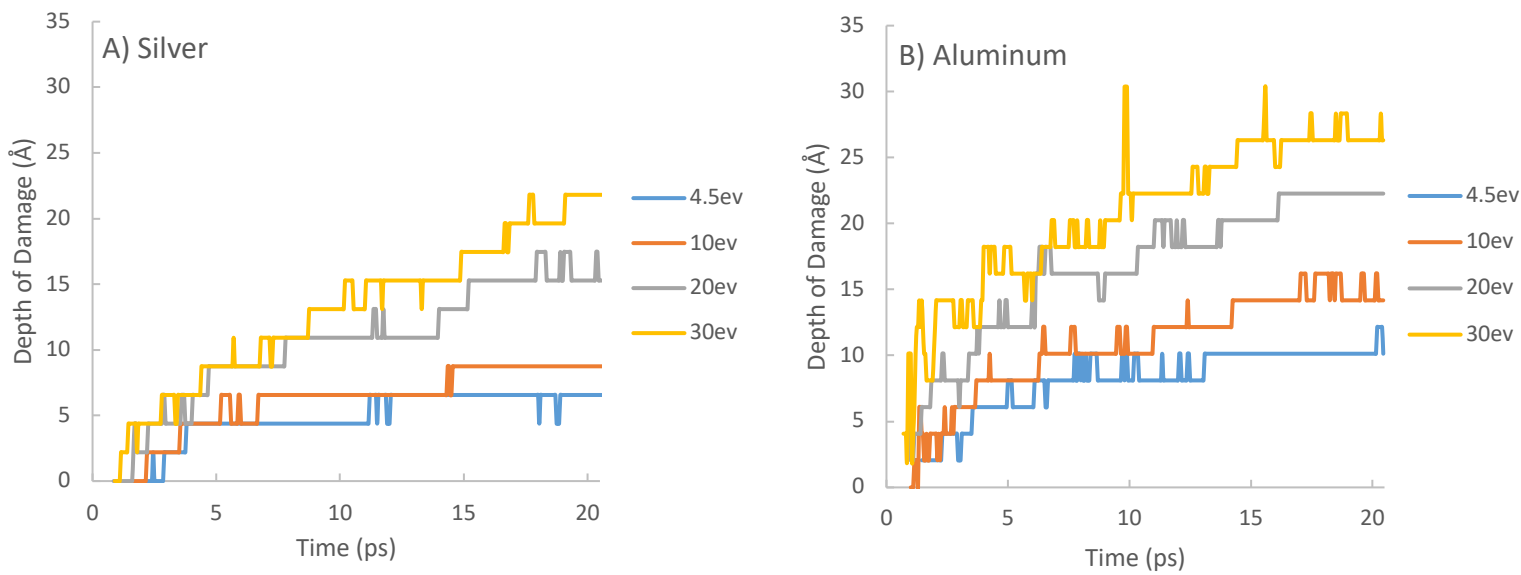


Figure 8.9 - Depth of defects in substrate for silver (A) and aluminum (B) as a function of impact energy using a thin bath layer

### Evolution of Defects after Impact

The final step in this study was to consider how defects in the system evolved after the impacts were concluded and the substrate was brought back down to its original temperature. Similar to studies on damage cascades [12]-[15] an annealing process was used to allow vacancy-interstitial pairs to recombine and ensure that remaining defects were stable. After 200 impacts two annealing cycles were performed using an *NVT* thermostat that involved heating the substrate to 500K and holding for 200 ps, and then cooling to 200K and holding for 100 ps. Defects were again tracked using a WS defect analysis. Referring to Table 8.4, for all substrates the total number of stable defects after the heating/cooling process was less than what was initially observed after impact. In all cases after annealing there was still more damage in the aluminum substrates, thus further supporting the conclusion that erosion yield is not enough to predict damage. However, the difference between damage in the substrates increased

with increasing impact energy. For example, after annealing there was only a small discrepancy in defects per atoms at 4.5 eV. However, at 30 eV there were over 50% more defects per atom for aluminum than for silver (Fig 8.10).

Table 8.4 - Number of defects per atom after impact and annealing for aluminum and silver after annealing for various impact energies using a thin bath layer

Impact Energy (eV)	Defects per Atom	
	Aluminum	Silver
4.5	0.013	0.011
10	0.032	0.021
20	0.081	0.065
30	0.17	0.11

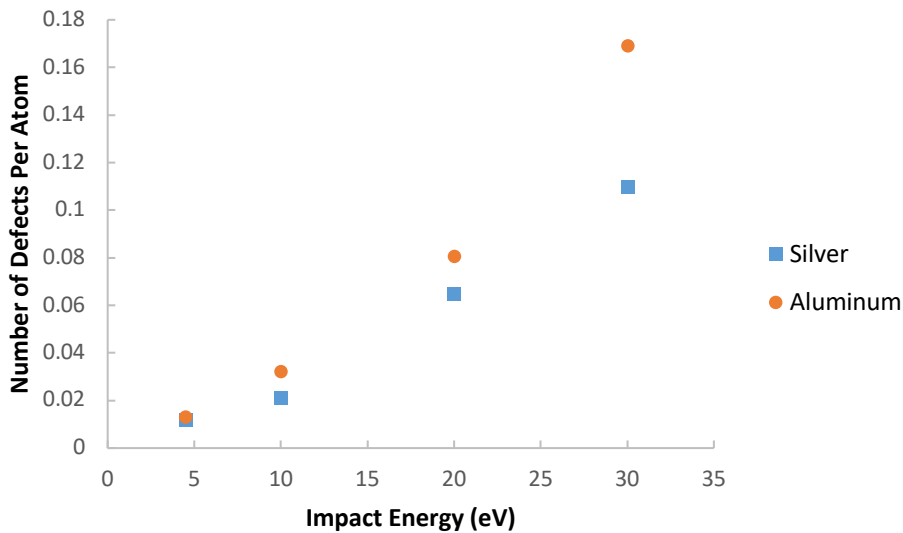


Figure 8.10 - Number of defects per atom after impact and annealing for silver and aluminum as a function of impact energy using a thin bath layer

## Conclusions

In conclusion, this study used the ReaxFF force field to determine the effect of impact energy on the damage of silver and aluminum due to atomic oxygen. While previous research has used these methods to simulate the LEO environment, research is needed on the performance of these materials when subjected to the higher energy collisions possible in deep space. Simply assuming a material is suitable based on its LEO performance is not sufficient. Moreover, as opposed to focusing on erosion rate, this study considered the effect these collisions have on the damage of the remaining substrate. Results from this study demonstrated that for both silver and aluminum the damage of the substrate (as determined by the number of defects) was correlated to the impact energy of the incoming AO. As expected based on LEO studies and cohesive energy, silver was shown to have more erosion than aluminum. However, despite the higher erosion, more damage was observed in the aluminum substrates due to its lower vacancy formation energy. Therefore, erosion yields do not necessarily indicate the state of the remaining substrate. As missions continue to move to deeper space and harsher environments the need for accurate simulation methods to accurately predict material performance will become paramount. This study demonstrates the potential for molecular dynamics simulations to be used to compare the material performance and degradation in these harsh deep space environments.

## References

- [1] Banks, B. A., Rutledge, S. K., Brady, J. A., and Merrow, J. E., 1989, "Atomic Oxygen Effects on Materials."
- [2] Zhang, J., and Minton, T. K., 2001, "Production of Volatile CO and CO<sub>2</sub> from Oxidized Polyethylene and Graphite Surfaces by Hyperthermal Atom-Surface Collisions," *High Perform. Polym.*, **13**(3), pp. S467–S482.
- [3] Srama, R., Ahrens, T. J., Altobelli, N., Auer, S., Bradley, J. G., Burton, M., Dikarev, V. V., Economou, T., Fechtig, H., Gv̇drlich, M., Grande, M., Graps, A., Gṙv̇n, E., Havnes, O., Helfert, S., Horanyi, M., Igenbergs, E., Jessberger, E. K., Johnson, T. V., Kempf, S., Krivov, A. V., Kṙv̇ger, H., Mocker-Ahlreep, A., Moragas-Klostermeyer, G., Lamy, P., Landgraf, M., Linkert, D., Linkert, G., Lura, F., McDonnell, J. A. M., Ṁdhlmann, D., Morfill, G. E., Ṁller, M., Roy, M., Scḣfer, G., Schlotzhauer, G., Schwehm, G. H., Spahn, F., Sṫbig, M., Svestka, J., Tschernjawski, V., Tuzzolino, A. J., Ẇsch, R., and Zook, H. A., 2004, "The Cassini Cosmic Dust Analyzer," *The Cassini-Huygens Mission: Orbiter In Situ Investigations Volume 2*, C.T. Russell, ed., Springer Netherlands, Dordrecht, pp. 465–518.
- [4] Parker, E. N., 1953, "The Interstellar Structures. I. Gas Clouds.," *Astrophys. J.*, **117**, p. 169.
- [5] Hoang, T., Lazarian, A., Burkhart, B., and Loeb, A., 2017, "The Interaction of Relativistic Spacecrafts with the Interstellar Medium," *Astrophys. J.*, **837**(1), p. 5.
- [6] Rahnamoun, A., and Van Duin, A. C. T., 2014, "Reactive Molecular Dynamics Simulation on the Disintegration of Kapton, POSS Polyimide, Amorphous Silica, and Teflon during Atomic Oxygen Impact Using the Reaxff Reactive Force-Field Method," *J. Phys. Chem. A*, **118**(15), pp. 2780–2787.
- [7] Zeng, F., Peng, C., Liu, Y., and Qu, J., 2015, "Reactive Molecular Dynamics Simulations on the Disintegration of PVDF, FP-POSS, and Their Composite during Atomic Oxygen Impact," *J. Phys. Chem. A*, **119**(30), pp. 8359–8368.
- [8] Morrissey, L. S., Handrigan, S. M., Nakhla, S., and Rahnamoun, A., 2019, "Erosion of Spacecraft Metals Due to Atomic Oxygen: A Molecular Dynamics Simulation," *J. Spacecr. Rockets*, **56**(4), pp. 1231–1236.
- [9] Van Duin, A. C. T., Dasgupta, S., Lorant, F., and Goddard, W. A., 2001, "ReaxFF: A Reactive Force Field for Hydrocarbons," *J. Phys. Chem. A*, **105**(41), pp. 9396–9409.
- [10] Lloyd, A., Cornil, D., Van Duin, A. C. T., van Duin, D., Smith, R., Kenny, S. D., Cornil, J., and Beljonne, D., 2016, "Development of a ReaxFF Potential for Ag/Zn/O and Application to Ag Deposition on ZnO," *Surf. Sci.*, **645**, pp. 67–73.
- [11] Hong, S., and van Duin, A. C. T., 2016, "Atomistic-Scale Analysis of Carbon Coating and Its Effect on the Oxidation of Aluminum Nanoparticles by ReaxFF-Molecular Dynamics Simulations," *J. Phys. Chem. C*, **120**(17), pp. 9464–9474.
- [12] Nordlund, K., Ghaly, M., Averback, R. S., Caturla, M., de La Rubia, T. D., and Tarus, J., 1998, "Defect Production in Collision Cascades in Elemental Semiconductors and Fcc Metals," *Phys. Rev. B*, **57**(13), p. 7556.
- [13] Zepeda-Ruiz, L. A., Han, S., Srolovitz, D. J., Car, R., and Wirth, B. D., 2003, "Molecular Dynamics Study of the Threshold Displacement Energy in Vanadium," *Phys. Rev. B*, **67**(13), p. 134114.

- [14] Ackland, G. J., Bacon, D. J., Calder, A. F., and Harry, T., 1997, "Computer Simulation of Point Defect Properties in Dilute Fe—Cu Alloy Using a Many-Body Interatomic Potential," *Philos. Mag. A*, **75**(3), pp. 713–732.
- [15] Chen, P. H., Avchachov, K., Nordlund, K., and Pussi, K., 2013, "Molecular Dynamics Simulation of Radiation Damage in CaCd<sub>6</sub> Quasicrystal Cubic Approximant up to 10 KeV," *J. Chem. Phys.*, **138**(23), p. 234505.
- [16] Yuan, B., Zeng, F., Peng, C., and Wang, Y., 2018, "A Reactive Molecular Dynamics Simulation Study to the Disintegration of PVDF and Its Composite under the Impact of a Single Silicon-Oxygen Cluster," *Comput. Mater. Sci.*, **154**, pp. 14–24.
- [17] Stukowski, A., 2009, "Visualization and Analysis of Atomistic Simulation Data with OVITO—the Open Visualization Tool," *Model. Simul. Mater. Sci. Eng.*, **18**(1), p. 15012.
- [18] Ogorodnikov, V. V., Rakitskii, A. N., and Rogovoi, Y. I., 1988, "Calculation of the Vacancy Formation Energy of Metals," *Sov. Powder Met. Met. Ceram.(Engl. Transl.);(United States)*, **27**(1).
- [19] Vijh, A. K., 1985, "The Fundamental Factor Determining the Sputtering Yields of Metals Bombarded with 20-KeV Oxygen Cations," *J. Mater. Sci. Lett.*, **4**(8), pp. 1036–1037.
- [20] De Rooy, A., 1985, "The Degradation of Metal Surfaces by Atomic Oxygen," *Proceedings of the 3rd European Symposium on Spacecraft Materials in a Space Environment*, pp. 99–108.
- [21] Jiang, D. E., and Carter, E. A., 2004, "First Principles Assessment of Ideal Fracture Energies of Materials with Mobile Impurities: Implications for Hydrogen Embrittlement of Metals," *Acta Mater.*, **52**(16), pp. 4801–4807.

## Summary

Overall, the purpose of this thesis was to use multiscale methods to develop a better understanding of the role various atomistic processes play in the degradation of mechanical properties in harsh environments. To achieve this purpose the study utilized various testing and simulation techniques. The study then focused on two specific environments where atomic scale processes can significantly effect macroscale mechanical properties: the effect of atomic hydrogen in harsh offshore oil and gas environments, and the effect of atomic oxygen impacts in space. The above chapters detail an exhaustive process of using testing and simulations to better understand how to account for microscale and atomistic defects on the predicted mechanical properties.

First, Chapter 2 attempted to better understand the effect hydrogen charging alone has on the void structure of steels. Previous research has suggested that an increase in voids pre loading will affect void growth and failure upon loading. Moreover, recently developed HE models have suggested that the interaction of hydrogen with voids may be critical to understanding the HE process. Therefore, this study using CT imaging to quantify the effect of hydrogen on initial void fraction. Six samples of 13-Cr Stainless steel were imaged before and after hydrogen charging and images were formed into a 3D model. Charging was shown to increase initial void fraction by 18 times pre loading. Therefore this study supported the theory that an important role of hydrogen promoting failure is to increase void production through the recombination into  $H_2$ .

Building on the findings of Chapter 2, Chapter 3 attempted to understand the role porosity plays on the elastic modulus of low porosity materials. This study developed a FEM to demonstrate that a macroscale plate with a center hole could be used to model the effect of porosity on the elastic modulus. The FEM agreed with previous low porosity models and, when compared to pre-existing experimental data, had better accuracy than all pre-existing models. Therefore this model can be used to estimate the effect of micropores on elastic modulus. However, while this model is capable of estimating the effect on macroscale elastic modulus, it cannot actually simulate the degradation process on the scale in which it is physically occurring. As such, the question remains as to why the elastic modulus is being reduced and how other defects may be influencing this reduction. As a result, there is a need for an atomistic model that can model the degradation process on the scale in which it occurs.

After demonstrating the effect of hydrogen on voids and of voids on macroscale properties, the next question was how best to model the unique multiscale HE process. Inspired by the limitations of the model in Chapter 3, MD was investigated due to its ability to both model atomistic processes and predict macroscale mechanical properties. However, there was a lack of clear understanding on which potential should be used when attempting to obtain these properties. Therefore, before attempting to simulate HE using MD, Chapter 4 evaluated various types of potentials for their accuracy in predicting the mechanical properties of pure iron from an atomistic uniaxial tension test at room temperature. Results demonstrated that EAM and MEAM potentials better predicted the elastic modulus of single crystal iron as compared to ReaxFF and Tersoff potentials. Findings were compared to previously conducted experimental data from uniaxial laboratory tension tests. The source of these errors was attributed to potential specific parameterization. While some potentials were developed specifically with elastic constants at realizable temperatures, others were not intended or tested for mechanical

properties. The findings highlighted the need to understand the capabilities and limitations of each potential before application to a problem outside of the initial intended use.

Building on the findings of Chapter 4, Chapter 5 was conducted to address the single crystal limitations of MD studies. Previous research on mechanical properties typically deal with perfect single crystals. While these single crystal structures are applicable to nanomaterials, they are not comparable to the polycrystalline structures that would be observed on the macroscale. Therefore, the purpose of Chapter 5 was to investigate whether single anisotropic crystals can be used to predict the elastic modulus of bulk polycrystalline samples. Findings demonstrated that the accuracy of a potential is dependent on the crystal direction. Therefore it is not sufficient to demonstrate potential accuracy by only testing one crystal orientation. Further, the most accurate potentials from a fixed volume condition were not necessarily the most accurate when simulating a physically realizable tension test (*NPT* dynamics). Finally, the Voigt Reuss Hill (VRH) method was shown to accurately predict polycrystalline mechanical properties from single crystal data as a function of temperature. Overall, Chapters 3 and 4 highlighted the importance of assessing a potential prior to use and demonstrated those potentials that were most accurate at predicting single crystal and polycrystalline elastic properties from uniaxial tension tests.

After developing a better understanding on how to accurately attain mechanical properties from atomistic simulations the next steps were to apply these findings to two harsh environments where atomistic processes have been known to degrade mechanical performance; hydrogen embrittlement in offshore oil and gas (Case Study 1) and atomic impacts in space (Case Study 2). For Case Study 1, Chapter 6 used MD to determine the effect lattice hydrogen concentration has on the mechanical

properties of iron at various temperatures. Previous experimental studies have suggested that hydrogen will degrade the elastic modulus and yield stress. However, due to the atomistic scale of the hydrogen these studies have difficulty quantifying and controlling the concentration of hydrogen in the lattice. Moreover, MD studies on HE typically focus more on the mechanisms of embrittlement and less on the subsequent degradation of mechanical properties. First, Chapter 6 demonstrated that the EAM type potential was best suited to modelling mechanical properties during HE as it better predicted the hydrogen free modulus and diffusion coefficient of hydrogen in iron. Results showed that increasing diffuse hydrogen in the lattice resulted in a linear decrease in the elastic modulus and stress at dislocation initiation. Moreover, as the concentration of hydrogen increased there was a higher density of dislocations after reaching peak stress. This lead to more dislocation interaction and shorter slip distances, corresponding to less steep declines in the stress strain curve after reaching the peak stress. Overall, hydrogen was shown to promote the nucleation and propagation of dislocations in the lattice, resulting in a lower elastic modulus and peak stress.

In addition to HE in the harsh offshore environment, consideration was also given to other environments where atomistic processes are damaging material performance. For example, in the LEO high energy atomic oxygen can impact materials and lead to erosion and damage. However, given the constant uncertainty in space budgets and high cost of launches it is difficult to test new materials in these environments. Moreover, these flight tests can only view the effect of the AO collision but are unable to achieve a scale where each individual impact can be observed. Therefore, Case Study 2 (Chapters 7 and 8) used MD to better understand the effect of AO in the LEO and deep space. First Chapter 7 used ReaxFF to model the effect of AO impacts on the erosion and temperature of spacecraft metals. Previous research has used MD to test polymers in space, but no work had been done previously on metals. During impact the erosion yield and substrate temperature were tracked and compared to

previously reported erosion yields from flight tests. Predicted erosion yields for silver and gold closely matched experimental values and it was shown that an energy barrier needed to be overcome before erosion could occur.

Finally, after demonstrating the accuracy of using MD to simulate material performance in space, Chapter 8 extended these findings to deep space where higher energy collisions can occur and flight experiments are extremely difficult to conduct. Moreover, as opposed to simply tracking erosion yields like previous tests and simulations, this study used a defect analysis method to track the damage of the remaining substrate as a function of impact. While silver was shown to have a higher erosion yield than aluminum, its substrate formed less defects at all impact energies considered. The source of this discrepancy was attributed to the lower energy needed to form vacancies in aluminum as compared to silver. This Chapter concluded that while erosion is certainly an important parameter in measuring the damage to a material by high energy impacts, it is not sufficient to describe the amount of damage and state of the remaining substrate. This study demonstrates the potential for MD simulations to be used to compare material performance and degradation in harsh deep space environments where testing may not be possible.

Future work for this thesis will be to continue to work towards realistic simulations that are accurate and comparable to macroscale experiments. Focus will be paid to continue to enhance the understanding of the two environments considered. First, after simulating the hydrogen base case, future work will begin to layer in other defects and see how they interact with hydrogen. For example, can the combined effect of hydrogen and voids be estimated through simple superposition? If not, what interactions are occurring during loading. For space work, there is a bounty of possible avenues. For

example, solar wind impacts on surfaces represent another important area where simulations are needed. Accurate simulations of these plasma-planetary impacts is critical to understanding planetary and exosphere evolutions. These simulations could be relevant to any celestial body impacted by solar wind. Further, MD simulations on impacts on space metals can consider the effects of pre-existing damage, along with larger scale impacts such as compounds.

Overall, this thesis has used multiscale testing and simulation methods to demonstrate and quantify the effect atomistic processes can have on macroscale mechanical properties. Findings have highlighted the importance of considering these atomistic processes on the scale in which they occur as opposed to simply observing their macroscale effects. Methods developed in this thesis were applied to develop a better understanding of the effect of atomic hydrogen in harsh offshore oil and gas environments, and of high energy atomic impacts in space. Specifically, MD simulations were highlighted as an invaluable tool to developing a better understanding of these processes and their effect on material performance.